Aqueous Aerosols in Atmospheric Chemistry and Airborne Diseases

Thesis by

Alan Yalun Gu

In Partial Fulfillment of the Requirements for
the Degree of
Doctor of Philosophy

CALIFORNIA INSTITUTE OF TECHNOLOGY
Pasadena, California

2022
(Defended April 7, 2022)

Alan Yalun Gu
ORCID: 0000-0001-8095-3634

ACKNOWLEDGEMENTS

Prof. Michael Hoffmann has always been supportive and available during the past several years when I explored vastly different fields of research. When we first met in January 2018, I was a fledgling eager to join a group for rotation, but not sure what I could do. Mike took me into his group with no questions asked. I appreciated that very much because at that time, I would not have been able to answer any questions about research had he asked. Prior to COVID-19, I focused on experimental atmospheric chemistry studies using a custom mass spectrometer developed in house. When the pandemic hit, the laboratory was closed for months, and around the same time the funding for the atmospheric chemistry projects was coming to an end. Thanks to Mike inviting me to the biochemistry subgroup in our research group, I was able to continue my residency. In 2021, I switched to yet another research topic of carbon capture, with an entrepreneurial plan that may take off at any time. Mike accommodated this variability with utmost flexibility, ensuring a smooth transition for me and for the burgeoning company. My experience at Caltech would not have been nearly as educational and enjoyable without him.

My thesis committee, Prof. Paul Wennberg, Prof. William Goddard III, and Prof. Harry Gray, took an extended period out of their busy schedule to offer advice on my work. My gratitude extends to them for this opportunity to learn from the experts in their respective fields.

A. J. Colussi, Lijie (Sara) Li and Nathan Dalleska were my first mentors after my arrival in the Hoffmann Group. A.J. taught me how to do research, which served as the cornerstone of my scientific career. Thanks to his pedagogy, I was able to switch research topics over the past several years and continue to invent new technologies in my future career. Sara showed me how to perform the atmospheric chemistry experiments and analyze the data and bore with my unfamiliar experimental techniques when I broke the mass spectrometer microjet and interrupted her research. Nathan taught me from the fundamental principles to the maintenance procedures of analytical instruments, which were instrumental to my

understanding of the chemistry involved in the experiments. I am so lucky to have the right mixture of advisor and mentors, and my scientific career will be a tribute to them.

This thesis work is made possible by the generous support of the National Science Foundation for the atmospheric Fenton chemistry project, Bill & Melinda Gates Foundation for the SARS-CoV-2 transmission modelling and testing device projects, and Resnick Sustainability Institute for the CO_2 projects. Thanks to them for having faith in me when I was new in the respective research fields and supported my exploratory work when success was by no means guaranteed.

Thanks to Clément Cid, Stephanie Yanchinski, and Neil Fromer for their support in the business planning and commercialization efforts in the carbon capture project. Entrepreneurship is full of unknown unknowns for me, and their support turns these unknowns into knowns.

The work presented in this thesis would not have been possible without my collaborators: Charles Musgrave, Prof. William Goddard III, Yi Zhang, and Lei Guo on the atmospheric chemistry projects; Yanzhe Zhu, Sean McBeath, and Xunyi Wu on the SARS-CoV-2 projects; as well as Heng Dong and Léopold Dobelle on the CO_2 projects.

Special thanks to Jing Li who was not only a collaborator but a mentor in biochemistry and microbiology, patiently teaching me the basics from my Grade 10 biology foundation and caring for my learning outcome.

Prof. Lifeng Yin visited our laboratory prior to the pandemic and showed me how versatile a researcher can be. We shared laughter, solution-driven research goals, and an entrepreneurial spirit. Our collaboration is going to make both of our lives so much more interesting. Despite the short time Prof. Xuejing Yang visited our laboratory, her knowledge and thinking paradigm inspired the project in Chapter V, and she continued to offer help in our later correspondence. It was so fortunate for me to have met them this early in my career.

Prof. Michael Vicic made my teaching assistant duties an experience beyond just graduation requirements. His care for his teaching assistants and his students' learning outcome is exemplary.

John Nagara from the patent office was consistently dependable during our collaboration, and I could always rely on him to be on time for meetings and deadlines. Such professionalism is the pinnacle of what I strive to attain.

Thanks to Prof. Paul Wennberg for inviting me to join his group meetings and activities. This small community meant a lot to me, especially at the start of my graduate studies when the only project I was working on was atmospheric chemistry and no one else in my own research group was working on anything remotely similar.

Thanks to Yuanlong Huang, Prof. John Seinfeld, Prof. Richard Flagan, Prof. Jess Adkins, and Donna Wrublewski for thought-provoking discussions. The knowledge they offered in their respective fields transformed my unknown unknowns into known unknowns.

The experimental efforts described in this thesis and beyond are reliant on the staff of the Linde Laboratory: Nora Oshima, Bronagh Glaser, and Leilani Rivera-Dotson. After the courses, the laboratory became my home. Thank you for making it a sweet one.

The Barracuda Virtual Reactor simulation software team, especially Peter Glaser and the support team, were very helpful and accommodating our request as their new academic customer as well as the questions encountered during the learning process. Thanks to them, I can end my graduate studies on a high note.

Graduate studies are more than projects, and I am fortunate to have met my lab mates and friends: Seungkyeum Kim, Axl LeVan, Prof. Kai Liu, Prof. Yang Yang, Cody Finke, Hugo Leandri, Eric Huang, Nissim Gore-Datar, Kevin Vu, Siwen Wang, and John-Alexander

Preuß. Thank you for sharing a nice time with me, including, or perhaps especially, when not talking about research.

Thanks to Sai Gu, for I owe it all to her.

ABSTRACT

Aqueous atmospheric aerosols are small droplets (typically smaller than 5 μm) suspended in the air that are comprised of water and water-soluble components. These aerosols provide an air-water interfacial reaction environment on their surfaces, and act as a medium for airborne disease transmission. In this thesis, Chapters II and V explore atmospherically relevant reactions on the aqueous aerosol surface using an online mass spectrometry, while Chapter III investigates the SARS-CoV-2 airborne transmission considering suspended virus-laden aerosols as the transmission media. Spinning off this SARS-CoV-2 work, Chapter IV describes a newly developed quantitative RNA amplification test kit for COVID-19, with an emphasis on the amplification result photo recognition component.

PUBLISHED CONTENT AND CONTRIBUTIONS

Gu, A. Y., Musgrave, C., Goddard, W. A., Hoffmann, M. R., & Colussi, A. J. (2021). Role of Ferryl Ion Intermediates in Fast Fenton Chemistry on Aqueous Microdroplets. *Environmental Science & Technology, 55*(21), 14370-14377. doi:10.1021/acs.est.1c01962

G. A. Y. designed the experiments, performed the experiments, analyzed the data, and wrote the non-computational sections of the manuscript.

Gu, A. Y.[#], Zhu, Y.[#], Li, J., & Hoffmann, M. R. (2022). Speech-Generated Aerosol Settling Times and Viral Viability Can Improve COVID-19 Transmission Prediction. *Environmental Science: Atmospheres*. doi:10.1039/d1ea00013f

G. A. Y. conceived the project, designed the computational algorithm, collaborated in writing the code, analyzed the data, and wrote the manuscript other than the figures.

Zhu, Y., Wu, X., Gu, A., Dobelle, L., Cid, C. A., Li, J., & Hoffmann, M. R. (2021). Membrane-Based In-Gel Loop-Mediated Isothermal Amplification (mgLAMP) System for SARS-CoV-2 Quantification in Environmental Waters. *Environmental Science & Technology*. doi:10.1021/acs.est.1c04623

G. A. collaborated in performing the experiments, analyzing the data, and writing the manuscript.

TABLE OF CONTENTS

LIST OF ILLUSTRATIONS

Number *Page*

LIST OF TABLES

Number *Page*

Chapter 1

INTRODUCTION

Chapter II was completed prior to COVID-19, investigating the ozone Fenton chemistry at the interface between an aqueous aerosol containing ferrous ion and gas phase ozone. This reaction produces reactive ferryl ions and hydroxyl radicals, both capable of driving oxidation chemistries in the atmosphere. This chapter investigates the oxidation kinetics of ozone Fenton chemistry via both the ferryl and the hydroxyl oxidation intermediates simultaneously using an online electrospray ionization mass spectrometry. In the spray chamber of the mass spectrometer, an aqueous jet containing ferrous perchlorate and dimethyl sulfoxide reacts with an intersecting gas stream of ozone, where the reaction takes place at the air-water interface. Results suggest that the ferryl ions are the dominant intermediate over hydroxyl radicals by 2 orders of magnitude at acidic pH. The interfacial kinetics is measured to be 4 orders of magnitude faster than the bulk aqueous phase kinetics for this ozone Fenton reaction system. The ferryl ion intermediate also dominate over the hydroxyl radicals in the bulk aqueous phase. In the presence of a common atmospheric ligand, the oxidation of an atmospheric substrate by the ozone Fenton reaction via the ferryl intermediate may be accelerated or suppressed, and the kinetics may be predicted by the standard reduction potential of ligated ferryl ions.

Chapter III was completed during the lockdown period of the COVID-19 pandemic and is a simulation investigation of the role of indirect airborne transmission of SARS-CoV-2. In the beginning of the pandemic, there was significant uncertainty towards the primary route of transmission, with contaminated surfaces and airborne aerosol transmission being the contenders. In contaminated-surface-based transmission, virus is deposited onto a surface by an infected individual, and is transmitted to another individual when that individual touches the contaminated surface. In airborne transmission, virus-laden aerosols are emitted by an infected individual, and another individual breathes in those suspended aerosols. Because the

settling time of those aerosols and the viability of the SARS-CoV-2 virus in those aerosols are direct functions of the ambient temperature and humidity, one expects to see correlation between weather and SARS-CoV-2 transmission when linked via the aerosol settling time and viral variability. Assuming a typical speech-generated aerosol size of 6 μm as the initial aerosol size and an asymptomatic transmission period of 5 days prior to testing, statistically significant correlation is observed in the reported data of 5 United States counties using linear regression and recurrent neural network. This result supports asymptomatic airborne transmission as a primary transmission route of SARS-CoV-2, and encourages epidemiologists to include meteorological variables in future disease transmission models.

Chapter IV was completed after the initial lockdown period of the pandemic, where I developed an image recognition software to count RNA amplicons after a Membrane-Based In-Gel Loop-Mediated Isothermal Amplification (mgLAMP) reaction. The mgLAMP is an alternative to Reverse Transcription quantitative Polymerase Chain Reaction (RT-qPCR) in SARS-CoV-2 detection, but with fewer equipment requirements due to its isothermal nature. Taking advantage of this lower requirement, our group has developed a home test kit for SARS-CoV-2 capable from collecting an individual's virus sample to obtaining a photo of the mgLAMP reaction glass slide. The Google AutoML Vision module presented in this chapter counts the amplicons in the photo, and returns a total count number. A non-zero count is a positive test result, and a zero count is a negative result. The computer count agrees with manual count with a slope of 0.9926 (R^2 = 0.992) and may be used to reduce worker workload at testing centers or produce an automatic result for home test kit users.

Chapter V is an ongoing experimental project investigating the importance of peroxymonocarbonate chemistry in the atmosphere. Peroxymonocarbonate is an oxidative intermediate formed from CO_2 and H_2O_2, and has been found to oxidize sulfides and alkenes ~100 times faster than H_2O_2 alone. The importance of this reaction in the atmosphere, however, remains unexplored. This work quantifies the rate acceleration by introducing gaseous or dissolved CO_2 into H_2O_2 oxidation reactions relevant in the atmosphere. The experiment is carried out in the online electrospray ionization mass spectrometer outlined in

Chapter II. Preliminary results suggest 2 orders of magnitude rate acceleration by introducing CO_2, and another 4 orders of magnitude rate acceleration at the air-water interface vs bulk aqueous phase. CO_2-activated H_2O_2 chemistry may play an important yet previously unrecognized role in atmospheric chemistry and may explain the observed higher-than-expected oxidation rates of various substrates in the atmosphere.

Chapter 2

AIR-WATER INTERFACIAL OZONE FENTON CHEMISTRY

Gu, A. Y., Musgrave, C., Goddard, W. A., Hoffmann, M. R., & Colussi, A. J. (2021). Role of Ferryl Ion Intermediates in Fast Fenton Chemistry on Aqueous Microdroplets. *Environmental Science & Technology, 55*(21), 14370-14377. doi:10.1021/acs.est.1c01962

1.1 Abstract

In the aqueous environment, Fe^{II} ions enhance the oxidative potential of ozone and hydrogen peroxide by generating the reactive oxoiron species (ferryl ion, $Fe^{IV}O^{2+}$) and hydroxyl radical ($^{\cdot}OH$) via Fenton chemistry. Herein, we investigate factors that control the pathways of these reactive intermediates in the oxidation of dimethyl sulfoxide (Me_2SO) in Fe^{II} solutions reacting with O_3 in both bulk-phase water and on the surfaces of aqueous microdroplets. Electrospray ionization mass spectrometry is used to quantify the formation of dimethyl sulfone (Me_2SO_2, from $Fe^{IV}O^{2+}$ + Me_2SO) and methanesulfonate ($MeSO_3^-$, from $^{\cdot}OH$ + Me_2SO) over a wide range of Fe^{II} and O_3 concentrations and pH. In addition, the role of environmentally relevant organic ligands on the reaction kinetics was also explored. The experimental results show that Fenton chemistry proceeds at a rate ~10^4 times faster on microdroplets than in bulk-phase water. Since the production of $MeSO_3^-$ is initiated by $^{\cdot}OH$ radicals at diffusion-controlled rates, experimental ratios of $Me_2SO_2/MeSO_3^- > 10^2$ suggest that $Fe^{IV}O^{2+}$ is the dominant intermediate under all conditions. Me_2SO_2 yields in the presence of ligands, L, vary as volcano-plot functions of

$E^0(LFe^{IV}O^{2+} + O_2/LFe^{2+} + O_3)$ reduction potentials calculated by DFT with a maximum achieved in the case of L ≡ oxalate. Our findings underscore the key role of ferryl $Fe^{IV}O^{2+}$ intermediates in Fenton chemistry taking take place on aqueous microdroplets.

1.2 Synopsis Statement

The ferryl ion intermediate in the reaction between dissolved iron and gaseous ozone can play a more important role than previously envisioned in the atmospheric system.

1.3 Introduction

Atmospheric oxidants such as ozone (O_3) and hydrogen peroxide (H_2O_2) react with the transition metal ions in natural aqueous media. In aerosol microdroplets, Fe^{II}/Fe^{III} and Cu^{I}/Cu^{II},[1] catalyze the oxidation of the aerosol organic components by O_3 and H_2O_2 via Fenton chemistry.[2] This chemistry is ubiquitous in the atmosphere.[3-13] The catalytic mechanism involves the production of more reactive intermediates, which in the case of Fe^{II} can be either high-valent state oxoiron (ferryl) $Fe^{IV}O^{2+}$ ions[14] or hydroxyl radicals ·OH, reactions R1 and R2.[15]

$$Fe^{II} + O_3 + H^+ \longrightarrow Fe^{III} + {\cdot}OH + O_2 \qquad [R1]$$

$$Fe^{II} + O_3 \longrightarrow Fe^{IV}O^{2+} + O_2 \qquad [R2]$$

Both, ·OH radicals, $E^0({\cdot}OH + H^+ + e^- \rightleftharpoons H_2O) = 2.7$ V vs SHE, and $Fe^{IV}O^{2+}$, $E^0(FeO^{2+} + H^+ + e^- \rightleftharpoons Fe(OH)^{2+}) > 1.2$V vs SHE, are strong one-electron oxidants, but their chemistries are quite different.[16] $Fe^{IV}O^{2+}$ can transfer O-atoms to low-valence atoms,[17] such as divalent S, or selectively insert O-atoms into C-H bonds via Gif chemistry.[18-20] Hydroxyl radicals (·OH), in contrast, are unselective and react with most substrates via fast H-atom abstractions or addition reactions.[21] Both intermediates generate products that are generally different from those obtained in the uncatalyzed oxidations.[22] These are significant issues in atmospheric chemistry. For example, one study estimated that up to ~30% of atmospheric ·OH would be accounted for by Fenton chemistry if reaction R1 were the exclusive channel.[23] A $Fe^{IV}O^{2+}/{\cdot}OH = 10^4$ ratio would account for the oxidation of atmospheric SO_2 in thick hazes.[23]

In the atmosphere, $Fe^{IV}O^{2+}$ can oxidize dimethyl sulfoxide,[24] epoxidize alkenes[25] such as isoprene and pinene,[26] and hydroxylate short alkanes.[27] It may also oxidize alcohols[28] and organosulfides into aldehydes and sulfoxides.

However, factors that control the relative importance of R1 vs R2 reactions are not well understood. Factors that could affect the outcome of Fenton reactions include the nature of the substrates, pH,[16] solvents,[29] and the presence and nature of complexing ligands.[30]

In this paper, we address the issues as they relate to the Fenton oxidation of dimethyl sulfoxide (Me_2SO) 1) at the air-water interface of microdroplets by exposing aqueous (Me_2SO + Fe^{II}) solutions to O_3(g), and 2) in bulk water by mixing solutions of (Me_2SO + Fe^{II}) with O_3(aq). The main reaction products are dimethyl sulfone (Me_2SO_2) and methanesulfonate ($MeSO_3^-$) as shown in R3-R5.[31]

$$Me_2SO + Fe^{IV}O^{2+} \longrightarrow Me_2SO_2 + Fe^{2+} \qquad [R3]$$

$$Me_2SO + {}^{\cdot}OH \longrightarrow {}^{\cdot}CH_3 + MeSO_2^- + H^+ \qquad [R4]$$

$$MeSO_2^- + {}^{\cdot}OH + O_2 \longrightarrow MeSO_3^- + HO_2{}^{\cdot} \qquad [R5]$$

Our choice of Me_2SO as the substrate is based, in part, on the fact that it is a common component of the marine aerosol resulting from the processing of biogenic dimethyl sulfide (Me_2S) emissions.[32] These emissions account for ~15% of the global atmospheric sulfur budget. Moreover, in part, by the fact that Me_2SO not only reacts with ·OH radicals, but with $Fe^{IV}O^{2+}$ ions via O-atom transfer to the S-atom.[16] This feature lets us simultaneously track the competition between reactions R3 vs R4-R5 under identical conditions.

The ozone Fenton reaction, Fe^{II} + O_3, was studied because it is expected to be more important than the Fe^{II} + H_2O_2 reaction under atmospheric conditions. For example, the O_3 and H_2O_2 tropospheric concentrations are comparable (typically 10 ppbv O_3 vs 2 ppbv H_2O_2), but their Henry's law constants are very different: $H(H_2O_2) = 9 \times 10^2$ mol m^{-3} Pa^{-1} vs $H(O_3) = 1.0 \times 10^{-4}$ mol m^{-3} Pa^{-1}. Consequently, the concentrations of dissolved H_2O_2 are expected to be ~

10^7 larger than those of O_3. Although O_3 reacts only ~ 10^4 times faster than H_2O_2: $k_{(FeII + O3)}$ = 8.2×10^5 M^{-1} s^{-1} vs $k_{(FeII + H2O2)}$ = 76 M^{-1} s^{-1} in bulk water,[33-34] our experiments show that O_3(g) reacts with Fe^{II}(aq) ions at the air-water interface of aqueous microdroplets faster than H_2O_2,[35] and ~10^4 times faster than in bulk water. Therefore, O_3 is expected to compete favorably with H_2O_2 at the air-water interface. Fenton chemistry as driven by O_3(g) and H_2O_2(g) on aqueous microdroplets is similar.[35] Based on these considerations and previous observations, we make the case that Fenton chemistry on aqueous aerosols mostly proceeds via reactions R1 and R2.

1.4 Methods

1.4.1 Experimental Section

Positively and negatively charged reaction products were analyzed by electrospray ionization mass spectrometry (ESI-MS). In the gas-liquid experiments, aqueous solutions of Me_2SO and $Fe(ClO_4)_2$ (in some experiments also containing one of the following ligands: sodium oxalate, sodium malonate, sodium tartrate, disodium-dihydrogen ethylenediaminetetraacetate, dimethylamine, trimethylamine, p-benzoquinone, 1,4-naphthaquinone or catechol) are injected (at 30 µL min^{-1} through a stainless steel Agilent G1946-68703 nozzle) into the spray chamber of the ESI mass spectrometer (Agilent G2445A Ion Trap MSD) (maintained at 1 atm with ultrapure N_2(g), 293 ± 2 K) using a syringe pump (Cole-Parmer 74905-02 and 74905-50) . A coaxial, codirectional, fast (~340m s^{-1}) stream of N_2(g) pneumatically nebulizes the outermost layers of the aqueous microjets into sub-micrometer-sized droplets (microdroplets) within 50 µs.[36] Microjets and microdroplets were made to react with an orthogonal stream of O_3(g) directed to the tip of the nozzle for ~ 1 ms, which is the estimated residence time of the microdroplets in the spray chamber, before they are pumped into the low pressure section of the mass spectrometer.[37-38] Microdroplets are naturally charged during nebulization by the segregation of anions from cations and deflected by an applied electric field towards the inlet to the low-pressure section of the mass spectrometer. Therein, microdroplets evaporate within a heated capillary tubing prior to undergoing Coulombic explosions that release the ions contained in the microdroplets to the

gas-phase for detection. A schematic of this experimental setup is shown in Figure 6. More details are provided in the Supporting Information (SI) section.

Experiments carried out in bulk-phase water were performed by injecting (Me_2SO + $Fe(ClO_4)_2$) and O_3 aqueous solutions through separate ports into a manifold mixer (Cole-Parmer Manifold Mixing Valve EW-01356-21, Figure 7) modelled as a tank reactor. The reactions were then allowed to take place for 12 minutes before injection into the ESI mass spectrometer for analysis. Instrumental drift was eliminated by adding non-complexing Cs^+ (50µM $CsClO_4$) and ClO_4^- (200µM $NaClO_4$) ions as internal standards. $Me_2SO_2H^+$ (from the protonation of the Me_2SO_2 product) and $MeSO_3^-$ product signals (see below) were quantified based on calibration curves obtained from Me_2SO_2 and $MeSO_3Na$ solutions (see Figures 8-10). Positive and negative ions were quantified in the same experiments by alternating positive/negative either in mass scanning or SIM (selected ion monitoring) detecting modes.

The ESI mass spectrometer was operated as follows. Positive ions were detected by polarizing the capillary at -3.4 kV (voltages relative to ground), the end plate offset and the capillary exit at 500 V and 78 V, respectively. In the negative mode, the capillary voltage was at 3.5 kV, and the end plate offset and the capillary exit at 500 and -64.5 V, respectively. The nebulizer N_2 gas source was maintained at 40 psi, and the drying gas (at 340 °C) flow rate was 12 L min^{-1}.

Ozone was generated by flowing ultrapure grade 99.9999 % O_2(g) at 50 cm^3 min^{-1} (via a mass flow controller (MKS 247) through an ozone generator (Ozone Solutions) and quantified via UV-visible absorption spectrophotometry (Shimazu UV-2101PC). The pH of aqueous solutions was adjusted before injection by adding $HClO_4$/NaOH solutions and measured (within ± 0.5 pH units) with pH paper (Milipore MCholorpHast). Sodium oxalate, sodium malonate, sodium tartrate, disodium-dihydrogen ethylenediaminetetraacetate (Na_2EDTA), dimethylamine (DMA), trimethylamine (TMA), p-benzoquinone, 1,4-naphthaquinone, catechol, dimethylsulfoxide (Me_2SO, DMSO), dimethylsulfone (Me_2SO_2, $DMSO_2$), sodium methanesulfinate ($MeSO_2Na$), sodium methanesulfonate ($MeSO_3Na$), iron (II) perchlorate ($Fe(ClO_4)_2$), cesium perchlorate ($CsClO_4$), sodium perchlorate ($NaClO_4$),

sodium sulfate (Na_2SO_4), acetonitrile (ACN), perchloric acid ($HClO_4$) and sodium hydroxide (NaOH) of purity 95% or higher were obtained from Sigma Aldrich and used as received.

1.4.2 Quantum Mechanical Calculations

Quantum mechanics (QM) calculations were carried out using Density Functional Theory (DFT) with the B3LYP hybrid functional selected for its high accuracy and versatility.[39] We used the Grimme-Becke-Johnson D3 empirical correction for describing London dispersion (van der Waals attraction) interactions.[40] Initial geometry optimizations were performed in the vacuum where all atoms were described with a singly-contracted triple-zeta basis set (TZV). Following vacuum optimizations, solvated single-point energies were calculated with an extended triplet-zeta basis set containing additional polarization functions on non-hydrogen atoms (TZV*).[41-42] To describe solvent effects, we used the Poisson Boltzmann Finite element (PBF) implicit solvent method with water solvent parameters of $\varepsilon = 80.37$ and a probe radius of 1.4 Å. The structure optimizations started with all structures having octahedral coordination of Fe^{II}/Fe^{IV}. To obtain accurate solvation energies for our clusters, we balanced the net charge to zero by replacing H_2O ligands with OH^- ions. For example, we performed calculations on the charge-neutral $[Fe^{IV}O(H_2O)_3(OH)_2]$, resulting from substituting two OH^- ions for two waters, rather than on $[Fe^{IV}O(H_2O)_5]^{2+}$ ions. We confirmed that charge neutralization barely affects the trend of reduction potential as a function of the ligand. After performing vacuum-optimizations at the B3LYP-D3/TZV level, all $Fe^{IV}O^{2+}$ structures converged to 6-coordinate iron-centered structures, except for the cases of $[Fe^{IV}O(H_2O)_2(OH)_2(TMA)]$, $[Fe^{IV}O(H_2O)_2(OH)_2(DMA)]$ (and un-ligated $[Fe^{IV}O(H_2O)_3(OH)_2]$, where TMA=trimethylamine and DMA=dimethylamine). These amines were treated as fully protonated ligands, whereas all other ligands were either singly or doubly deprotonated depending on experimental pH and pK_a values. The reaction free energies for the conversion of $Fe^{IV}O^{2+}$ to Fe^{II} (calculated as:$\Delta G_{rxn} = \left[G_{Fe^{II}} + G_{Me_2SO_2}\right] - \left[G_{Fe^{IV}O^{2+}} + G_{Me_2SO}\right]$) are interpreted as $Fe^{IV}O^{2+}$ 2-electron reduction potentials in which the reference oxidation is the conversion of Me_2SO to Me_2SO_2. In all cases, unfilled coordination sites on the 6-coordinate Fe centers were filled with additional waters. Table 2, Figure 11-12

and Appendix A show the optimized structures of ligated Fe^{II} and $Fe^{IV}O^{2+}$ complexes. The structures presented in our work represent the lowest-energy conformations for each structure. All Fe(IV) structures were modeled as high-spin quintets (singly occupied dxy,dxz,dyz,dx2-x2) and all Fe(II) were modeled as high-spin quintets (doubly occupied dxy). Since DFT is a single-determinant method, the high-spin configurations are the most reliable states.

1.5 Results and Discussion

1.5.1 Identification and Quantification of Products

Figure 1 shows the positive and negative mode ESI mass spectra obtained from (Me_2SO + $Fe(ClO4)_2$ + $CsClO_4$) aqueous microdroplets at pH 4.5 before and after exposure to O_3(g). In the absence of O_3, signals appear at m/z^+ = 133, 79, m/z^- = 99, 101, which correspond to Cs^+, Me_2SOH^+ and $^{35,37}ClO_4^-$, respectively. Upon O_3 exposure, new signals appear at m/z^+ = 95 ($Me_2SO_2H^+$), m/z^- = 95 ($MeSO_3^-$) and m/z^- = 97 (HSO_4^-). The relative ratios of $MeSO_3^-$ and HSO_4^- signal intensities: $I_{-95}/I_{-97} > 1$ (see Figure 13), are consistent with our previous study at pH 7.[43] We verified that the Me_2SO_2 and $MeSO_3^-$ products are inert in these experiments. Me_2SO_2 was also produced in the uncatalyzed ozonolysis of Me_2SO in the absence of $Fe(ClO_4)_2$, as reported in the literature.[44]

Signal intensities were converted to concentrations using Me_2SO_2, $MeSO_3Na$ and HSO_4Na calibration curves using $CsClO_4$ and $NaClO_4$ as the internal standards (Figure 8-10). We note that this procedure is approximate because the mass signals detected in our gas-liquid experiments correspond to species formed at the air-water interface, whereas calibration curves are based on mass signals from $Me_2SO_2H^+$, $MeSO_3^-$ and HSO_4^- ions present in bulk aqueous solutions. This procedure is correct to the extent that $Me_2SO_2H^+$, $MeSO_3^-$, HSO_4^-, and internal reference Cs^+ and ClO_4^- ions have similar surface affinities.[45] The dependences of $Me_2SO_2H^+/Cs^+$, $MeSO_3^-/ClO_4^-$ and HSO_4^-/ClO_4^- ratios as functions of experimental parameters are, of course, independent of such an assumption. The key result is that the main product of the Fenton oxidation of Me_2SO on microdroplets is Me_2SO_2, which is produced in mM concentrations vs $MeSO_3^-$ in μM concentrations. Figure 18a-c show $Me_2SO_2H^+$,

$MeSO_3^-$ and HSO_4^- signal intensities as functions of initial Fe^{II} and O_3 concentrations. Plotted $Me_2SO_2H^+$ signal intensities, I_{95+} (Figure 14a), correspond to I_{95+} signals obtained in the presence of Fe^{II} minus those measured in the uncatalyzed oxidation of Me_2SO by O_3 (see Figure 15 for raw, uncorrected $Me_2SO_2H^+$ signals).

1.5.2 Rates and Product Yields at the Air-Water Interface vs Bulk Water

The formation of Me_2SO_2 (detected as $Me_2SO_2H^+$) is consistent with one-step O-atom transfers from O_3 or $Fe^{IV}O^{2+}$ to Me_2SO (reaction **R3**) (Figure 2). The formation of $MeSO_3^-$ and HSO_4 from Me_2SO, on the other hand, is a multi-step process involving the splitting of one and two Me groups via C-S bond fissions, reactions **R4** and **R5.**[43] Leaving methyl groups are formed by breaking the weak C-S bonds of the sulfur-centered free radicals produced from ·OH radical additions to reduced S atoms.[43] ·OH radical addition reactions to S-atoms are very fast, with diffusion-controlled rate constants $k_4 \sim k_5 \sim k_{DMSO+OH} = 4.5 \times 10^9$ M^{-1} s^{-1} in bulk water.[46] Therefore, if all of $Fe^{IV}O^{2+}$, and most of the ·OH radicals produced in R1 react with Me_2SO (see below), from: $Me_2SO_2/(MeSO_3^- + HSO_4^-) < Me_2SO_2/MeSO_3^- = I_{95+}/I_{95-} = (k_3/k_4)[Fe^{IV}O^{2+}]/[\cdot OH]$, and the $k_3/k_4 \leq 1$ condition, the observed $I_{95+}/I_{95-} >> 1$ ratios imply that $[Fe^{IV}O^{2+}] >> [\cdot OH]$, that is: $k_2 >> k_1$.

That both $k_4 \sim k_5$ are diffusion-controlled is consistent with the rapid consumption via **R5** of the undetected methyl sulfinate $MeSO_2^-$ intermediate produced in **R4.** In other words, the rate of formation of $MeSO_3^-$ is in fact controlled by **R4**. The $Me_2SO_2H^+/MeSO_3^-$ ratios, evaluated from I_{95+}/I_{95-} values measured in gas-liquid experiments, as functions of $[Fe^{2+}]$ at various O_3(g) concentrations are shown in Figure 14. We found that ~1.5 mM Me_2SO_2 is produced from pH 4.5 (1 mM Me_2SO + 100 μM $Fe(ClO_4)_2$) solutions exposed to 113 ppm O_3 (equivalent to ≤ 0.4 mM O_3(aq) under equilibrium) for < 1 ms. The direct and inverse dependences of Me_2SO_2 and $MeSO_3^-$ concentrations on $[Fe^{2+}]$, Figure 14a-b, suggest that a small fraction of the ·OH radicals produced in R1 reacts further with Fe^{2+} in competition with Me_2SO, reaction R4. Note that the minor role assigned to ·OH radicals in these experiments is valid because the extrapolated $MeSO_3^-$ concentrations at $[Fe^{2+}] = 0$ still are in the μM scale (vs mM Me_2SO_2 concentrations). Me_2SO_2 and $MeSO_3^-$ are produced in mM and μM

concentrations in experiments exposing pH 4.5 $Fe(ClO_4)_2$ in aqueous microdroplets to O_3(g) for < 1 ms. The results imply that $Fe^{IV}O^{2+}$ ions are produced in 300-1600 larger yields than ·OH radicals on the surface of aerosol microdroplets at typical cloud water pH and iron concentrations.

To investigate the course of Fenton chemistry in bulk water, we rapidly mixed (Fe^{2+}+ Me_2SO) solutions with O_3(aq) solutions obtained by previously dissolving O_3(g) in water. In contrast to the gas-liquid experiments, we found that only ≤ 0.1 mM Me_2SO_2 was produced by mixing pH 4.5 (10 mM Me_2SO + 100 μM $Fe(ClO_4)_2$) with 10.6 mM O_3(aq) solutions for 12 minutes (See Figure 16-1.17). This result is consistent with previously reported kinetic values in bulk water (Kinetic Analysis in the SI).[44] Thus, under our experimental conditions, interfacial Fenton chemistry as catalyzed by $Fe(H_2O)_6^{2+}$ ions on microdroplets largely proceeds via the ferryl in, $Fe^{IV}O^{2+}$, pathway at a rate that is 10^4 times faster than in bulk water.

Figure 3 shows the structures of fully hydrated Fe^{2+} and FeO^{2+} ions with various ligands. It is apparent that the apical water of hexaquo Fe^{2+} ion needs to be replaced before (or during) an O-atom can be transferred from O_3 to produce the FeO^{2+} ion via an outer-sphere process. This process would be facilitated if the hydration shell of Fe^{2+} at the air-water interface presented a vacancy, preferentially oriented to the air phase that could accept an O-atom without paying an enthalpy penalty of dehydration.[35]

1.5.3 Ligand Effects

We tested the effects of environmentally relevant ligands (L) on the rates and products of interfacial ozone Fenton chemistry. Experiments involved (1 mM Me_2SO + 100 μM $Fe(ClO_4)_2$ + 200 μM L) microdroplets at pH 4.5, except as indicated, exposed to O_3(g) for < 1 ms. The mass spectrum recorded in a similar experiment is shown in Figure 18. Ligands were found to be inert under our experimental conditions. For example, we could not detect any new species from the oxidation of EDTA itself in these experiments. None of the ligands used in our experiments were expected to react with $Fe^{IV}O^{2+}$.[17, 47] Furthermore, none of the ligands at 200 μM is expected to significantly compete with 1 mM Me_2SO for ·OH radicals

either, because rate constants for ·OH radical reactions with most of the ligands used in our experiments are at least 10 times slower than $k_{DMSO+OH} = 4.5 \times 10^9$ M^{-1} s^{-1}.[46]

We found that the nature of the ligands has a significant effect on the dimethyl sulfone Me_2SO_2 concentrations (Figure 4), and a weaker effect on methanesulfonate $MeSO_3^-$ yields (Figure 19). Figure 4 shows the dependence of Me_2SO_2 yields as a function of the calculated reduction potentials of the complexed iron couples: $E^0(LFe^{IV}O^{2+} + O_2 = LFe^{2+} + O_3)$. The volcano-type dependence of Me_2SO_2 yields as a function of E^0 suggests the competition of opposite effects. A positive effect is most likely associated with faster rates of formation of the $LFe^{IV}O^{2+}$ intermediates with stronger Fe=O bonds expected at larger E^0 values. Negative effects arise from the slower O-atom transfers expected from stronger Fe=O bonds to Me_2SO. Me_2SO_2 yields are, therefore, expected to peak at an intermediate E^0 value, which in our experiments corresponds to the ligand L = oxalate (Figure 4). This explanation is consistent with previous studies for which the reactivity of ferryl ion intermediates was linked to the electron affinity of the iron-bound oxygen derived from DFT calculations.[48]

The data of Figure 4 were obtained at pH 4.5, the pH of 100 μM Fe^{II} solutions in equilibrium with atmospheric CO_2. Lower pH values are likely under atmospheric conditions.[49] Figure 5 shows the effect of [EDTA] on Me_2SO_2 yields at pH 1, 2 and 4.5. The successive pK_a's for H_4EDTA are 2.0, 2.7, 6.2 and 10.3. At pH 4.5, H_2EDTA^{2-} complexation has the net effect of increasing the reduction potential of Fe(IV) to Fe(II) as shown in Figure 4. This results in a decrease in the yield of the ferryl ion pathway as shown in Figure 5. Note that at pH 2.0, H_3EDTA^- complexation leads to an increase in the yield of the ferryl ion pathway. We ascribe this result to the effect of differently protonated ligands on Fe(IV) and Fe(II) reduction potentials.

Under atmospheric conditions, aerosols typically are comprised of mixtures of water with organics. Figure 20 shows that EDTA has minor effects in catechol/water and acetonitrile/water mixtures at pH 4.5. The lack of significant effects in mixed media suggests that EDTA is preferentially solvated by the organic solvents while Fe^{II} and ferryl ion remain in the aqueous microphase.[50]

The Fenton reaction between interfacial Fe^{II} ions and gas-phase ozone at the air-water interface of aqueous microdroplets mainly produces $Fe^{IV}O^{2+}$ via reaction R2 at a rate ~10^4 faster than the similar reaction in bulk water. The presence of complexing ligands affects both the relative and absolute rates of the ferryl ion and hydroxyl radical pathways. Dimethyl sulfoxide, Me_2SO, is an important intermediate in the tropospheric oxidation of biogenic S-containing gases. We have shown that the yields of dimethyl sulfone Me_2SO_2, the product of $LFe^{IV}O^{2+} + Me_2SO \longrightarrow$ reactions, were found to depend on the nature of L according to a volcano plot function of the E^0 ($LFe^{IV}O^{2+} + O_2 \rightleftharpoons LFe^{2+} + O_3$) reduction potentials as calculated by DFT with a peak at L ≡ oxalate. The volcano dependence of Me_2SO_2 yields reflects competing effects on the formation of Me_2SO_2 resulting from the influence of L on the strength of the Fe^{IV}=O bond. The stronger Fe^{IV}=O bonds produced at faster rates in reaction R2 become weaker O-atom donors to Me_2SO. Results show that ozone Fenton chemistry on aqueous microdroplets proceeds ~10^4 faster than in bulk-phase water due to the production of reactive ferryl ion ($Fe^{IV}O^{2+}$) intermediates that, in turn, depend on the specific nature of the available complexing ligands.

1.6 Summary

The Fenton reaction between interfacial Fe^{II} ions and gas-phase ozone at the air-water interface of aqueous microdroplets mainly produces ferryl $Fe^{IV}O^{2+}$ ions, reaction **R2**, ~ 10^4 faster than the similar reaction in bulk water. Ligands L affect both the relative and absolute rates of the ferryl and hydroxyl pathways. In the oxidation of dimethyl sulfoxide Me_2SO, an important intermediate in the tropospheric oxidation of biogenic S-containing gases, the yields of dimethyl sulfone Me_2SO_2, the product of $LFe^{IV}O^{2+} + Me_2SO$ reactions, were found to markedly depend on the nature of L according to a volcano function of the E^0($LFe^{IV}O^{2+} + O_2 = LFe^{2+} + O_3$) reduction potentials calculated by DFT, and peak at L ≡ oxalate. The volcano dependence of Me_2SO_2 yields reflects competing effects on the formation of Me_2SO_2 resulting from the influence of L on the strength of the Fe^{IV}=O bond. The stronger Fe^{IV}=O bonds produced at faster rates in reaction **R2** become weaker O-atom donors to Me_2SO. Present results show that ozone Fenton chemistry proceeds on aqueous microdroplets about 10^4 faster than in bulk water, mainly produces reactive ferryl $Fe^{IV}O^{2+}$ ion intermediates, and

strongly depends on typical organic ligands. These are relevant issues in the heterogeneous chemistries of atmospheric aerosol and cloud microdroplets.

1.7 Supporting Information

1.7.1 Online Electrospray Ionization Mass Spectrometry

In our gas-liquid experiments, the products generated in the microdroplets and the outermost layers of the microjets are analyzed without manipulation by online electrospray ionization mass spectrometry (ESI-MS).[37, 51] The production of charged microdroplets requires the conversion of the kinetic energy of the fast sheathing nebulizer N_2 stream into electrostatic energy associated with the separation of anions from cations and that associated with the creation of additional surface.[36] Charge separation is a direct result of the nebulizer gas because ion signals (1) increase at higher nebulizer gas velocity and (2) extrapolate to zero as nebulizer gas velocity drops to zero.[36, 51]. The polarizing external electric field required to deflect the charged microdroplets does not affect the observed interfacial chemistry, as shown, e.g., in the interfacial α-tocopherol ozonation reaction in the positive and negative modes.[52] This is consistent with the fact that the calculated electric field at the microjet tip is 2 orders of magnitude weaker than the electric field naturally present at the air-water interface.[53-54] The surface specificity of online ESI-MS has been demonstrated in several reports from our laboratory.[37, 55]

1.7.2 Quantification of Ozone Concentration in Spray Chamber

Quantification of interfacial ozone concentration assumes a well-mixed spray chamber with an $O_3/O_{2(g)}$ inlet at 50 cm^3/min and a jet of nebulizer gas stream through an annulus with an inner diameter of 100um and an outer diameter of 200um at sonic velocity. Ozone generator settings at 1200, 2700 and 3000 ppm in the $O_2/O_{3(g)}$ stream correspond to 113, 254 and 283 ppm in the spray chamber, respectively.

1.7.3 Kinetic Analysis of $Me_2SO_{(aq)}$ Ozonation in Bulk Water

In this experiment, $Me_2SO_{(aq)}$ and appropriate internal standards are dissolved in an aqueous solution in syringe A, while saturated $O_{3(aq)}$ aqueous solution in equilibrium with 3000ppm $O_{3(g)}$ is prepared in syringe B. Syringe A and B are each pushed at 15 μL/min into a manifold

tank reactor of volume 373 μL. The outlet of the manifold tank reactor connects to the ESI-MS microjet via PEEK capillary tubing of negligible internal volume.

Levanov et al.[56] reported the Henry's Law constant for ozone H_{O3} as a function of temperature

$$lnH_{O_3} = -(9.445) + \frac{2406}{T}$$

$$H_{O_3} = 86.8\ at\ 25\ ℃$$

Calculate the saturation concentration of O_3(aq) in equilibrium with 3000ppm $O_{3(g)}$

$$\left[O_{3_{aq}}\right] = 0.0106\ M$$

In the tank reactor, the concentration of O_3(aq) is diluted by half, resulting in an initial reaction concentration of

$$\frac{\left[O_{3_{aq}}\right]}{2} = 0.00532M = 255\ mg/L$$

At this ozone concentration, the ozonation Me_2SO follows zero-order kinetics with a rate constant k = 0.10 mM/min.[44]

We can calculate this rate constant from our bulk-phase experimental measurements. From Figure 8, we obtain the Me_2SO_2 concentration from direct ozonation to be 2.335 mM. We calculate the reaction time using a continuously stirred tank reactor model with a total volume of 373 μL and a total flow rate of 30 μL/min, and the residence time is

$$t = \frac{373}{30} = 12.43\ min$$

Hence the zero-order rate constant is

$$k_0 = \frac{2.335}{12.43} = 0.0188\ mM/min$$

Comparing with the literature reported value of 0.10 mM/min,[44] this confirms the slow bulk phase kinetics compared to interfacial kinetics where 2 mM Me_2SO_2 are formed from Me_2SO ozonolysis within 1 ms (Figure 16 y-intercept).

1.8 Figures

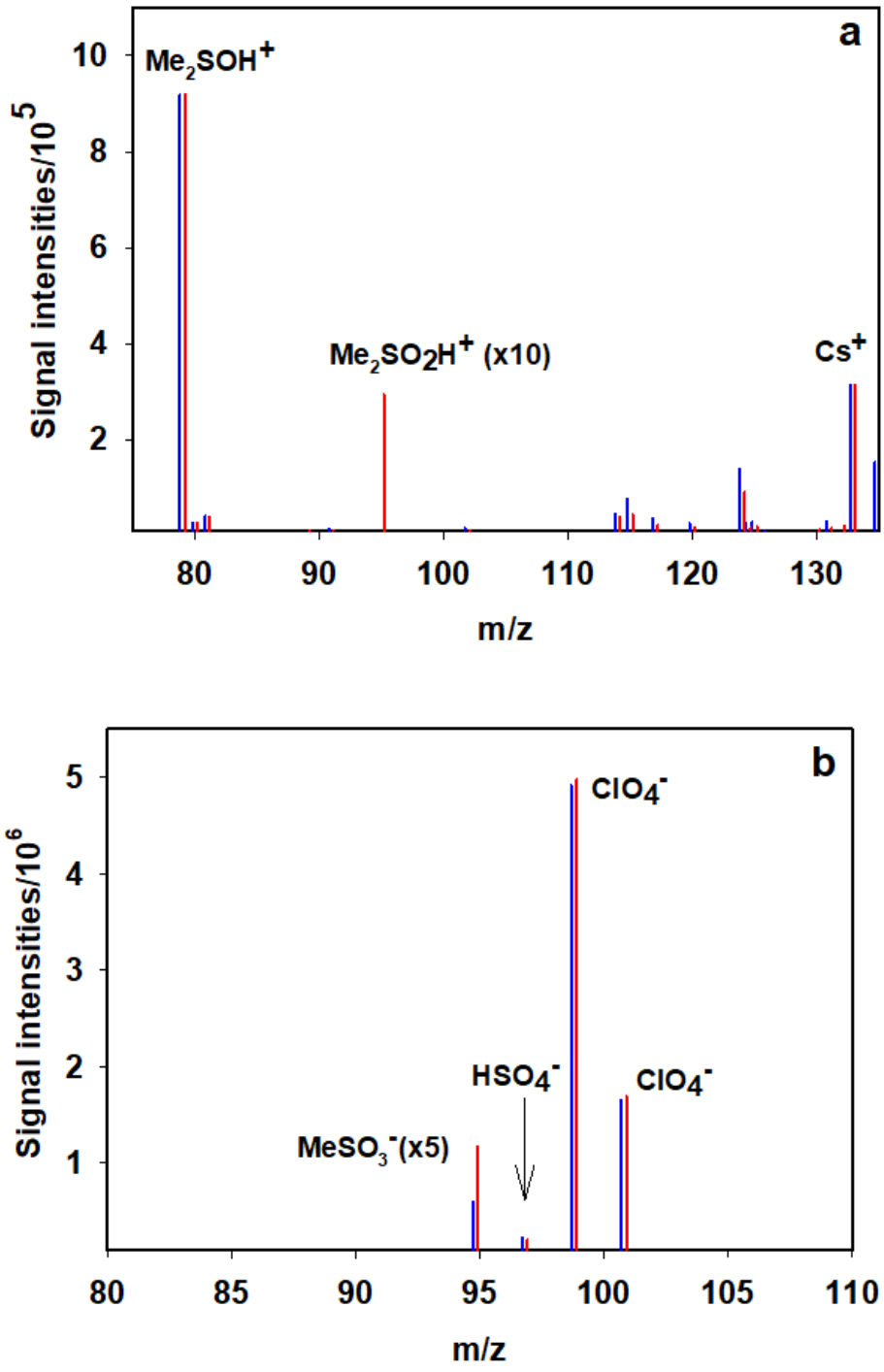

Figure 1. Positive (a) and negative (b) online electrospray ionization mass spectra of pH 4.5 (1mM Me_2SO + 100µM $Fe(ClO_4)_2$ + 50µM Cs^+ + 250µM ClO_4^-) aqueous

microdroplets before (blue) and after (red) exposure to 283ppm O_3(g) for < 1 ms. Cs^+ and ClO_4^- non-complexing ions added as internal standards.

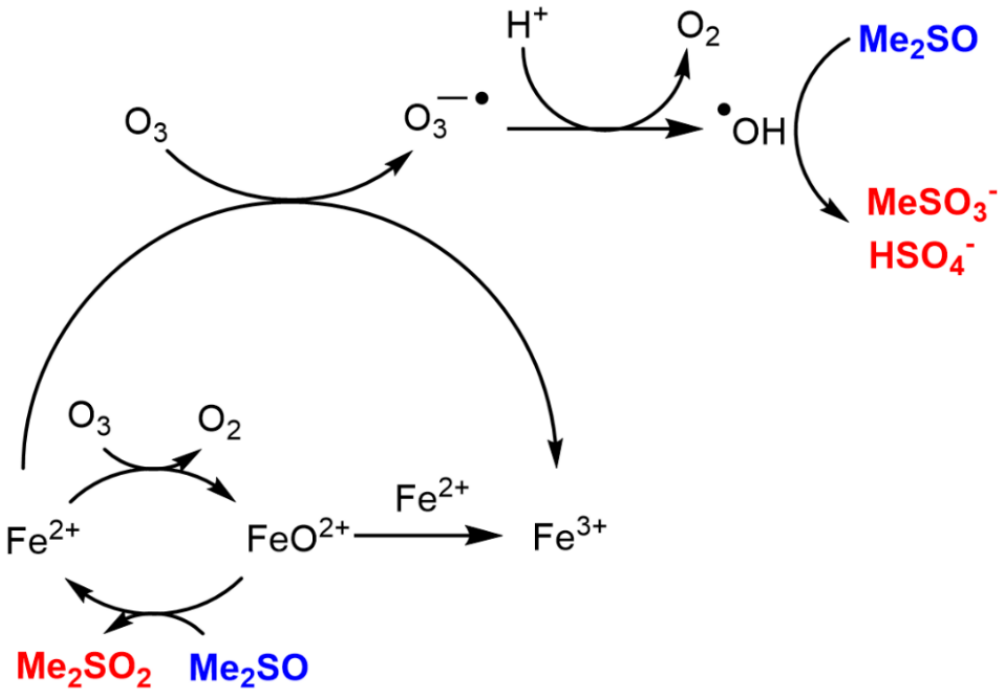

Figure 2. Mechanism of the Fenton oxidation of Me_2SO into Me_2SO_2, $MeSO_3^-$ and HSO_4^-. Me_2SO_2 is the only product of the ferryl ion pathway (bottom left).

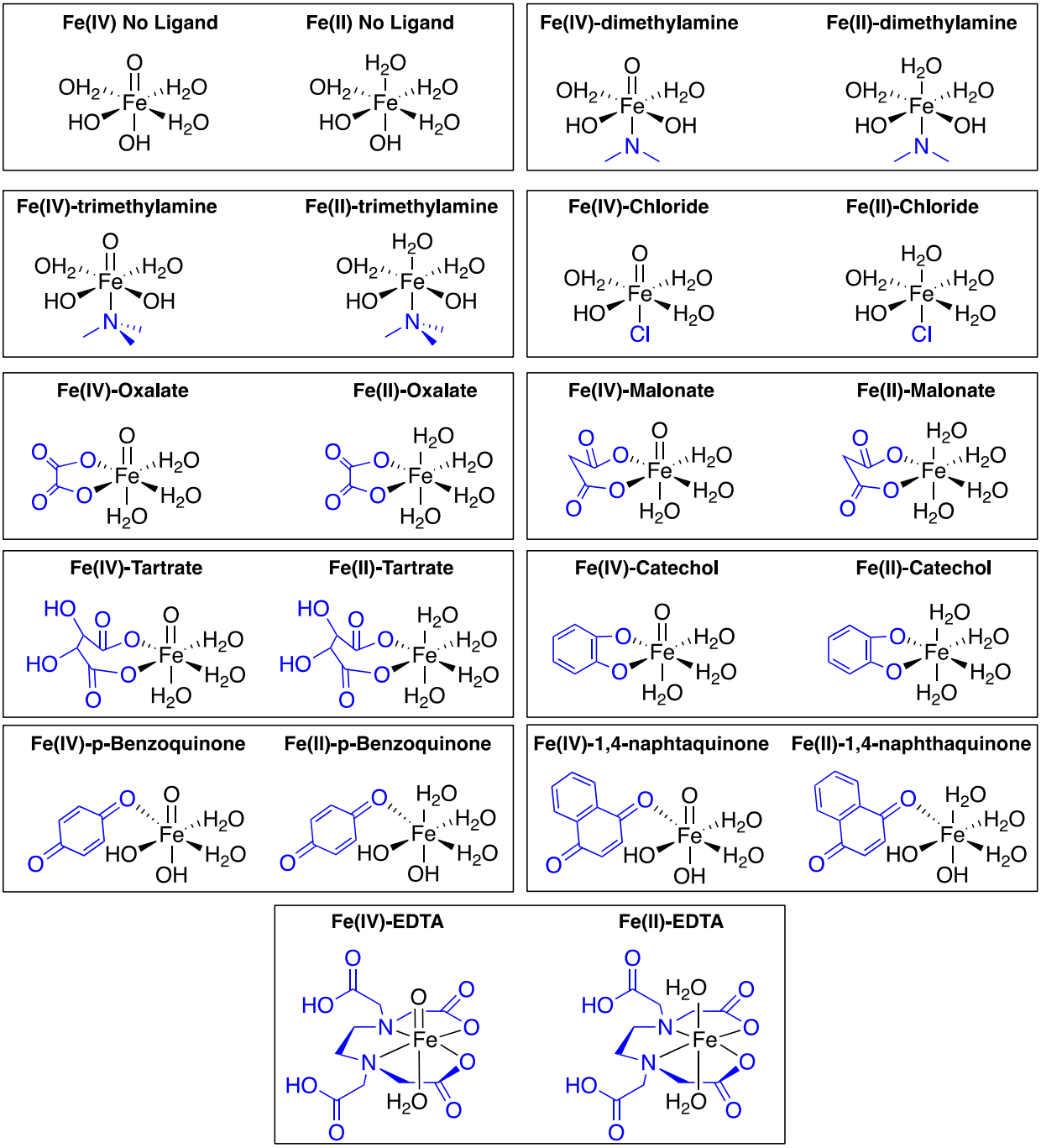

Figure 3. Structures of charge-neutral $Fe^{IV}O$ and Fe^{II} species. Ligands in blue. Structures do not report actual coordination, stereochemistry, denticity, or hapticity. For DFT-optimized structures, see Figures 11-12.

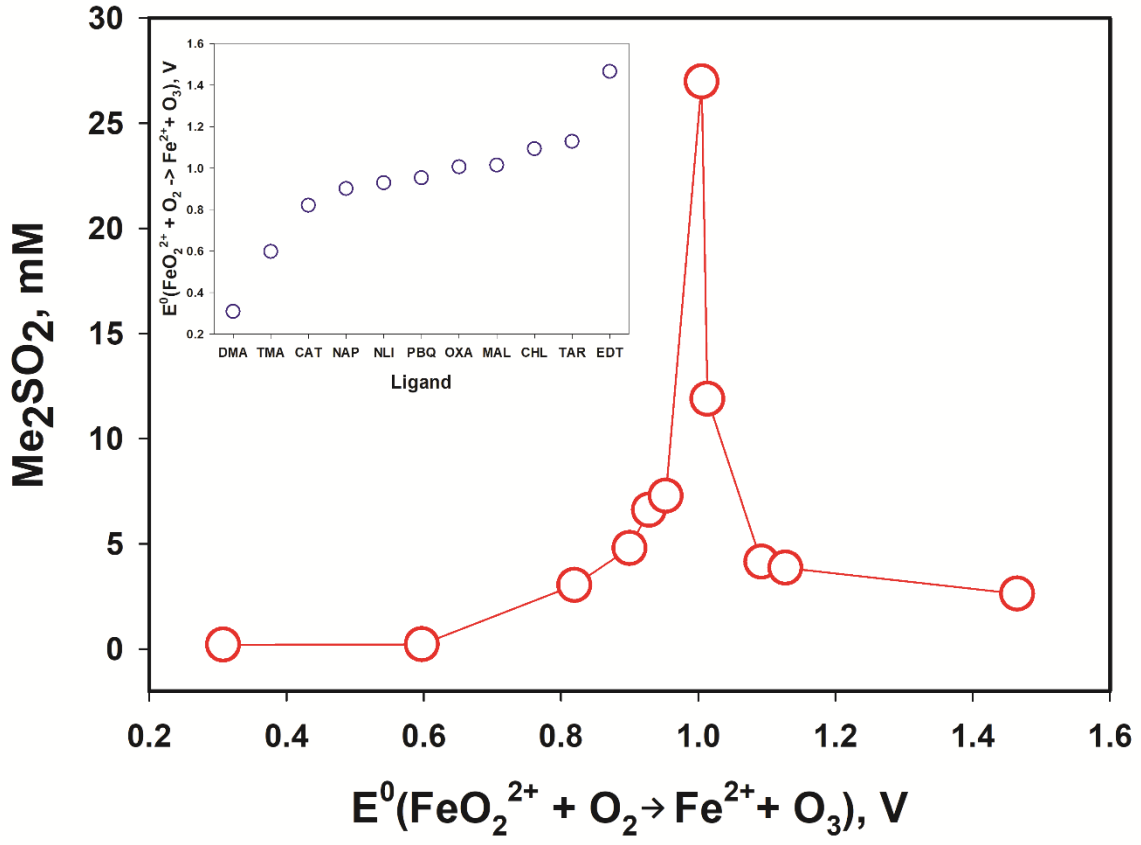

Figure 4. Ligand effects on the formation of dimethyl sulfone Me_2SO_2. [Me_2SO_2] vs $E^0(LFe^{IV}O^{2+} + O_2 \rightarrow LFe^{2+} + O_3)$ DFT formal reduction potentials calculated from $\Delta G(LFe^{IV}O^{2+} \rightarrow LFe^{2+})$ Gibbs free energies differences relative to $\Delta G(Me_2SO \rightarrow Me_2SO_2)$. The inset shows $E^0(LFe^{IV}O^{2+} + O_2 \rightarrow LFe^{2+} + O_3)$ values for the different ligands L. [Me_2SO_2] determined at the air-water interface of pH 4.5 [1mM Me_2SO + 100 µM $Fe(ClO_4)_2$ + 200 µM ligand L + 150 µM $NaClO_4$] aqueous microdroplets exposed to 283 ppmv O_3(g) for < 1 ms (see text for more details). Because no Cs^+ is used as the internal standard in the positive mode, the absolute concentration of [$Me_2SO_2H^+$] measured has higher uncertainty than Figure 14, though the trend is unaffected. Me_2SO_2 concentration is measured as $Me_2SO_2H^+$. Due to unavoidable complex formation between the negatively charged ligands and $Me_2SO_2H^+$ cation, the yield measured is an underestimate of the actual yield. DMA = dimethylamine, TMA = trimethylamine, CAT = catechol, NAP = naphthoquinone, NLI = no ligand, PBQ = p-benzoquinone, MAL = malonate, CHL = chloride, OXA = oxalate, TAR = tartrate, EDT = ethylenediaminetetraacetate.

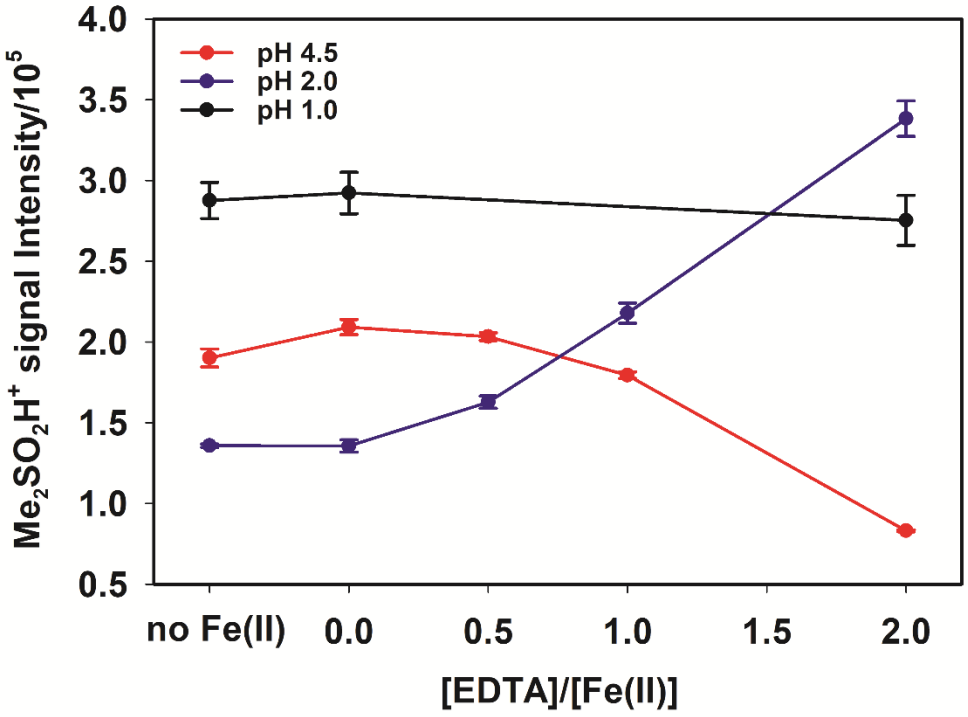

Figure 5. Protonated dimethyl sulfone $Me_2SO_2H^+$ ($m/z^+ = 95$) mass signal intensities vs [EDTA]/[Fe(II)] at various pH values. $Me_2SO_2H^+$ mass signal intensities are measured by online electrospray ionization mass spectrometry at the air-water interface of [1mM Me_2SO + 100 µM $Fe(ClO_4)_2$] aqueous microdroplets exposed to 283 ppm O_3(g) for < 1 ms. The mass signal intensities measure the net yield of Me_2SO_2 from Fenton chemistry and direct ozonolysis of Me_2SO, after subtracting the $Me_2SO_2H^+$ complexed by EDTA. No Fe(II) means experiments in the absence of EDTA or Fe^{II}.

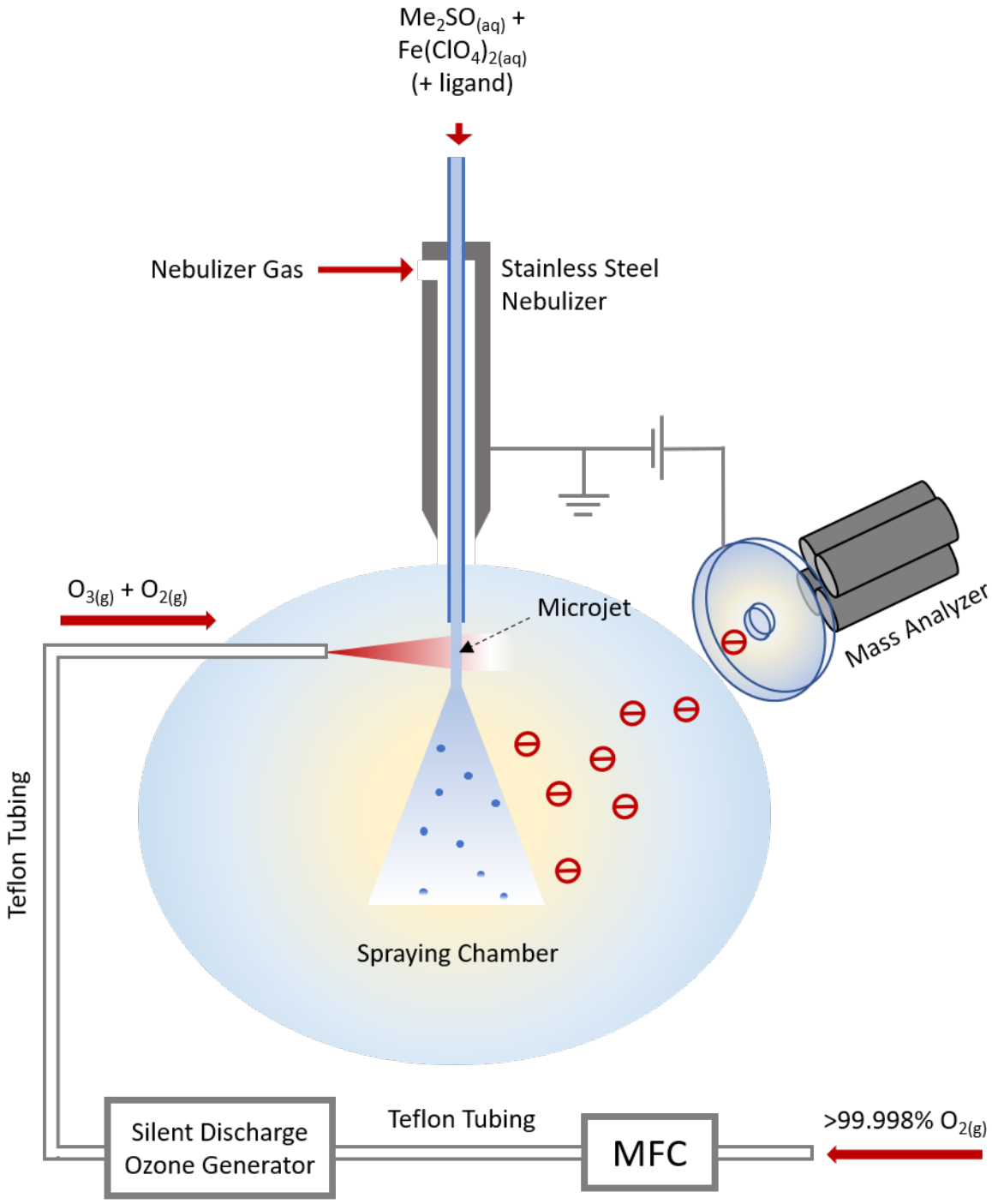

Figure 6. Experimental setup of online ES-MS. The aqueous reactants and gaseous reactants contact at the outlet tip of the microjet.

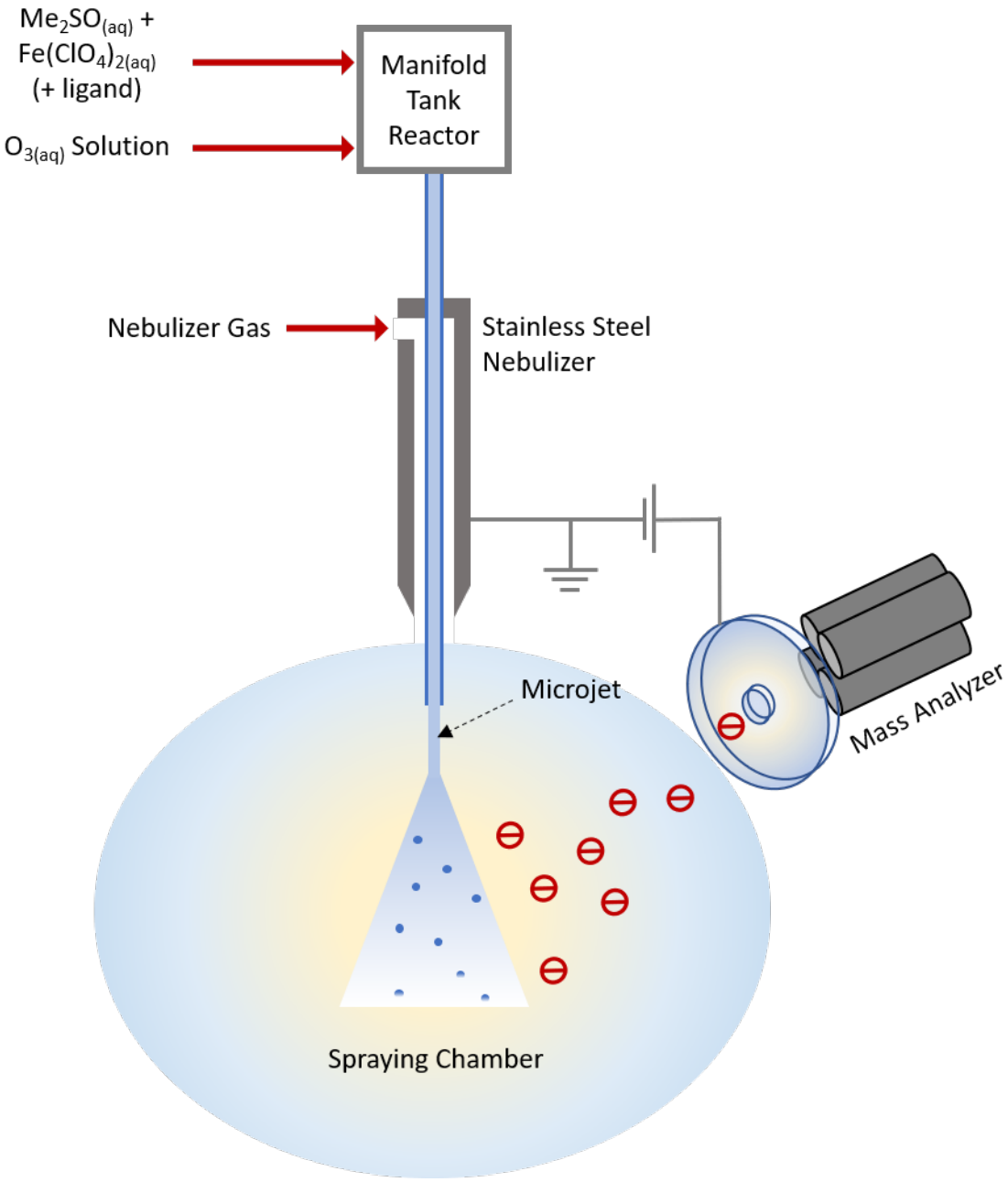

Figure 7. Experimental setup of offline ES-MS. The aqueous reactants contact each other in the manifold tank reactor before entering the microjet.

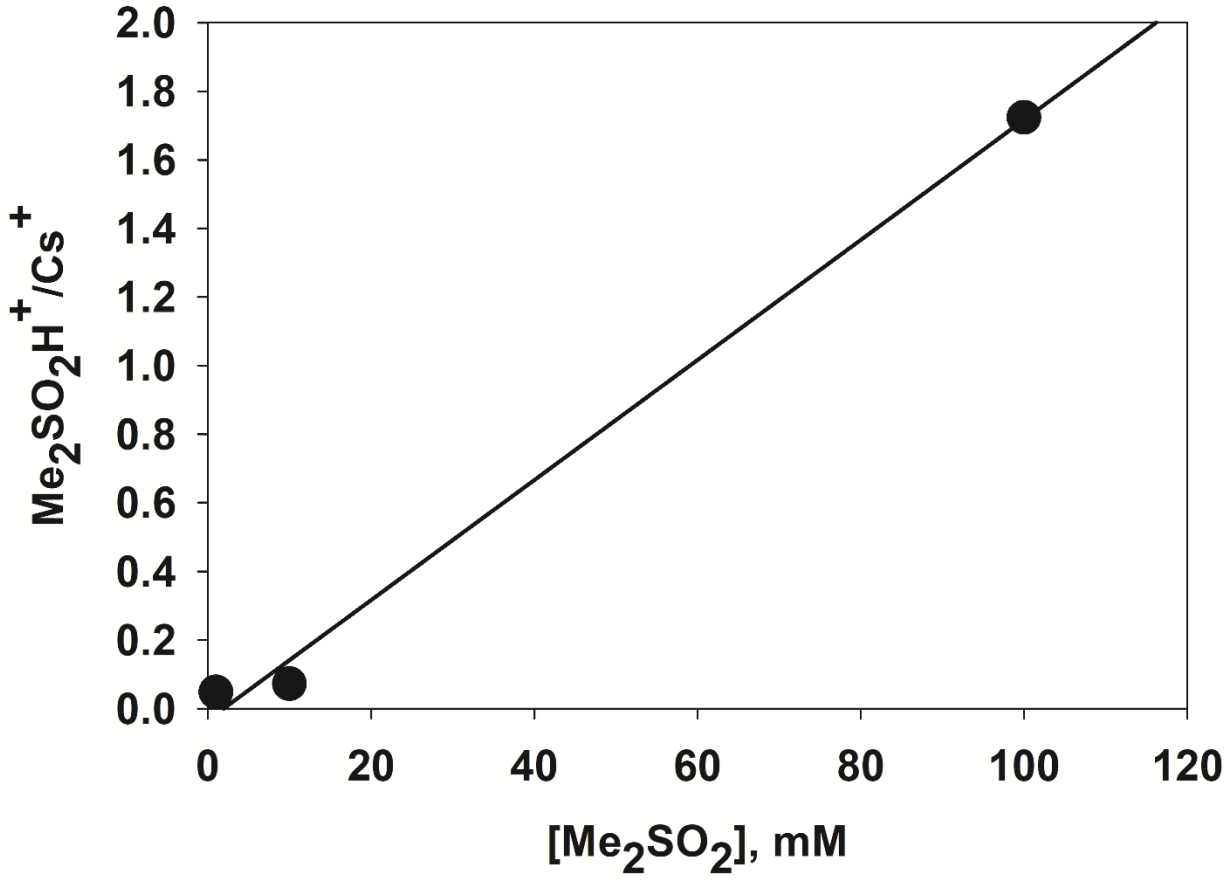

Figure 8. Me_2SO_2 calibration curve using 1, 10 and 100 mM Me_2SO_2. Y-axis plots the mass signal intensity ratios of $Me_2SO_2H^+/Cs^+$ at pH = 4.5 and $[Cs^+]$ = 50 µM.

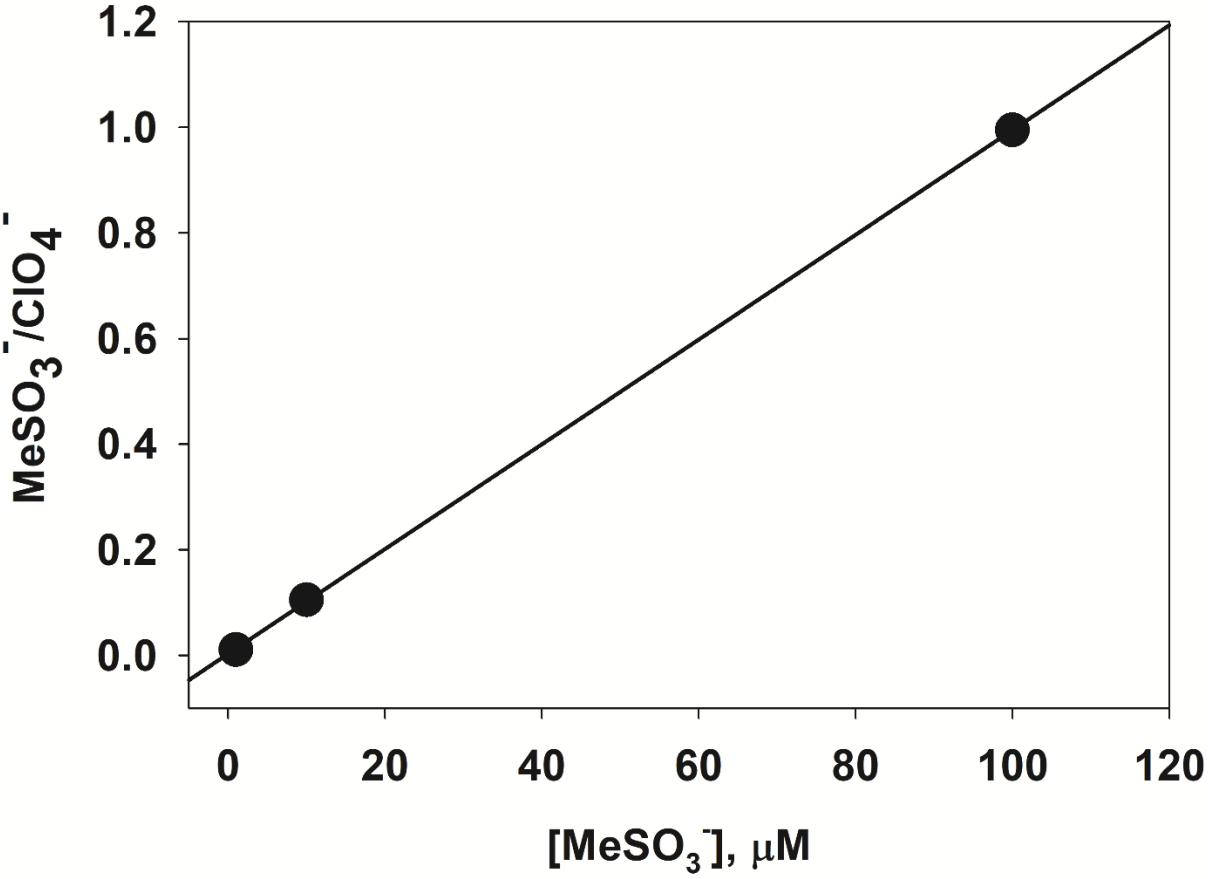

Figure 9. $MeSO_3^-$calibration curve using 1, 10 and 100 µM $MeSO_3Na$. Y-axis plots the mass signal intensity ratios of $MeSO_3^-/ClO_4^-$ at pH = 4.5 and $[ClO_4^-]$ = 250 µM.

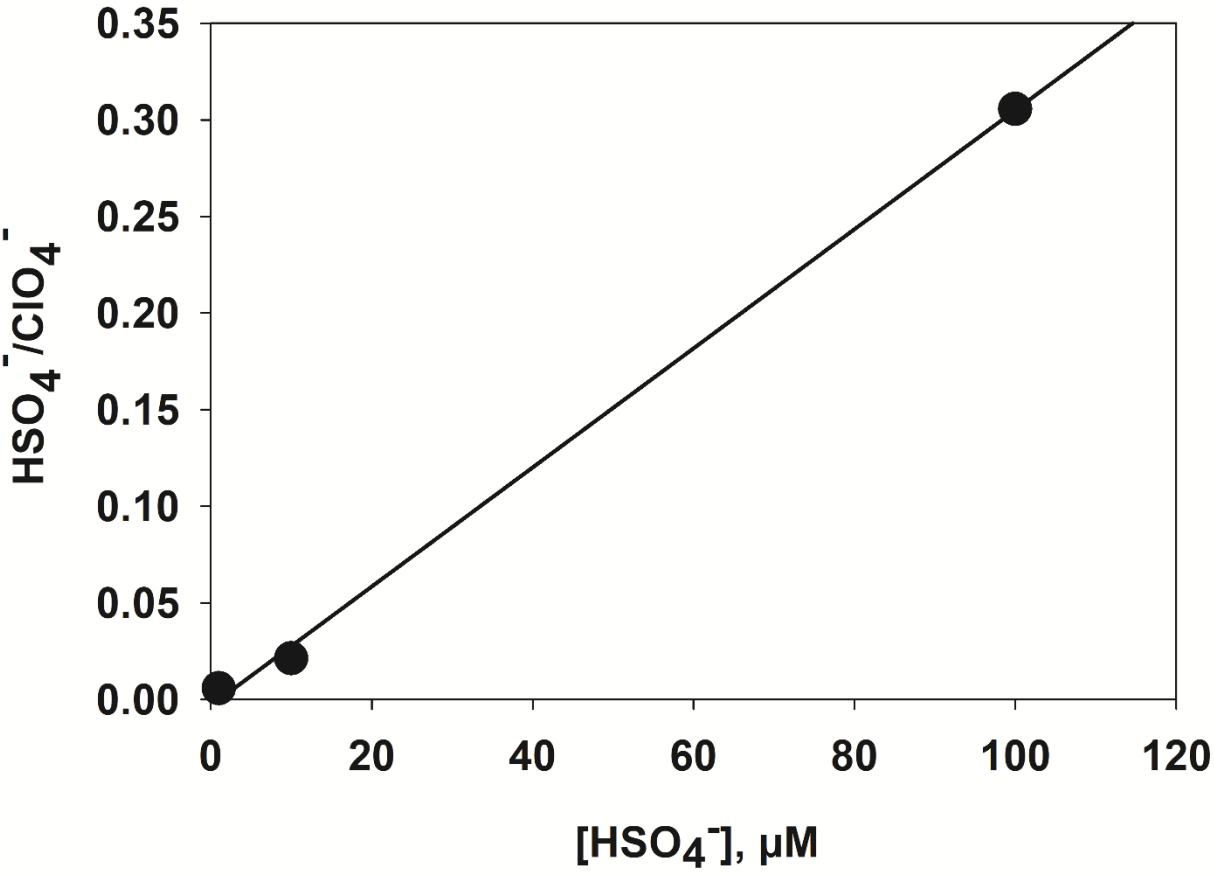

Figure 10. HSO_4^- calibration curve using 1, 10 and 100 µM $NaHSO_4$. Y-axis plots the mass signal intensity ratios of HSO_4^-/ClO_4^- at pH = 4.5 and $[ClO_4^-]$ = 250 µM.

No Ligand:

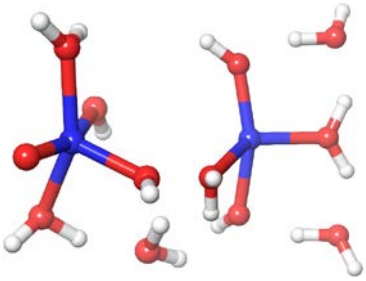

Dimethylamine:

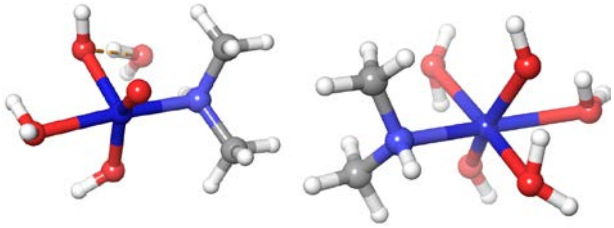

Trimethylamine:

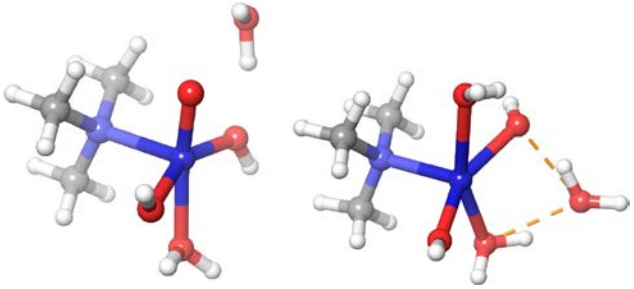

Chloride:

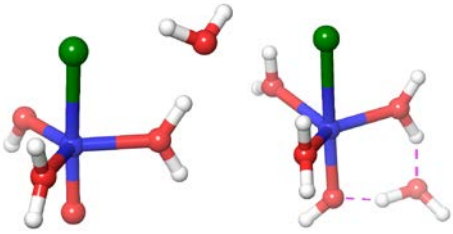

Oxalate:

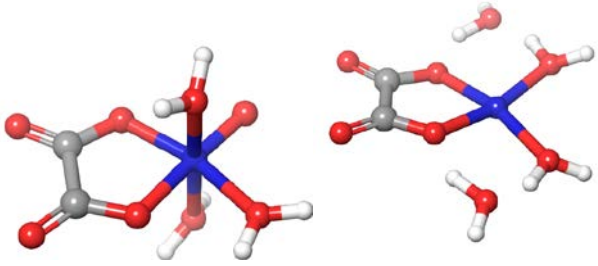

Malonate: 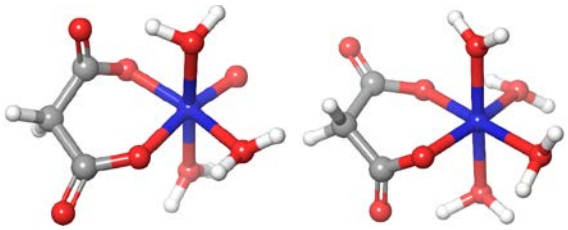

Tartrate: 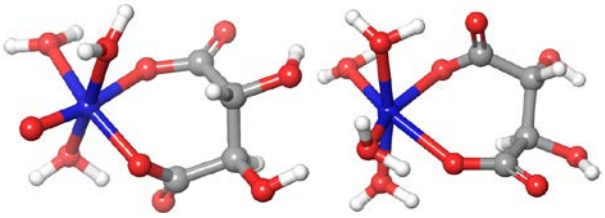

Catechol: 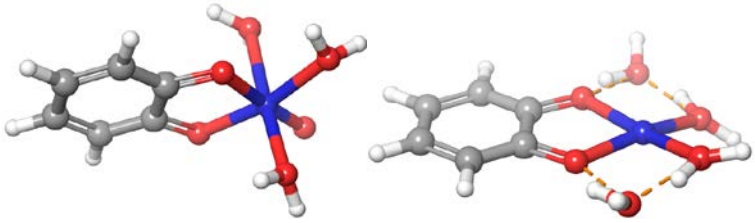

p-Benzoquinone: 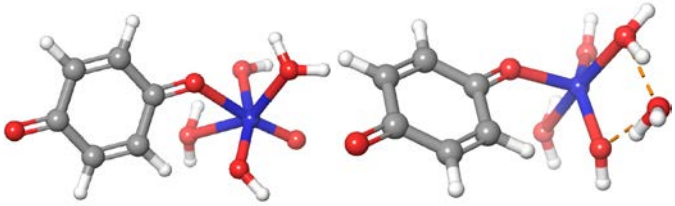

1,4-naphthaquinone: 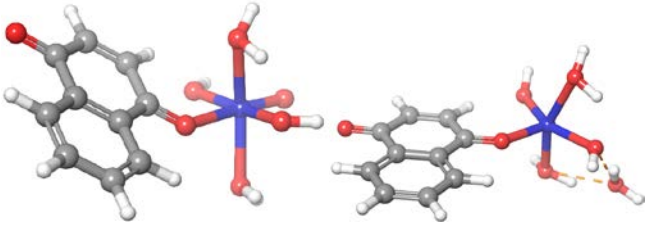

EDTA: 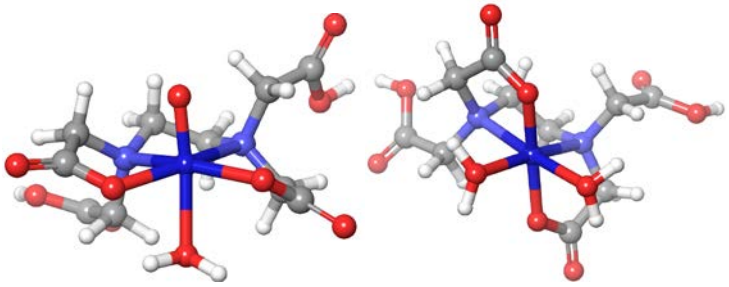

Figure 11. Optimized structures of ligated $Fe2^{+}$ and FeO_2^{+} complexes from DFT calculation.

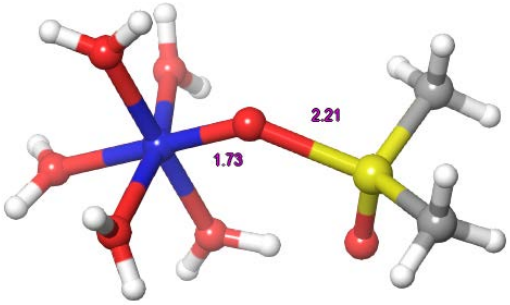

Figure 12. Optimized structure of R3 transition state.

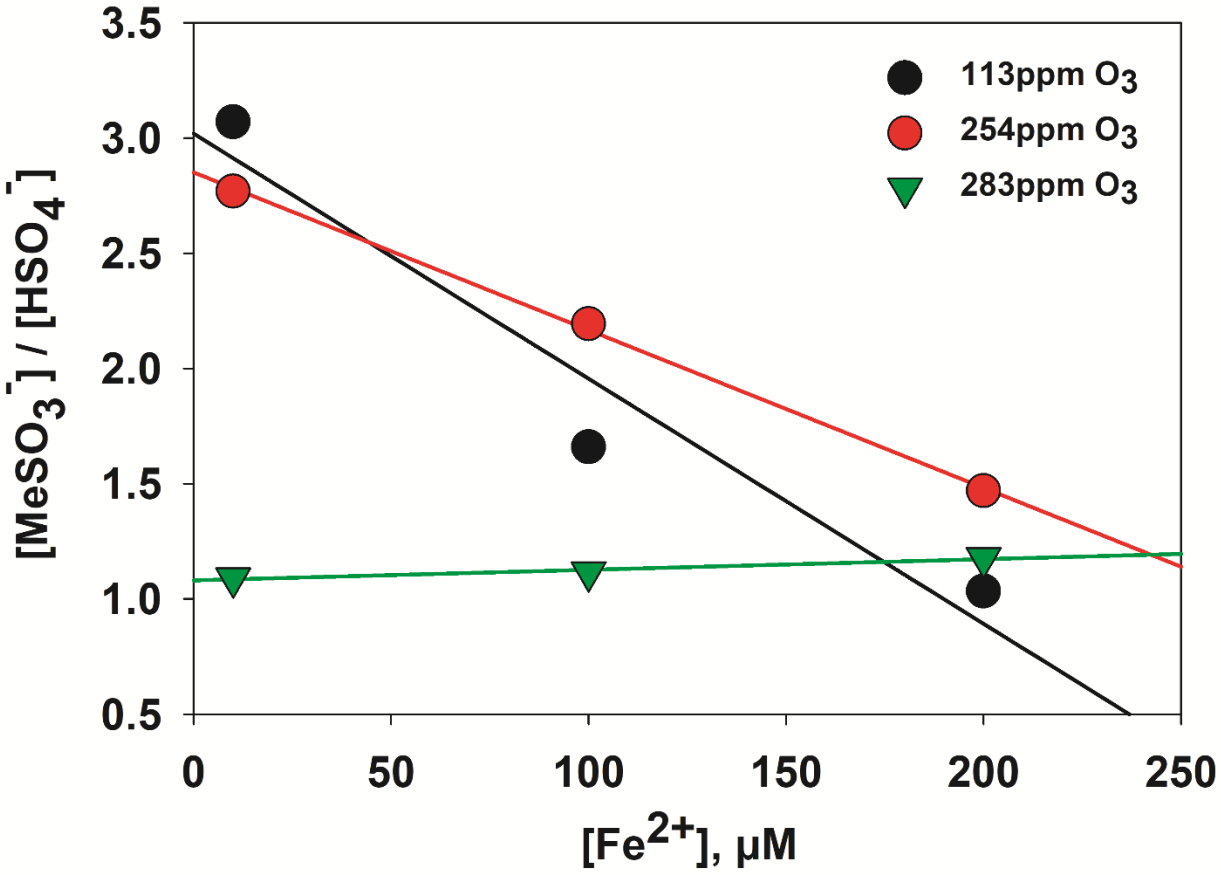

Figure 13. Relative product concentration of $MeSO_3^-$ and HSO_4^- in interfacial ozone-Fenton chemistry for 1mM Me_2SO and 100 µM $Fe(ClO_4)_2$.

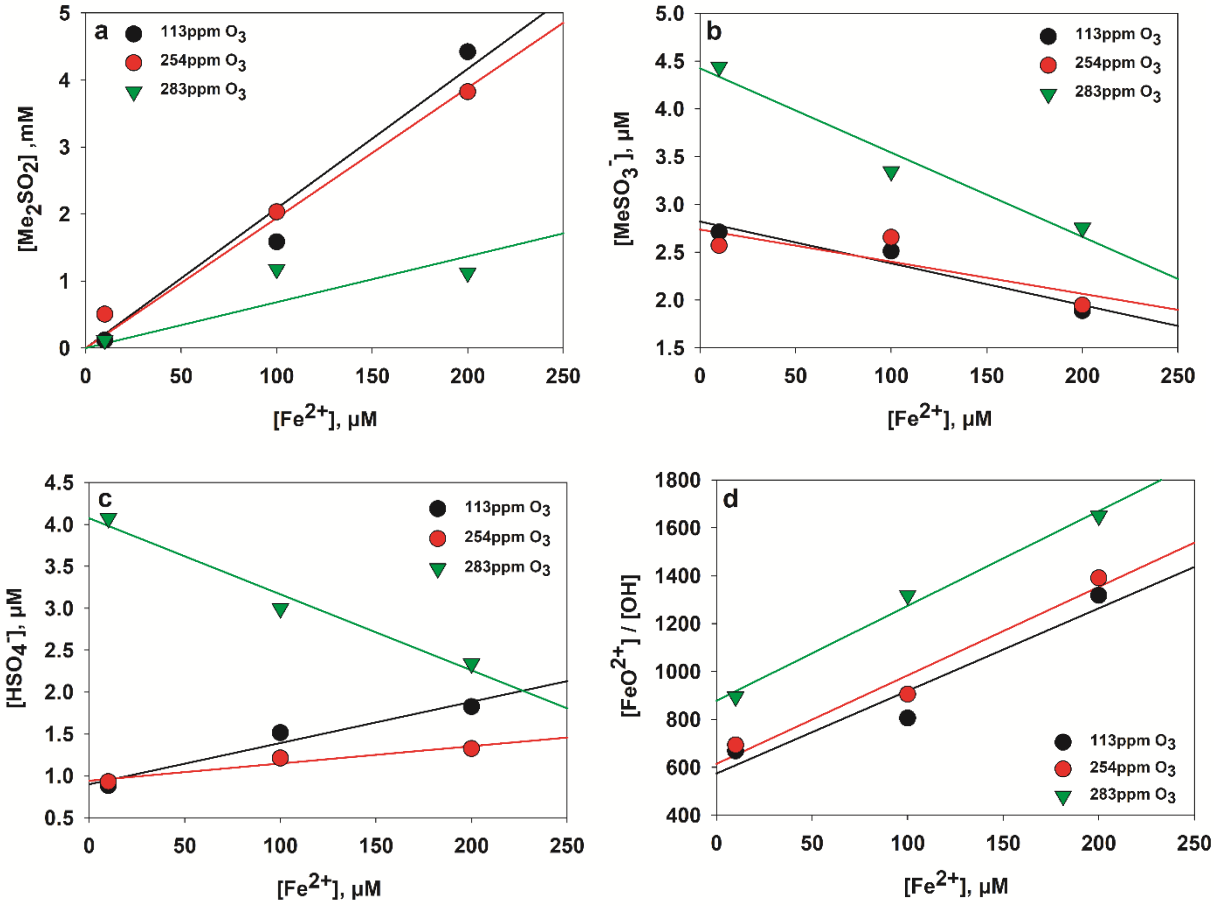

Figure 14. Product concentrations of (a) Me_2SO_2 (b) $MeSO_3^-$ and (c) HSO_4^- at different initial Fe^{II} bulk concentration ($[Fe^{II}]$) and gaseous O_3 concentration at pH 4.5 resulting from ozone Fenton oxidation of 1mM Me_2SO. Concentrations on the y-axis are the corresponding bulk concentrations of Me_2SO_2, $MeSO_3^-$ or HSO_4^- in hypothetical equilibrium with the sampled surface concentrations. The product concentrations are used to calculate the ferryl:hydroxyl pathway product concentrations ratio, represented as (d) the cumulative ferryl:hydroxyl intermediate. $CsClO_4$ and $NaClO_4$ are added as the internal standards to a total concentration of 50 µM Cs^+ and 200 µM ClO_4^-.

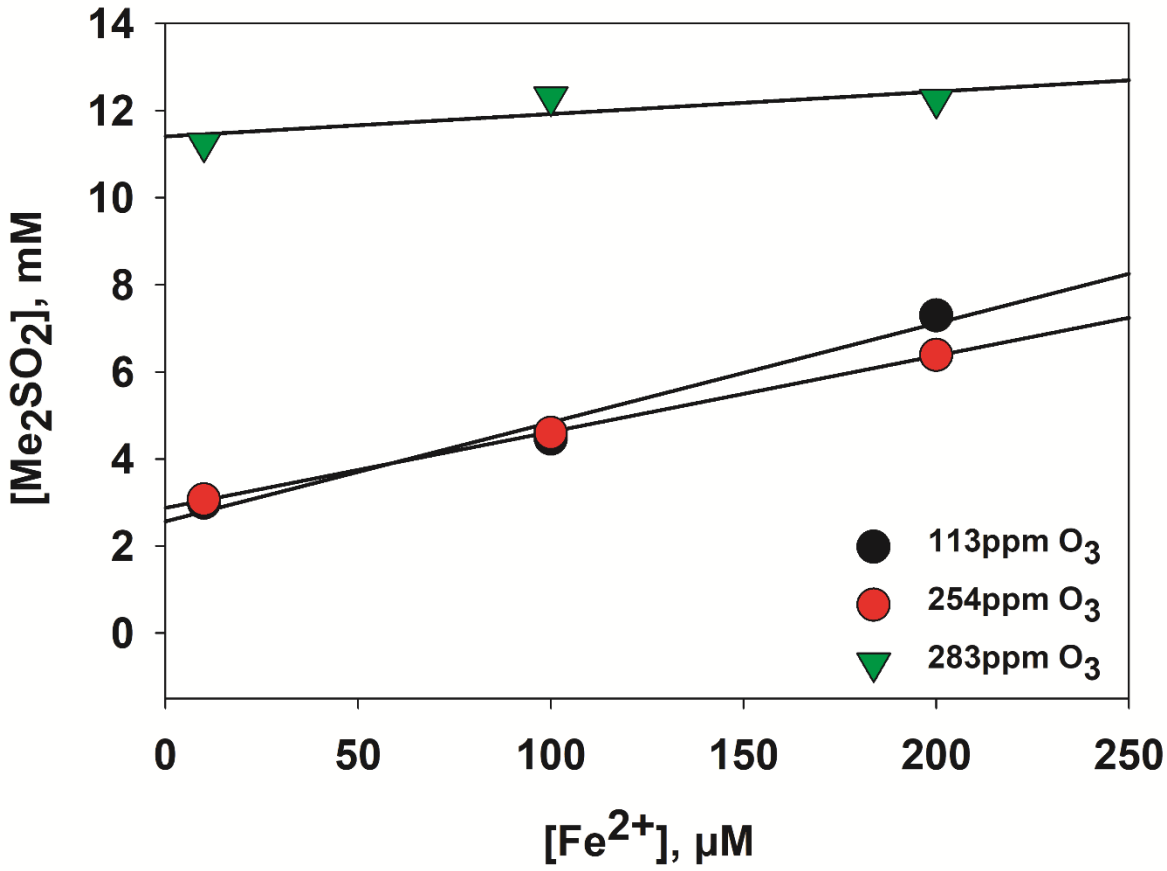

Figure 15. Me_2SO_2 product concentration at the air-water interface for 1mM Me_2SO and 100μM $Fe(ClO_4)_2$ including Me_2SO_2 produced from Me_2SO direct ozonolysis. The y-intercepts show the product concentration from direct ozonation of Me_2SO, and the slope shows the product concentration from ferryl O-atom transfer.

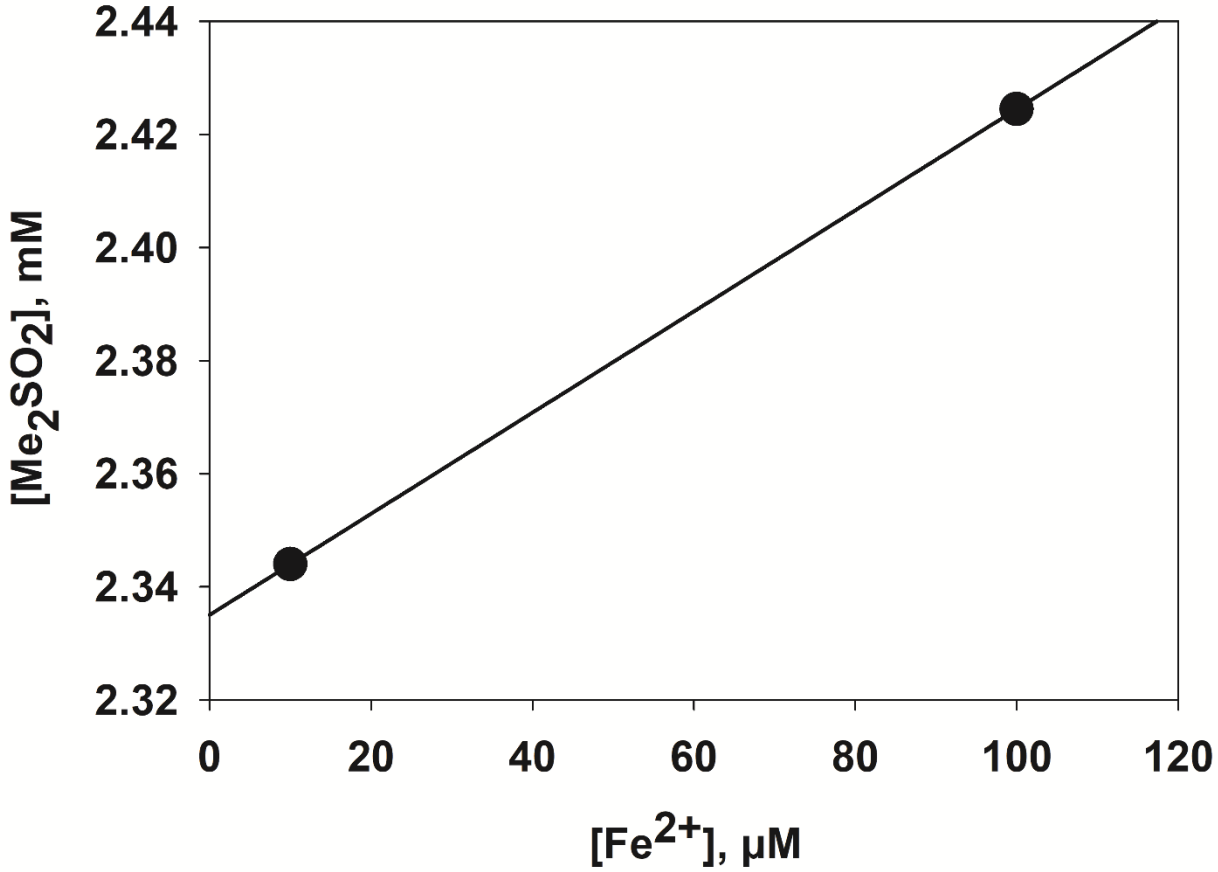

Figure 16. Me_2SO_2 product concentration in the bulk phase reaction from 10mM Me_2SO, 5mM O_3 and 100µM $Fe(ClO_4)_2$ reacting for 746 seconds, including Me_2SO_2 produced from Me_2SO direct ozonolysis. The y-intercepts show the product concentration from direct ozonation of Me_2SO, and the slope shows the product concentration from ozone-Fenton chemistry, including but not limited to O-atom transfer from ferryl species. The Me_2SO_2 product concentration originating from 100µM Fe^{2+} sets the upper bound for ferryl O-atom transfer kinetics.

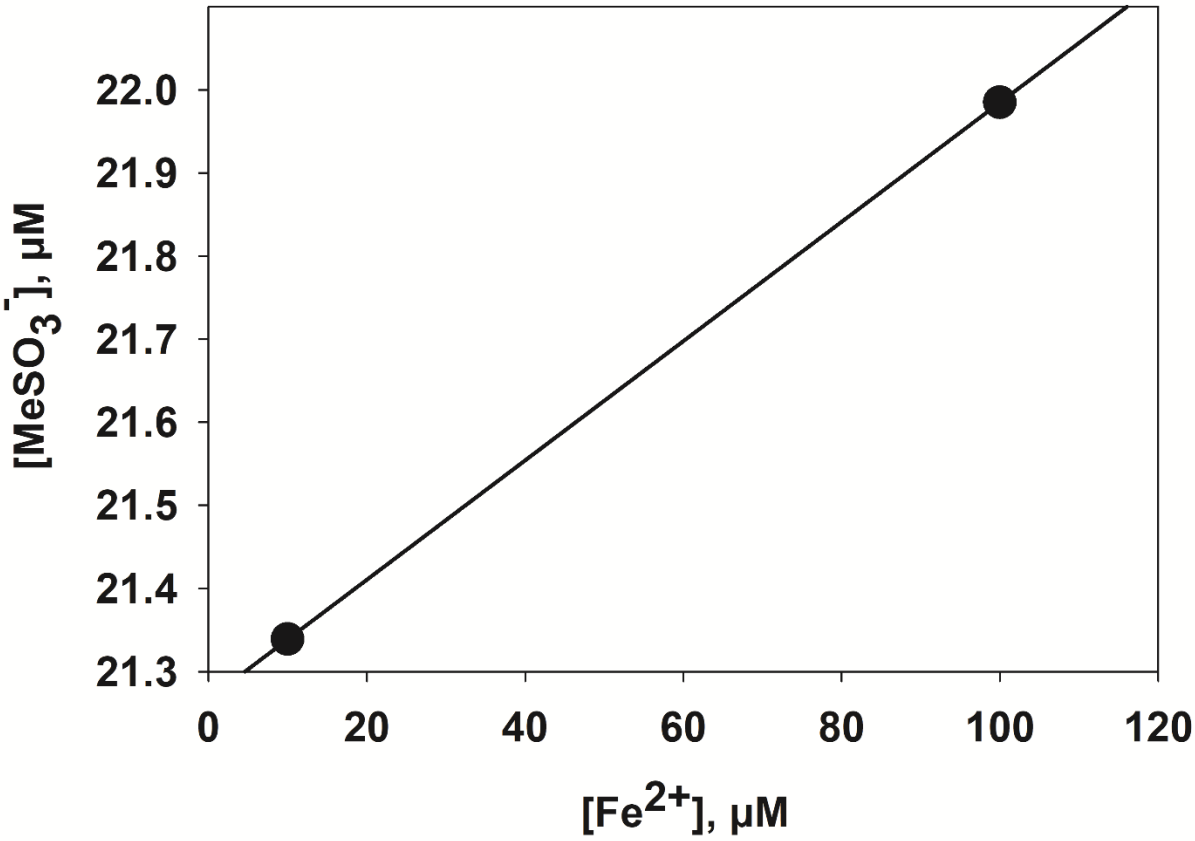

Figure 17. $MeSO_3^-$ product concentration in bulk from 10mM Me_2SO, 5mM O_3, and 100µM $Fe(ClO_4)_2$ reacting for 746 seconds. The y-intercepts show the product concentration from direct ozonation of Me_2SO, and the slope shows the product concentration from ozone-Fenton chemistry, including both ferryl and OH pathways.

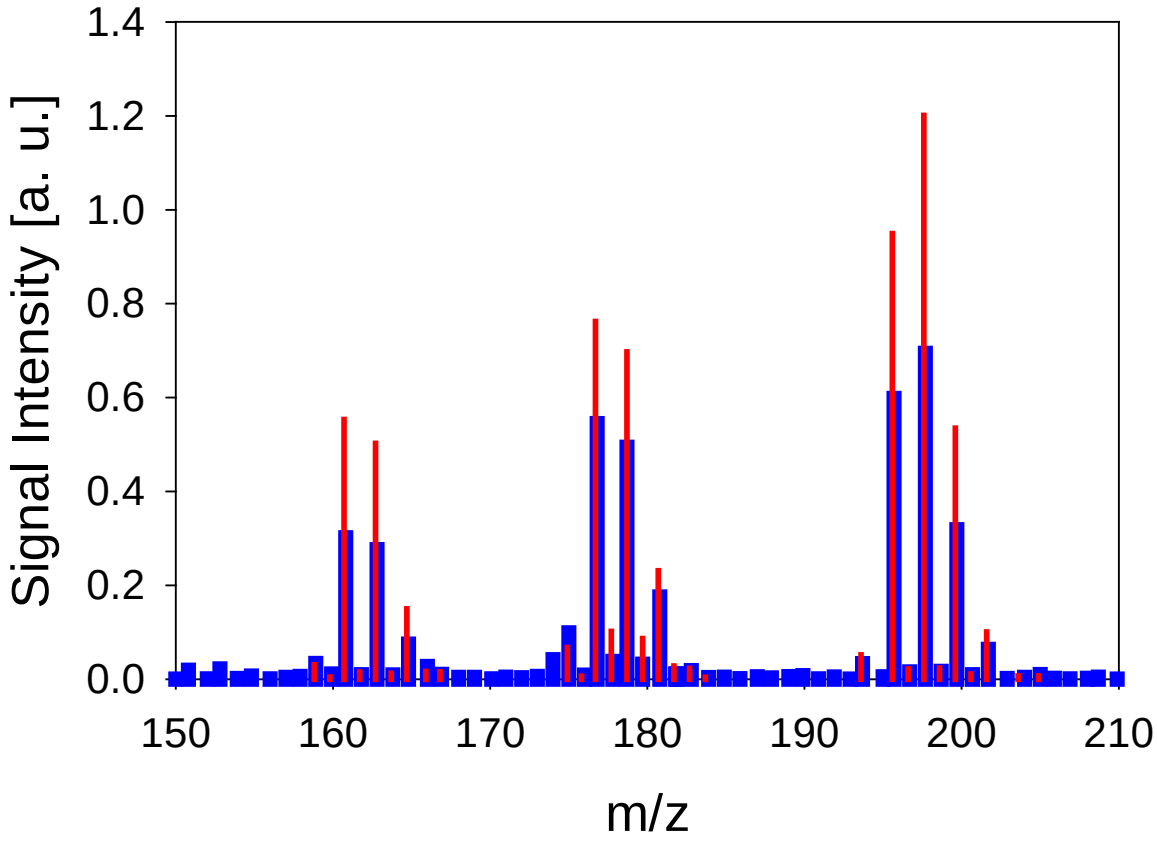

Figure 18. 5mM EDTA effect on the ozone Fenton chemistry between 10mM $FeCl_{2(aq)}$ and 283ppm $O_{3(g)}$. Blue denotes without EDTA and red with EDTA in the reaction mixture. The iron peaks are $Fe^{II}Cl_3^-$ most visible at m/z=161/163/165, $Fe^{IV}OCl_3^-$ most visible at m/z=177/179/181, and $Fe^{III}Cl_4^-$ most visible at m/z=196/198/200/202. The signal intensities are lowered for all three species with EDTA added, showing that ligands compete with Cl^- for the coordination sphere of Fe^{2+} ions.

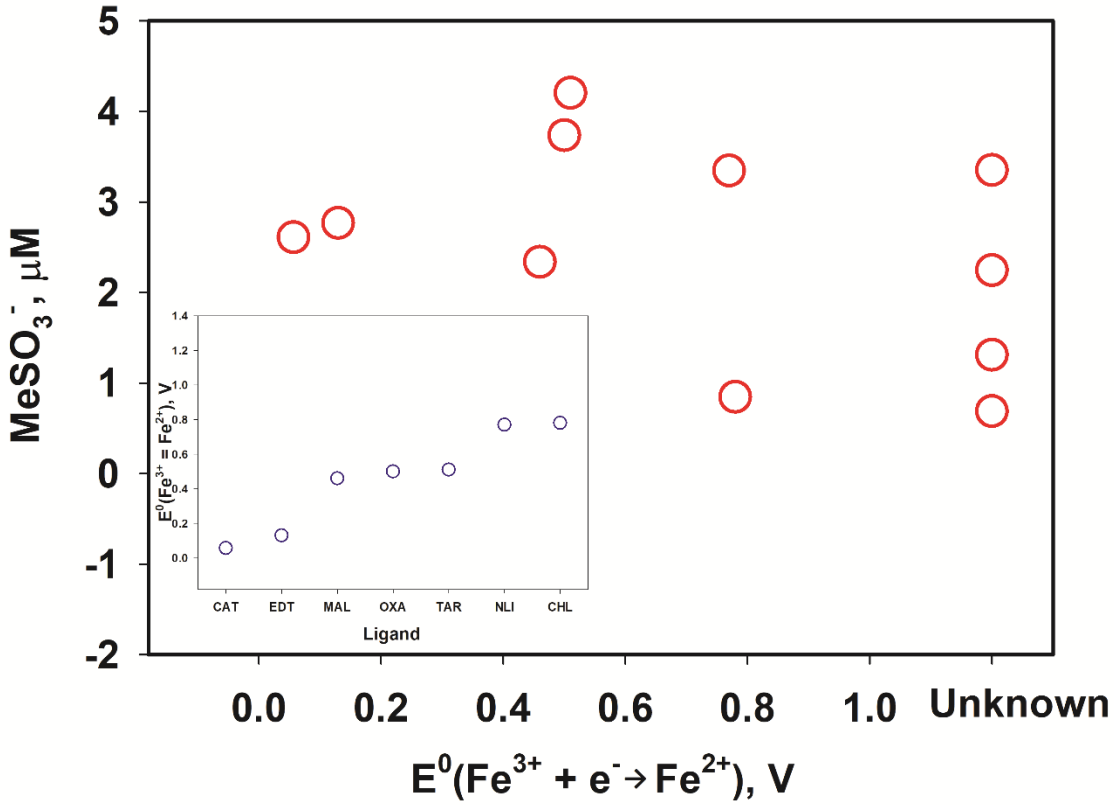

Figure 19. Methanesulfonate formation [$MeSO_3^-$] vs $E^0(Fe^{3+} + e^- \longrightarrow Fe^{2+})$ reduction potentials. The inset shows calculated $E^0(Fe^{3+} + e^- \longrightarrow Fe^{2+})$ potentials as functions of ligand. Standard reduction potentials of Fe^{3+} to Fe^{2+} in the presence of ligands shown on the x-axis of the inset are from Martell and Smith.[10] Reactants are 1mM Me_2SO, 100 μM $Fe(ClO_4)_2$, 200 μM ligand L, 283ppm O_3 at the interface of gaseous O_3 and aqueous microdroplets. Abbreviations: DMA = dimethylamine, TMA = trimethylamine, CAT = catechol, NAP = naphthoquinone, NLI = no ligand, PBQ = p-benzoquinone, MAL = malonate, CHL = chloride, OXA = oxalate, TAR = tartrate, EDT = ethylenediaminetetraacetate.

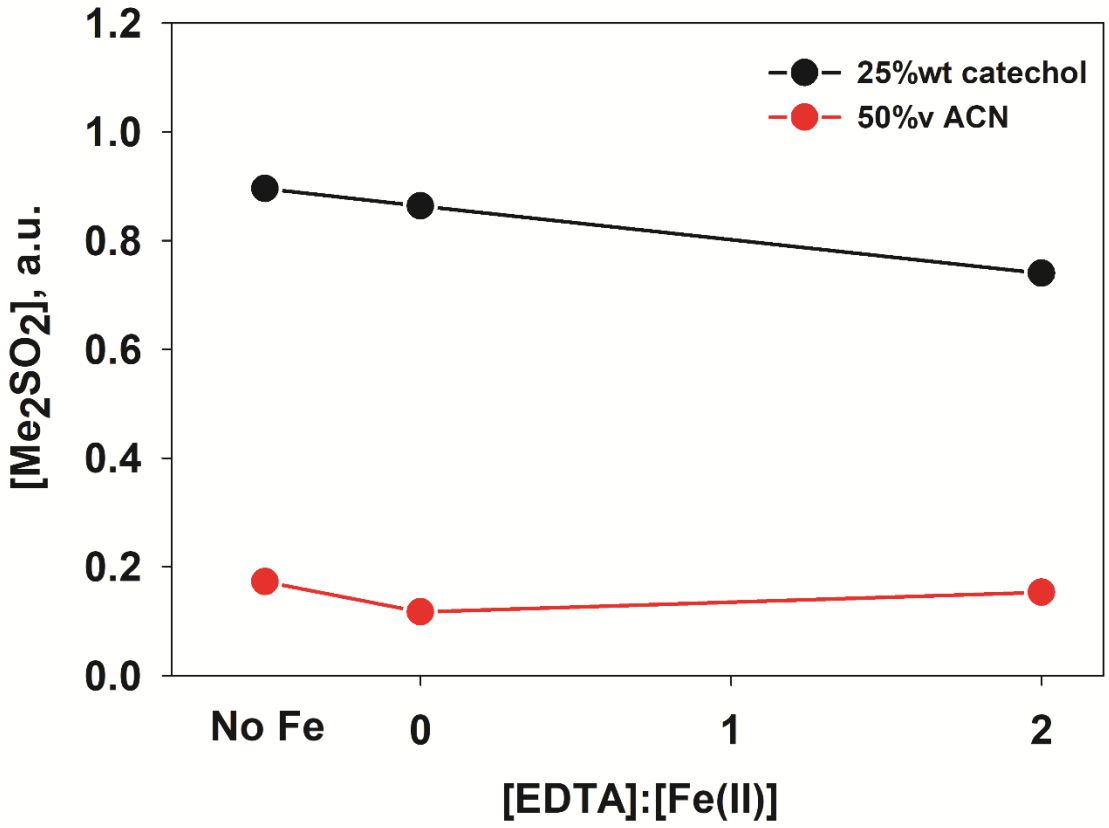

Figure 20. Ligand effect on interfacial Me_2SO_2 product concentration in 25 weight-percent catechol/water and 50 volume-percent acetonitrile/water solvents. The concentrations of Me_2SO and Fe(II) are fixed at 1mM and 100µM, respectively. $O_{3(g)}$ is at 283 ppm.

1.9 Tables

Ligand	$MeSO_3^-/HSO_4^-$
catechol	1.110045
EDTA	3.297675
malonate	1.774516
oxalate	1.867809
tartrate	1.966674
ClO_4^-	1.116289
Cl^-	15.35224
p-benzoquinone	2.344543
1,4-naphthaquinone	0.86446
dimethylamine	2.680139
trimethylamine	0.758585

Table 1. Ligand effect on the relative product concentrations of $MeSO_3^-$ and HSO_4^-. ClO_4^- denotes no ligand as perchlorate does not ligate Fe^{2+}.

Ligand	Fe=O distance (Å)	Fe(IV)-Ligand distance(s) (Å)	Fe(II)-Ligand distance(s) (Å)
No Ligand	1.65	-	-
Dimethylamine	1.65	2.05	2.18
Trimethylamine	1.64	2.17	2.17
Chloride	1.64	2.43	2.63
Oxalate	1.65	1.90, 1.93	1.98, 1.99
Malonate	1.64	1.92, 1.96	1.92, 1.96
Tartrate	1.64	1.92, 1.96	2.08, 2.23
Catechol	1.66	1.89, 1.91	1.98, 1.99
p-benzoquinone	1.65	2.16	2.01
1,4-naphthaquinone	1.65	2.12	2.03
EDTA	1.63	Fe-N: 2.26, 2.33 Fe-O: 1.95, 1.96	Fe-N: 2.20, 2.22 Fe-O: 1.91, 1.90

Table 2. Important bond distances for the Fe systems investigated. All distances are in Å. Some structures contain multiple Fe-Ligand distances due to increased denticity. Structures are depicted in Figure 4.

1.10 Acknowledgements

This project was supported by the U.S. National Science Foundation, Grant AGS-1744353. Special thanks are extended to Drs. Nathan Dalleska and Sara Lijie Li for their assistance.

Chapter 3

SARS-COV-2 INDIRECT AIRBORNE TRANSMISSION MODEL

Gu, A. Y.[#], Zhu, Y.[#], Li, J., & Hoffmann, M. R. (2022). Speech-Generated Aerosol Settling Times and Viral Viability Can Improve COVID-19 Transmission Prediction. *Environmental Science: Atmospheres*. doi:10.1039/d1ea00013f.

2.1 Abstract

Droplets during human speech are found to remain suspended in the air for minutes, while studies suggest that the SARS-CoV-2 virus is infectious in experimentally produced aerosols for more than one hour. However, the absence of a large-scale association between regional outbreaks and weather-influenced virus-laden speech-generated aerosol characteristics such as settling time and viral viability makes it challenging for policy making on appropriate infection control measures. Here we investigate the correlation between the timeseries of daily infections and of settling times of virus-containing particles produced by speaking. Characteristic droplet settling times determined by the Stokes-Cunningham equation as influenced by daily weather conditions were estimated based on local meteorological data. Daily infection data were calibrated from local reported cases based on established infection timeframes. Linear regression, vector autoregression, simple recurrent neural network, and long short-term memory models predict transmission rates within one-sigma intervals using the settling times and viral viability over 5 days before the day of prediction. Corroborating with previous health science studies, from the perspective of meteorology-modulated

transmission, our results strengthen that airborne aerosol transmission is an important pathway for the spread of SARS-CoV-2. Furthermore, historical weather data can improve the prediction accuracy of infection spreading rates.

2.2 Introduction

The novel coronavirus (SARS-CoV-2) has caused more than 240 million infections and 4.8 million deaths globally from COVID-19 as of October 19, 2021.[57] COVID-19 is known to cause considerable asymptomatic infections. Therefore, the ability to predict local COVID-19 outbreaks is imperative for effective public health management.[58] Faster flu transmission during winter months is often linked to lower temperatures and relative humidity than occur during the summer.[59] Virus-laden aerosols from infected human hosts evaporate into smaller aerosol particles at lower humidity and as a result, they take longer to settle out of the atmosphere. In addition, viruses in aerosols survive longer at lower ambient temperatures, and thus, they remain contagious for longer periods of time while airborne.[60] Speech-generated aerosols may be suspended in air for 8 to 14 minutes[61], while viruses encapsulated in aerosol droplets could remain viable for 49 hours[62-63]. Thus speech-generated aerosols are widely considered to have contributed to asymptomatic transmission of COVID-19.[61, 64-65] The fate and transport of these virus-laden aerosol droplets could be used for predicting the spread of COVID-19.

Airborne transmission of COVID-19 has been studied extensively over the past year.[66-67] Previous studies on predicting COVID-19 transmission and similar airborne transmission diseases were focused on using an infected population (SIR model)[68] or meteorological observation[69] directly as the input variables when predicting COVID transmission. Considering the non-linear relationships connecting weather to settling time and viral viability[63, 70], using weather-derived settling times and viability as input variables may improve the goodness of fit as well as elucidating additional factors affecting airborne transmission.

Meteorological conditions such as temperature and humidity affect aerosol settling velocity by affecting the final size of aerosols after equilibration with ambient moisture through

evaporation or condensation. The settling velocity of the equilibrated aerosols in the atmosphere is often calculated using Stokes' Law[71], which has been traditionally used to estimate aerosol terminal velocity at ambient temperatures and pressures. Because it assumes no-slip boundary condition, it underestimates the terminal settling velocity for small particles of size < 1 μm. In air at 25 °C, the terminal velocity accounting for slip correction is 1.24 times faster than calculated from uncorrected Stokes' Law for a 1 μm-diameter particle, and 2.2 times faster for a 200 nm-diameter particle. Stokes' Law also assumes that aerodynamic stress is transferred primarily through viscous exchange, meaning it is valid for small Reynolds number Re < 1. Cunningham later introduces a correction factor to account for particle surface slippage and the resultant Stokes-Cunningham Law applies for aerosols sizes as small as 100 nm at ambient temperature and pressure.[72] Other models, such as the one proposed by Epstein[73] and Millikan[74], are only applicable at Knudsen numbers Kn > 10, corresponding to nm-sized particles in the lower troposphere or micron-sized particles at millibar-level pressures[75].

In addition to settling time, weather also affects the viability of viruses in suspended aerosols.[76] In the case of SARS-CoV-2, high temperature, relative humidity (within 20% - 70% range) and Ultraviolet B (UVB) light produce higher decay rates,[63] which is in agreement with previous studies on an enveloped virus[77]. In a study focused on the viability of SARS-CoV-2 on surfaces, investigators reported an extension of viability over longer times at low temperatures and humidities.[78-79] Weather also affects influenza A virus viability, though the relationship depends on the specific solution medium.[80]

Given aerosol settling times and viral viability as the input variables, COVID-19 cases can be forecasted using regression analysis or machine learning models. Regression analyses such as linear regression and vector autoregression can identify key input variables among all the input variables but are limited to linear correlations only.[81-82] Machine learning algorithms can find highly non-linear correlations, but they do not reveal any intuitive relationship between the input and response variables. Machine leaning has been introduced

as a promising alternative to existing forecasting models for influenza[83] and SARS-CoV-2[84] with temperature, humidity and sunlight intensity as input variables.

Herein, we test the model fitting and prediction performance of the transmission rate of COVID-19 in the US using the settling times of speech-generated aerosols coupled with viral viability data. In order to achieve this goal, weather information, evaporated speech aerosol settling times, and viral viability are processed in regression and recurrent neural network (RNN) models to forecast SARS-CoV-2 daily transmission rates. We compared linear regression, vector autoregression (VAR), simple RNN and long-/short-term memory (LSTM) RNN in terms of prediction performance of COVID-19 transmission. We expect that inclusion of first principles such as the Köhler equation for vapor pressure reduction on aquated aerosol size and settling velocity calculation improvements should removes some of the non-linearity that models need to accommodate in order to achieve better fitting and forecasting performance. A good model fitting and prediction performance would indicate that speech-generated airborne aerosols are a significant transmission route for COVID-19 and that the weather-affected speech-generated aerosol properties may be incorporated to assist further predictive model development.

2.3 Methods

Figure 21a shows the data flow of the model from weather data to predicted SARS-CoV-2 transmission in this work. Each section of the model is elaborated in this section.

2.3.1 Data Mining

Five counties were selected for inclusion in our model development. They are Harris County, TX, King County, WA, Los Angeles County, CA, Maricopa County, AZ, and Santa Clara County, CA. The counties are representative of the top-20 most populated counties in the United States. Of the 5 counties selected none had zero-case days throughout April 2020. They also had moderately warm weather and no temperature below 0°C. When temperatures are below 0°C, additional data on water surface tension and sodium chloride solution partial molal volumes below normal melting point are needed. Constraining the predictive model to $T > 0\ ^{o}C$ avoids the complication of ice crystal formation within aquated aerosols[85]. The daily

local meteorological data, including daily average temperatures and relative humidities (RH) were obtained online from National Oceanic and Atmospheric Administration (NOAA) from 1 April to 29 August 2020. For counties with more than one station, the station with most data coverage for daily temperature and RH was chosen. The station numbers are 12960, 24233, 93134, 23183, and 23293 for Harris County, King County, Los Angeles County, Maricopa County, and Santa Clara County, respectively.

The county-level COVID-19 confirmed case counts were obtained from USAFacts.org, who collected data from the Centers for Disease Control and Prevention (CDC), and the corresponding state- and local-level public health agencies. Data was acquired on 14 September 2020 and contained up-to-date daily confirmed cases. Given the extended asymptomatic period of COVID-19, the daily confirmed cases data was processed to reflect the daily active cases based on a disease progression timeline (Figure 21b) that summarizes information provided by the CDC[86]. The daily active cases of a certain day to study is therefore the sum of daily confirmed cases for the past 12 days and future 4 days.

2.3.2 Aerosol Settling Behavior

Given the fast kinetics of water evaporation from micron-sized aerosols (seconds)[87-88] compared to their settling time from a typical human height (minutes),[89] the Köhler equation (Equation 1) is used to estimate the size of evaporated aerosols:[70]

$$\ln h = \frac{\xi_{\sigma,0}}{\xi} - \frac{c^3}{\xi^3} \quad (1)$$

where h is RH in decimal, $c = \left(\nu\left(\frac{M_w}{M_s}\right)\left(\frac{\rho_{dry}}{\rho_w}\right)\right)^{\frac{1}{3}} = 1.10$ for sodium chloride solution, $\xi = \frac{r}{r_{dry}}$ is the ratio of dry salt diameter to wet aerosol diameter, $\xi_{\sigma,0} = \frac{r_{\sigma,0}}{r_{dry}}$ is the ratio of the characteristic length scale of Kelvin effect to dry salt diameter where the characteristic length scale is calculated as follows:

$$r_{\sigma,0} = \frac{2\overline{v_w}\sigma}{RT} \quad (2)$$

in which $\overline{v_w}$ is the partial molal volume of water in the solution, σ is the surface tension of the solution-air interface, R is the gas constant and T the absolute temperature.

The speech-generated aerosols are modelled as sodium chloride solutions at physiological concentration of 80 mM, which is a typical salivary sodium concentration[90]. The initial size of speech-generated aerosols before evaporation is taken as 6 μm, which is the most abundant size according to experimental measurements[91]. The partial molal volume of water in a sodium chloride solution,[92] water vapor pressure,[93] water surface tension[94], and the binary diffusion constant of water vapor in air[95] are taken from previous experimental data or semi-empirical relationships.

The settling velocity of the evaporated aerosol of a given size is calculated using the Stokes' Law with the Cunningham correction factor shown in Equation 3:

$$V_t = \frac{\rho_p D_p^2 g}{18\mu} \times C_c \quad (3)$$

where V_t is the terminal settling velocity, ρ_p is the particle density, D_p is the particle diameter, g is the gravitational acceleration, mu is the viscosity of air, and C_c is the Cunningham correction factor calculated as follows:

$$C_c = 1 + 2.52\,Kn \quad (4)$$

where 2.52 is an empirical constant specific to air, and Kn is the Knudsen number, which is the ratio of the mean free path of the gas molecules (λ) and the aerosol diameter (D_p) as shown in Equation 5.

$$Kn = \frac{\lambda}{D_p} \quad (5)$$

Assuming ideal gas law, the mean-free path, λ, for a given gas is

$$\lambda = \frac{1}{\sqrt{2}\pi d^2\left(\frac{N}{V}\right)} \quad (6)$$

where d is the Van der Waals diameter of the gas molecule ($3.10 \times 10^{-10} m$ for N_2), and $\frac{N}{V}$ is the molecular density of gas (2.46×10^{25} at 25 °C and 1 atm total pressure). $\lambda = 95$ nm for air at 25 °C.

From the aerosol settling velocity, the settling time is calculated assuming aerosols attain their terminal settling velocity immediately after release at a height of 1.5 meters. Because the settling time is used as an intermediate variable in the model depicted in Figure 21 to check fitting and make predictions, the absolute height of release does not affect conclusions obtained.

2.3.3 Viral Viability

Viral viability is calculated using empirical linear regression with interaction by Paul Dabisch[63]. Because the regression equation is obtained from a limited range of temperature (10 - 30 °C) and humidity (20 - 70 %), we focus on counties with moderate climate where the viability calculation is valid.

2.3.4 Transmission Model

The variable describing SARS-CoV-2 transmission is the "new case percentage increase (NCP)," which is calculated as the number of new positive tests on a particular day divided by the "total number of active cases (TNAC)" on that day. The TNAC on a day is estimated by summing all positive tests from 12 days before until 4 days after the day of interest as stated above.

The timeseries data for each county are separated into a training set and a test set, with the test data set containing the last 4 days of data and the training set containing the remaining data. VAR and RNN models are developed using the training data. Subsequently, the predictive accuracy of the trained models is tested using the test data.

Linear regression analysis uses the settling times and viral viability between the day of interest and 5 days before as the input variables (total of 10). VAR uses the settling times, viral viability, and "new case percentage increase" between 1 day and n days prior to the day of interest as the input variables, where n is the order of VAR and selected by Akaike's Information Criterion. As an autoregressive algorithm, predictions of more than one day in the future are calculated using the predictions of previous days, not the actual data as in the linear regression or RNN models. Simple RNN uses the same input variables as the linear regression model, one hidden layer of 70 nodes, a max epoch of 10^5 and a learning rate of 10^{-4}. LSTM uses the same input variables as RNN, one LSTM layer of 120 units, a max epoch of 10^6 and a batch size of 72. All models use the new case percentage increase on the day of interest as the response variable, which represents the transmission rate.

2.4 Results and Discussion

In order to investigate the gravity settling of the speech-generated droplets, the settling velocity and dimensionless numbers of the Stokes-Cunningham modification were estimated for droplets of 6 μm size (Figure 27), which is used as the peak initial size of speech-generated droplets[91]. It should be noted that this size is comparable to the average diameter of cough-generated droplet size of 5 μm[96]. Thus, we use the size representing speech-generated droplets considering asymptomatic transmission of SARS-CoV-2[97], which is at its most contagious before symptom onset[98]. Figure 22 shows the estimated terminal settling velocities of an evaporated aerosol as well as its associated Reynolds number and Knudsen number at that particular size and velocity in ambient air. The density of the aerosol is set to unity in this chart for illustration purposes; estimated sodium chloride solution density accounting for evaporation is used in producing all fitting and prediction results. Because the Stokes-Cunningham equation is only applicable to $Re < 1$ and particle size > 100 nm, the estimated terminal velocity is accurate up to approximately ~10 μm and down to 0.1 μm in terms of aerosol size. Thus, the size spectrum is broad enough to encompass the entire range of sizes produced by equilibrating speech-generated aerosols with ambient moisture (*vide infra*). For the range of sizes shown in Figure 22b, $Kn << 10$. Thus, the Epstein or Millikan equations[73, 99] are not applicable in regard to the range covered (Fig. 2b). The decreasing

trend of Kn as droplet size increases also confirms the importance of surface slippage at small droplet sizes.

Droplets of an initial size of 6 μm equilibrate with atmospheric moisture and evaporate into smaller aerosols or condense into larger droplets as shown in Figure 23 a-b. Figure 23a shows the temperature effect on the size of aerosol after evaporation or condensation, which is negligible within the temperature range seen in the counties investigated. Assuming that a few seconds are needed for droplets to evaporate to an equilibrium size,[88] we further assume instantaneous kinetics, thus the temperature effects demonstrated in this work are expected to be smaller than in reality. Figure 23b shows the relative humidity effect on the size of aerosol after evaporation (below 90% relative humidity) or condensation (at 100% relative humidity). A higher relative humidity corresponds to a larger equilibrium size of droplet or aerosol as expected. An initial size of 6 μm yields a droplet of size 1 to 10 μm in equilibrium with moisture, and this final droplet size is used to calculate its settling time from the height of 1.5 m shown in Figure 23c. As expected from Figure 23a, the temperature effects on the settling velocity are minimal. The relative humidity effect on settling time is significant, yielding as short as 1 min at 100% relative humidity and >20 min at <10% relative humidity. The evaporation and settling calculations agree with the classic Wells model.[89, 100] Similarly, the SARS-CoV-2 virus half-life is plotted as a function of ambient temperature and relative humidity in Figure 23d. Lower temperatures and humidities yield longer viral half-lives. However, the relationship is highly nonlinear. The non-linearity poses a challenge to previous models[69, 101-102] using meteorological data directly as input variables. Current transmission models incorporating weather data as input variables have varying goodness of fits and correlation significances that may be due to how the meteorological variables were used[85]. For example, humidity has been factored into models as relative humidity,[103] absolute humidity,[104] or dew point.[105]

The correlation between humidity and transmission may be related to the hydrophilic interactions between water and the proteins on the outer surface of SARS-CoV-2 virus via hydrogen bonding.[106] The range of virus half-lives varies from several minutes to over an

hour with typical ranges of temperature and humidity in April. These results underscore the potential effect of weather on airborne virus transmission. Results show that the weather affects the fate and transport of speech-generated, virus-laden droplets by changing the settling times and viral half-lives, and thus these intertwined effects may not be captured by a simple linear model.

To establish an effective weather-based model for COVID-19 epidemic prediction, regression analyses (LR and VAR) and machine learning models (RNN and LSTM) were compared for 5 U.S. counties. Figure 24 shows the timeseries of daily case percentage increase in the different US counties. The model fittings follow the major trends of the actual data and capture most of their peaks and troughs; the actual data of the last 4 days also fall inside the one-sigma prediction intervals despite simplicity of the models used. The goodness of fit and the prediction accuracy generally rank as follows: LSTM > simple RNN > LR > VAR (see r^2 for fitting and residual sum of squares (RSS) for prediction in Table 3a-b). Considering a key difference between VAR and the rest of the models are the use of auto-regressively predicted settling times and viral viability data versus actual data starting from the second day of prediction, the lowest fitting and prediction accuracy of VAR suggests inaccurate aerosol settling times and viral viability predictions from past data as expected. It is clear that accurate weather-originated data input is required to predict transmission rates accurately. VAR also includes past transmission rate data as an input, which is not included in the other models explored. This suggests that past transmission is not a significant input variable for predicting future transmission compared to the two weather-originated variables as normalized into a percentage increase. Improved fitting for LSTM over simple RNN suggests that weather beyond 5 days prior affects current transmission. Better fitting and prediction performance of neural network models compared to LR suggests nonlinearity in the correlation between settling time, viral viability, and transmission rate, even though reasonable linear correlations are observed. For example, the r^2 values for the counties considered vary from 0.36 to 0.80 with an average of 0.59, achieved using input variables capturing two types of weather influences on transmission. Variability in goodness of fit

among the counties may be explained by local residents, who have delay in time from the onset of symptom to getting a COVID test.

To better understand how weather-originated aerosol settling times and viral viability affect transmission, the contours of model predictions are shown in Figure 25. The ranges of settling times and virus half-lives are determined in part by the local temperature and RH range during April, for each county of study. Note that the data points used to generate the contour plots are not uniformly distributed inside the contours, and the data to be predicted may not lie within the range of training data (see Figure 28). Although UV intensity is not a direct input variable in this model, it positively correlates with temperature[107] and is, therefore, indirectly taken into account in this model.

Counties have faster transmission at longer aerosol settling times or longer virus half-lives. These results indicate that active-virus-laden aerosols are a major pathway for COVID transmission. The only exception to this claim was seen for Santa Clara County for which there appeared to be faster transmission at low viral viability and settling times leading to a less accurate prediction compared to the other counties that were analysed in Figure 25. Harris, King and Maricopa counties show faster transmission with a longer virus half-life, while LA County had increased transmission rates at longer settling times. The LR, VAR and simple RNN predictions show clear trends, while the trend of LSTM predictions indicates hotspots for easy transmission in the 2D space of viral viability and aerosol settling times. This may be indicative of the small training data set used, considering the high accuracy of fitting and predictions by LSTM in Figure 24. The different trends between LA County vs. Harris, King and Maricopa counties may be a result of their different policies and human behaviours not captured by the input variables in this work. Future work in the training of an LSTM model with sufficient data over a wide range of weather conditions from all seasons may reveal a clear trend of correlation similar to the LR, VAR, and simple RNN models in this work.

The performance of transmission rate prediction based on aerosol settling times and viral viability was also studied with an extended dataset of Maricopa County from May to August

2020, as shown in Figure 26. The r^2 values are 0.172, 0.579, and 0.999956 for linear regression, simple RNN, and LSTM, respectively. Like the April data, LSTM has the closest fitting, followed by the simple RNN, and a linear regression. All three models have similar prediction accuracies, with RSS values of 0.0110, 0.0156, 0.0160 for linear regression, simple RNN, and LSTM, respectively. The matching performance of these 3 models are also observed in April Maricopa County data. The observed increase in new cases line falls within the one-sigma prediction interval for the last 21 days of available data.

The prediction from weather-driven settling times and viral viability to transmission rate in this work corroborates with previous findings that transmission is faster at low temperatures and humidites for COVID in major global cities from Nov 2019 – Feb 2020,[108] in the US using state-level data over Jan – Apr 2020,[109] and for Singapore using data from Jan – May 2020[69]. Respiratory droplets travel can travel three times farther at lower temperatures and higher humidity compared to typical dry and hot environments.[110]

It should be noted that not all published work supports a link between weather and transmission. Linear machine learning models failed to establish the correlation between state-level (Italy and US) or country-level (rest of the world) transmission and meteorological data.[103] This is most likely due to the non-linearity in linking temperature and humidity data to other variables that are important factors in transmission. For similar reasons, a recent multilinear regression model found no significant correlation between temperature, humidity and the basic reproductive number R_0 of transmission.[111] However, the lack of correlation between meteorological data and COVID transmission in China during early 2020 may be a result of strong policy changes overshadowing any weather effects.[112]

Other works have analysed the link between virus-laden aerosol settling and SARS-CoV-2 transmission from different perspectives.[61, 65, 113] Smith et al. provided a useful model that assesses aerosol transmission of SARS-CoV-2 through respiratory droplet physics.[113] TheirThe study calculated the number of virus particles inhaled via indirect airborne transmission by calculating the persistence (settling time) of cough-generated aerosols, and concluded that aerosol transmission is a possible but not efficient route of transmission of

SARS-CoV-2.[113] This conclusion as well as evidence suggested by Stadnytskyi et al.[61] and Anfinrud et al.[65] agree with the conclusion of the present work to the extent that indirect airborne transmission is a possible route of transmission of SARS-CoV-2. The WHO, in the most recent update (Apr 30, 2021), has also acknowledged aerosol transmission as one of the major routes of transmission for SARS-CoV-2.[114] Homogeneity of the aerosols in the space studied is often assumed in these approaches to translate aerosol persistence to aerosol inhaled, which can be far from reality[91]. One advantage of this work is that by predicting transmission from aerosol persistence (and virus viability) via data analysis tools, homogeneity is not assumed. Because the infection risk assessment is embedded in the data analysis step connecting aerosol persistent and transmission, mathematical infection risk assessment models such as Wells-Riley and dose-response are also not required in this work. This approach reduces uncertainties introduced into the model as the infection threshold of SARS-CoV-2 is still unclear[115].

A key assumption in the models presented is that the timeframes of virus transmission, disease progression, test-to-results, and hospitalizations are consistent across a studied population, their location, and time span. However, timeframes could actually be fluctuating and thus undermine the accuracy of our model predictions. For example, since COVID case data that is reported may have inherent time delays due, for example, to the shortage of test kits. Delays are an important parameter in this study, and thus model fitting residuals associated with this input variable cannot be eliminated. Another underlying assumption of this study is that the fraction of asymptomatic infections of total infections is constant. However, this is still unknown to the best of our knowledge. Our models also have simplifications that may be additional sources of error. These simplifications include that a sodium chloride solution, which is used as a surrogate model of physiological fluids, is a good proxy for virus-laden aerosols and that the surface tension of an aerosol droplet is only a function of its temperature and solute concentration. The neural network models use a random set of parameters initially for each neuron, and the optimized result can be dependent on this initial set of parameters, if they are actually too different from the optimal set.

Although the models in this work use the outdoor weather input variables and transmission can occur indoors, the outdoor temperature correlates positively with the indoor environment[116-117]. The correlation coefficient (slope of linear regression), however, depends on the season and location. For example, Massachusetts has $T_{outdoor} \sim 0.04T_{indoor}$ at $T < \sim 10°C$, and $T_{outdoor} \sim 0.41T_{indoor}$ at $T > \sim 10°C$.[118] South Korea has $T_{outdoor} \sim 0.13T_{indoor}$ at $T < \sim 15°C$, and $T_{outdoor} \sim 0.47T_{indoor}$ at $T > \sim 15°C$.[119] The indoor absolute humidity also tracks the outdoor humidity across seasons and diverse locations.[117, 120-121] As a result, the outdoor transmission risk predicted in this work tracks with, and can be used as a surrogate for the indoor transmission risk.

Control measures such as mandatory mask-wearing and lockdowns are not accounted for by two input variables in this work. We limit our scope to April in Figure 24 when nationwide lockdown was still in effect to minimize this variable in terms of its influence on transmission. The extended-time analysis on Maricopa County for May-August in Figure 26 has lower fitting and prediction accuracy compared to the April results as shown in Table 3c. The lower accuracy for longer time periods of analysis may be the result of encompassing more non-weather-related events, such as a significant increase in mask-wearing and the mass public protests of 2020. Although it is possible that the models presented in this work are not capable of handling data over longer times, the RNN models typically benefit from additional training data to improve prediction accuracy. They are expected to have improved prediction performance for longer study times, if non-weather-related events would be represented in the model.

2.5 Conclusions

Seasonality of airborne COVID transmission may be explained in part by weather-induced changes in the aerosol settling times and virus viability. We use Stokes' sedimentation model with a Cunningham correction factor for surface slippage in order to estimate the settling times of speech-produced aerosols after evaporation for $Re < 1$ and $Kn << 1$. SARS-CoV-2 viral viability is estimated using an empirical relationship from local historical weather data. Linear regression, vector autoregression, and recurrent neural network models using the

settling time, viral viability and past transmission rate successfully predict future transmission rates within one-sigma prediction interval. Airborne speech-generated aerosol transmission is a significant transmission route of SARS-CoV-2. Including aerosol settling time and viral viability from historical weather data as input variables can improve the accuracy of transmission rate prediction. Corroborating with publications and public actions over the past year, the findings of this study support implementation of control measures including social distancing, enforcing mask wearing, and systematic preventive measures such as improved ventilation in both community and healthcare settings.

Overall, the evidence on weather influence of transmission has been contradictory and inconclusive. We note that the present work does not aim to prove that aerosol settling time and virus viability are exclusively important on predicting transmission rate. The fitting and prediction performance of the models presented suggests that weather plays a considerable role in transmission. Thus, the incorporation of weather-derived, transmission-mechanisms-based input variables, including aerosol settling times and virus viability, into epidemiological prediction model may worth further investigation. Future work in model development should also include additional variables that play a role in airborne or surface-based transmission such as wind speeds, turbulence (especially those created by speech which can lengthen the suspension time by 30-150 times[122]), and UVB intensity. Datasets should include more locations outside of the US where the weather system may be different. Furthermore, the study periods can be extended to allow for better machine learning algorithm training.

2.6 Supplementary Note

Code for this work is available at: https://github.com/zhuyanzhe98/evaptransmission

2.7 Figures

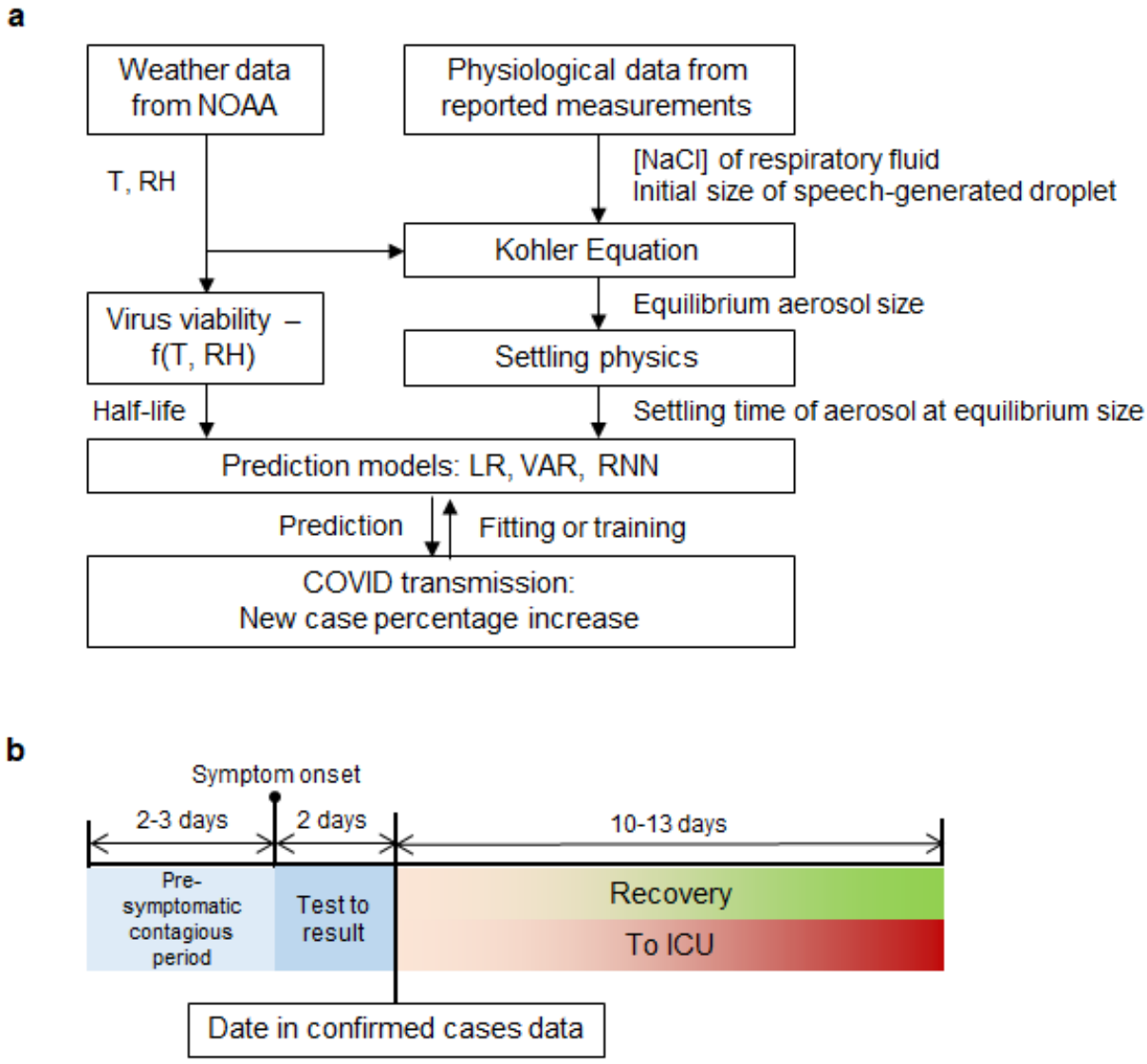

Figure 21. (a) illustration showing the model data flow in this work (b) typical COVID-19 progression around the date of positive test result. The three periods are: the pre-symptomatic contagious period, the wait period to obtain the test result after taking the test, and the recovery period at the end of which the patient is modelled as either recovered and no longer contagious, or entering the intensive care unit (ICU) and isolated from the public. We assume that the patient takes the test at the onset of symptoms. Under this assumption,

a positively tested patient is considered contagious in our model from 4 days before until 12 days after the positive test result.

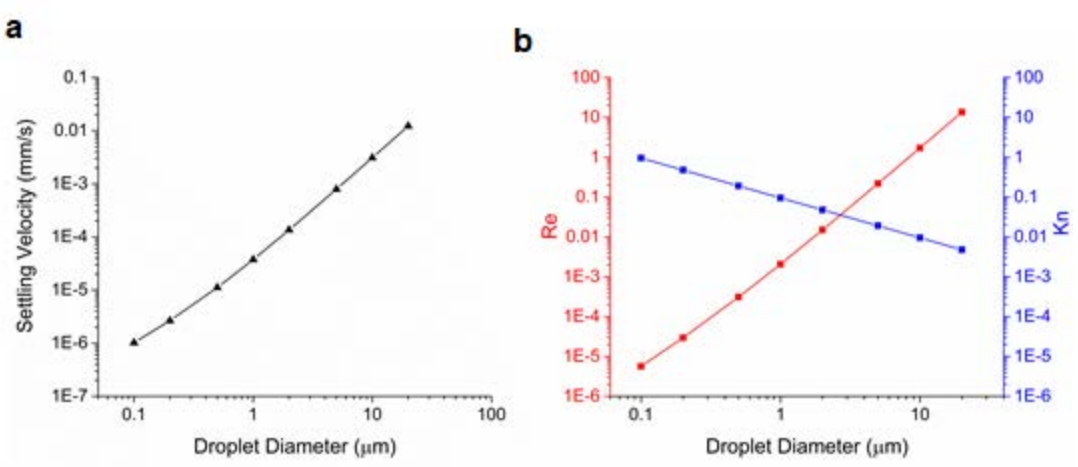

Figure 22. (a) Calculated settling velocities of aerosols of varying sizes using Stokes-Cunningham Law. (b) The Reynolds number (Re) and Knudsen number (Kn) of droplets of varying sizes. At Kn < 10, the Stokes-Cunningham Law is the most applicable first-principle relationship to calculate settling velocity.

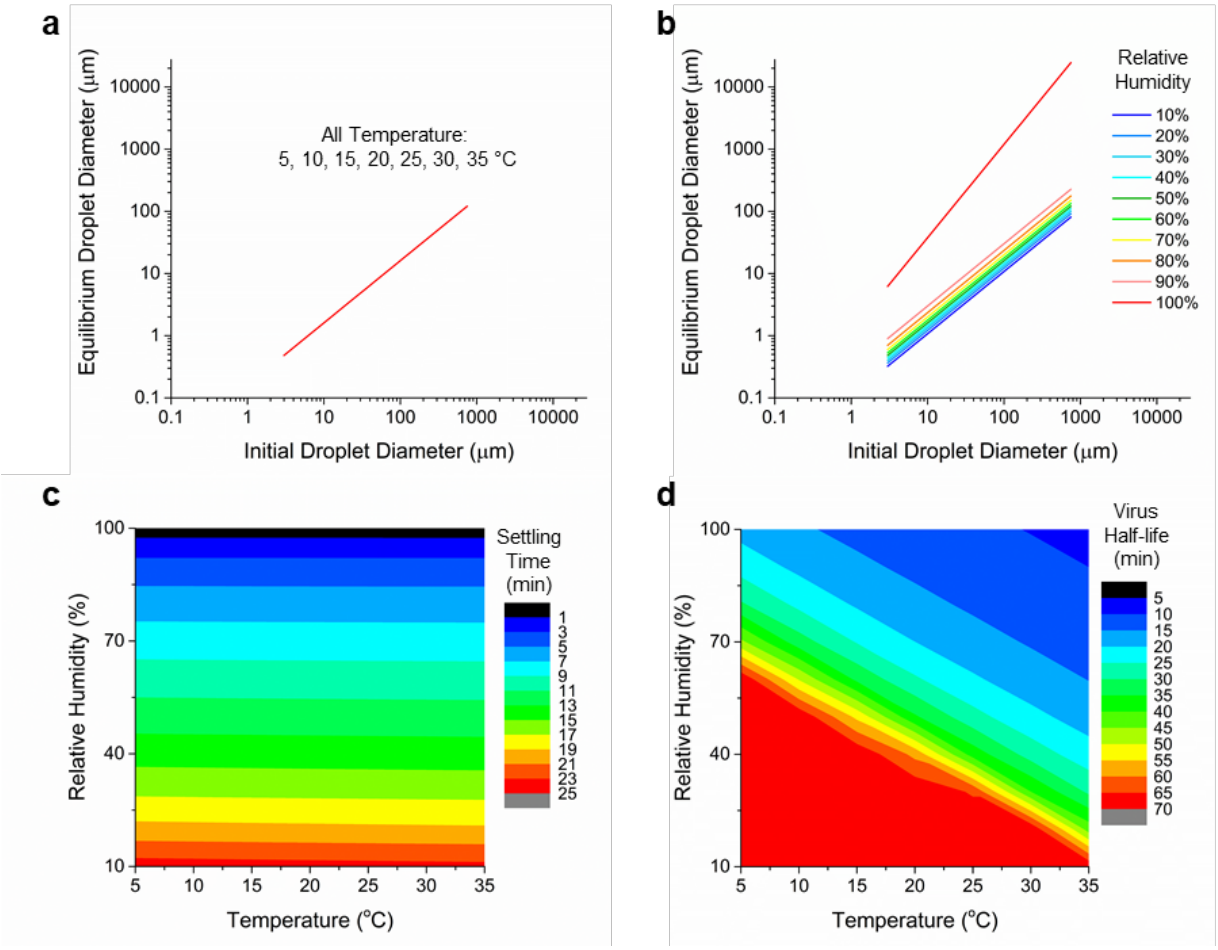

Figure 23. Evaporated aerosol sizes derived from the Köhler equation based on an initial size at different ambient (a) temperatures at 50% relative humidity and(b) relative humidity at 25 ℃. (c) Calculated settling times obtained from the empirical model using 6 μm as the initial droplet size and (d) viral viability at different ambient temperatures and relative humidity.

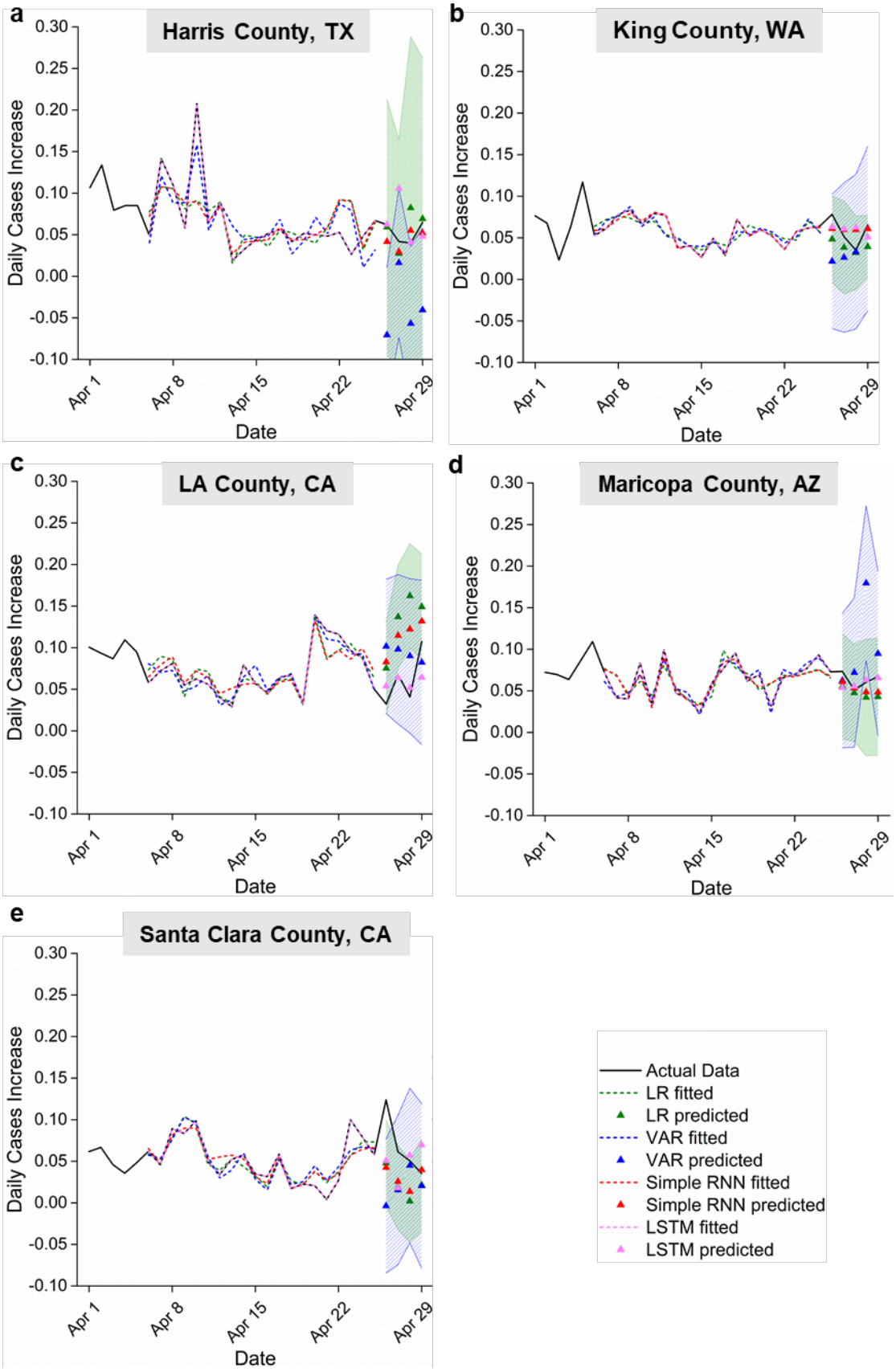
a
Harris County, TX
b
King County, WA
c
LA County, CA
d
Maricopa County, AZ
e
Santa Clara County, CA
Daily Cases Increase
0.30
0.25
0.20
0.15
0.10
0.05
0.00
-0.05
-0.10
Apr 1
Apr 8
Apr 15
Apr 22
Apr 29
Date
Actual Data
LR fitted
LR predicted
VAR fitted
VAR predicted
Simple RNN fitted
Simple RNN predicted
LSTM fitted
LSTM predicted

Figure 24. Timeseries of daily case percentage increase in decimal format for April 2020 in counties studied. The predicted daily case increase of the last 4 days are shown as triangles with their associated one-sigma prediction intervals. Dashed lines show the model fitting from the 6th day to the 25th day of April. No fitting data obtained from the model for the first 5 days because they would require weather data from March (up to 5 days prior). LR: linear regression; VAR: vector autoregression; Simple RNN: simple recurrent neural network; LSTM: long-/short-term memory recurrent neural network. The green filled areas represent 95% confidence intervals for LR predictions. The blue patterned areas represent 95% confidence intervals for VAR predictions.

Harris County, TX
King County, WA
LA County, CA
Maricopa County, AZ
Santa Clara County, CA
LR
VAR
Simple RNN
LSTM
Daily cases increase fraction
0.02
0.04
0.06
0.08
0.10
0.12
0.14
0.16
0.18
0.20
0.22
0.24
Virus Half-life (min)
Setting Time (min)

Figure 25. Contour plots of the daily case percentage increase as a function of settling time and viral viability (represented by half-life) for different counties. Colour shows the daily case percentage increase in decimal. LR: linear regression; VAR: vector autoregression; Simple RNN: simple recurrent neural network; LSTM: long short term memory recurrent neural network.

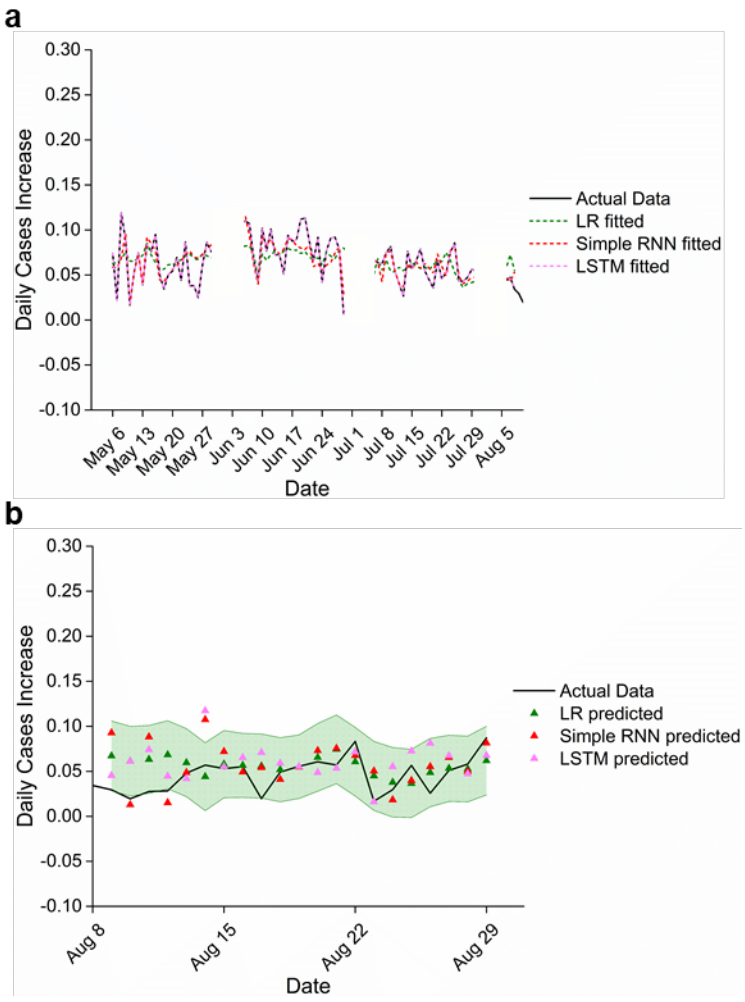

Figure 26. (a) Fitting and (b) predicted daily new case percentage increase for Maricopa County from May to August 2020. Interrupted data in (a) is due to interrupted weather history data from NOAA. Error bars show one-sigma prediction intervals. The training data in (a) are 75 days long and the testing data in (b) are 21 days long. LR: linear regression; Simple RNN: simple recurrent neural network; LSTM: long short term memory recurrent neural network. The green filled areas represent 95% confidence intervals for LR predictions.

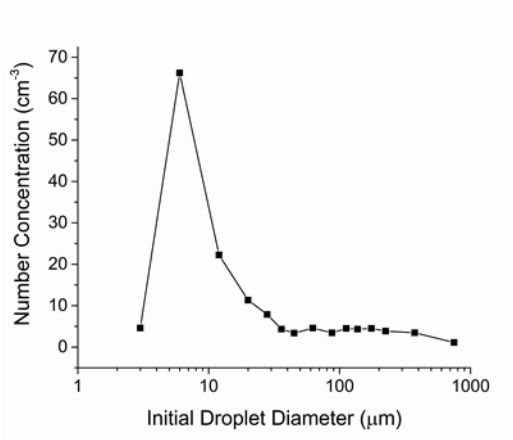

Figure 27. Size distribution of speech-generated droplets before evaporation measured by Morawska et al.[91] The peak number concentration is at 6 μm and is used as the input to the Köhler equation in this work.

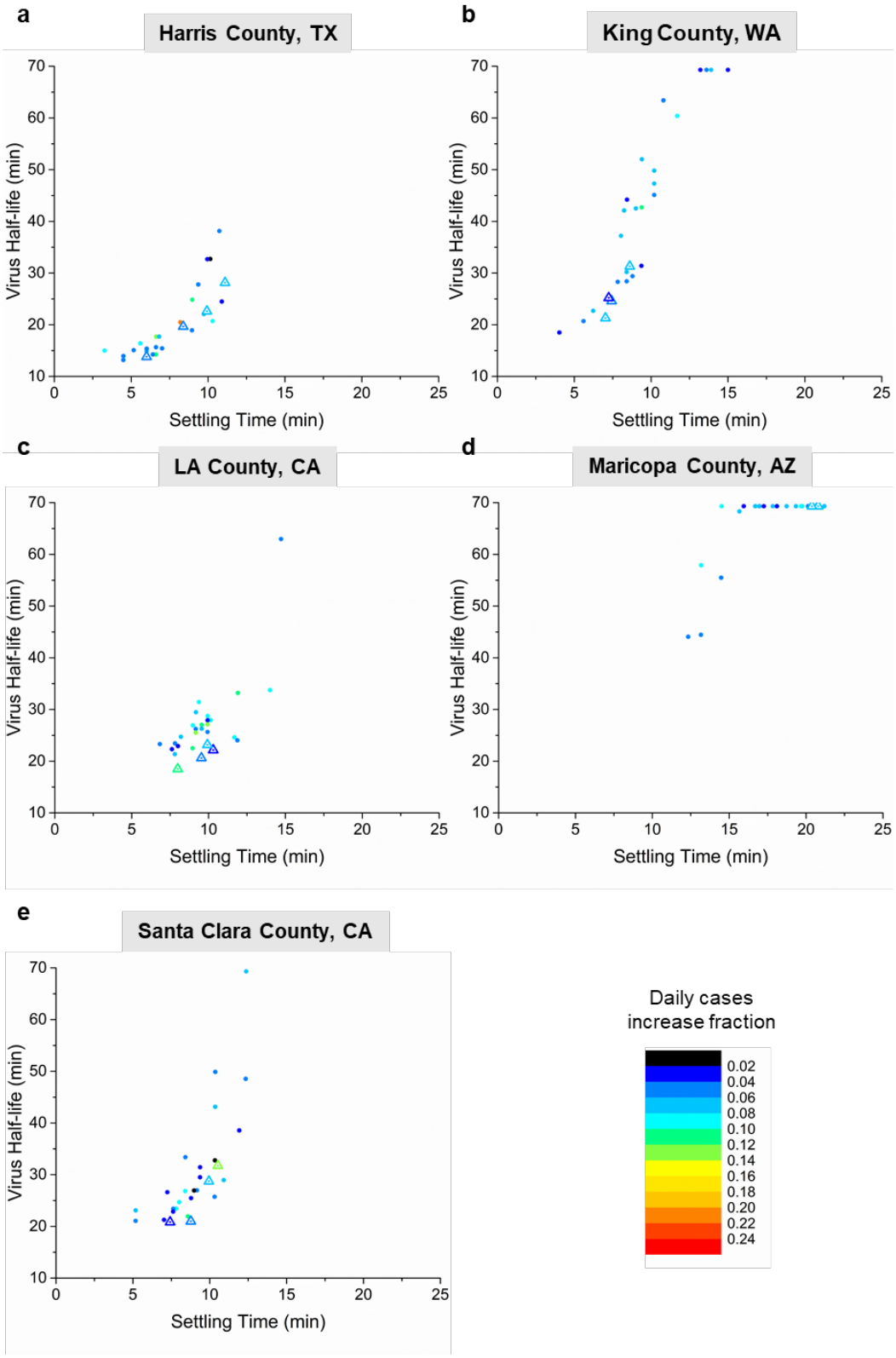
a
Harris County, TX
b
King County, WA
c
LA County, CA
d
Maricopa County, AZ
e
Santa Clara County, CA
Virus Half-life (min)
Settling Time (min)
Daily cases increase fraction
0.02
0.04
0.06
0.08
0.10
0.12
0.14
0.16
0.18
0.20
0.22
0.24

Figure 28. Data points available to generate the contour plot in Fig. 5 for each county, with the daily case percentage increase as a function of settling time and viral viability (represented by half-life). Colour shows the daily case percentage increase in decimal. The daily cases percentage increase is shown as the colour of each data point. The dots represent data points for training, and the triangles represent data for prediction. LR: linear regression; VAR: vector autoregression; Simple RNN: simple recurrent neural network; LSTM: long short-term memory recurrent neural network.

2.8 Tables

a. R^2 for Fitting

	LR	VAR	Simple RNN	LSTM
Harris County, TX	0.362	0.616	0.374	0.99998
King County, WA	0.540	0.702	0.979	0.99998
LA County, CA	0.805	0.882	0.772	0.99997
Maricopa County, AZ	0.530	0.873	0.712	0.99995
Santa Clara County, CA	0.719	0.721	0.745	0.99998

b. Sum of Squares of Residuals for Prediction

	LR	VAR	Simple RNN	LSTM
Harris County, TX	2.02E-03	3.87E-02	9.54E-04	4.37E-03
King County, WA	1.76E-03	3.85E-03	9.97E-04	1.30E-03
LA County, CA	2.32E-02	8.79E-03	1.20E-02	2.47E-03
Maricopa County, AZ	1.27E-03	1.56E-02	6.60E-04	4.19E-04
Santa Clara County, CA	1.02E-02	1.87E-02	9.29E-03	8.47E-03

c. Fitting and prediction for Maricopa County, May-August

	LR	Simple RNN	LSTM
R^2 for Fitting	0.172	0.579	0.99996
Sum of Squares of Residuals for Prediction	1.10E-02	1.56E-02	1.60E-02

Table 3. (a) R-squared of model fitting and (b) sum of squares of residuals of model prediction for each county and model during April 2020. (c) R-squared of model fitting and sum of squares of residuals of model prediction for Maricopa County during extended time frame from May to August 2020. LR: linear regression; VAR: vector autoregression; Simple RNN: simple recurrent neural network; LSTM: long short term memory recurrent neural network.

2.9 Acknowledgements

This work was supported by the Bill & Melinda Gates Foundation Investment Grant INV-018569. The authors thank Paul Dabisch at National Biodefense Analysis and Countermeasures Center for sharing his insights on SARS-CoV-2 viability. The authors would like to acknowledge Richard Flagan for helpful discussions.

Chapter 4

IMAGE RECOGNITION FOR A SARS-COV-2 TEST KIT

Zhu, Y., Wu, X., Gu, A., Dobelle, L., Cid, C. A., Li, J., & Hoffmann, M. R. (2021). Membrane-Based In-Gel Loop-Mediated Isothermal Amplification (mgLAMP) System for SARS-CoV-2 Quantification in Environmental Waters. *Environmental Science & Technology*. doi:10.1021/acs.est.1c04623.

3.1 Abstract

Since the COVID-19 pandemic is expected to become endemic, quantification of severe acute respiratory syndrome coronavirus-2 (SARS-CoV-2) in environmental waters is critical for rapid risk assessment and for early detection of outbreaks. Herein, we report on the development of a membrane-based in-gel loop-mediated isothermal amplification (mgLAMP) system that is designed for the rapid point-of-use quantification of SARS-CoV-2 particles in environmental waters. The mgLAMP system integrates viral concentration, in-assay viral lysis, and an on-membrane hydrogel-based RT-LAMP quantification using an enhanced fluorescence detection with a target-specific probe. With a sample-to-result time of less than 1 hour, mgLAMP has a limit of detection (LOD) of 0.96 copies/mL in Milli-Q water and 93 copies/mL in surface water. The LOD of mgLAMP for SARS-CoV-2 detection in surface water was at least 10-fold lower than that of the reverse transcription quantitative polymerase chain reaction (RT-qPCR). A 3D-printed portable device is designed to integrate heated incubation and fluorescence illumination for the simultaneous analysis of 9 mgLAMP

assays. Smartphone-based imaging and machine learning-based image processing are used for interpretation of results. In this report, we demonstrate that mgLAMP is a promising method for large-scale environmental surveillance of SARS-CoV-2 without the need for specialized equipment, highly-trained personnel, and labor-intensive procedures.

3.2 Introduction

The pandemic of coronavirus disease 2019 (COVID-19) is predicted to become endemic with seasonal fluctuations.[123-124] The SARS-CoV-2 virions and their RNA are known be shed in feces of infected individuals at a concentration of 10^2 to 10^8 copies/g.[125-127] Depending on sanitary practices the viral RNA is discharged in wastewater and surface waters.[128] Detection of SARS-CoV-2 RNA in river water and wastewater has been widely reported globally such as in Italy,[129] Japan,[130] and Brazil[131]. In Spain, SARS-CoV-2 RNA was detected in wastewater before the first local case was confirmed.[132] Virions may persist in environmental waters given that the time required for 99% viable virus load reduction (T_{99}) of 19.5 days for wastewater and T_{99} at 18.7 days for river water at 4 °C.[133] Thus large-scale environmental surveillance is necessary for quantitative risk assessment, for notice of potential outbreaks, population-wide infection prevalence monitoring, and for a better understanding of SARS-CoV-2 contamination and potential spread via environmental waters.[129, 134-135] Therefore, development of point-of-sampling testing technologies for large-scale environmental surveillance is needed to avoid the use of specialized equipment, highly-trained personnel, and labor-intensive laboratory procedures.[136]

Detection of SARS-CoV-2 is based on nucleic acid analysis (NAA) using primarily reverse transcription quantitative polymerase chain reaction (RT-qPCR).[130, 132, 137-140] RT-qPCR is not readily adaptable for large-scale environmental surveillance especially in resource-limited settings due to its requirement for a specialized thermocycling instrument and the need for highly-trained personnel. Furthermore, RT-qPCR does not produce absolute quantification. In addition, RT-qPCR targeting SARS-CoV-2 is sensitive to inhibitors that are present in wastewater leading to false negative results.[141-142] To address these challenges, isothermal NAA methods, such as loop-mediated isothermal amplification (LAMP), are used for environmental quantification of other microbial pathogens including Zika virus,[143]

astrovirus,[144] MS2,[145] *E. coli,* and *Enterococcus spp,*[146-147]. RT-LAMP quantification has higher tolerances to inhibitors and shorter the amplification times (e.g., 30 min) compared to RT-qPCR. Huang et al. used a portable in-gel LAMP platform for the sensitive detection of MS2 coliphage in wastewater while RT-qPCR failed to produce a positive result.[145] RT-LAMP has been used in portable SARS-CoV-2 detection platforms for use on clinical samples.[148-149] However, isothermal methods have yet to be developed for detecting SARS-CoV-2 in environmental water samples.

Point-of-use (POU) NAA for environmental surveillance normally requires the implementation of complex procedures required for sample preparation, including viral particle concentration, RNA extraction, and subsequent purification.[140] SARS-CoV-2 loads observed in surface water and wastewater are typically lower than the detection limit of RT-qPCR.[128, 130, 132] Therefore, SARS-CoV-2 viral particles are commonly concentrated from 50-500 mL water sample for example by ultracentrifugation,[150] ultrafiltration,[137] polyethylene glycol (PEG) precipitation,[151] or electronegative membrane filtration[130, 137]. The recovery rates using these methods for SARS-CoV-2 concentration of samples taken from wastewater and surface waters are poorly understood, while the recovery rates for similar-structured surrogates are generally in the range of 26.7-65.7%.[137] Other existing in-field virus concentration technologies, such as nanofiltration via superabsorbent polymer microspheres[152-153] and bag-mediated filtration[154], may be readily adaptable for SARS-CoV-2. For RNA concentration and purification, specialized commercial kits for environmental samples are commonly employed but they involve a series of manual operations.[130, 137, 140, 150-151] These sample preparation steps take at least 2 hours and require specialized instruments. Integration of sample preparation is needed for the development of rapid, sensitive, and POU quantification platforms targeting SARS-CoV-2 in environmental waters.

Herein, we report on a membrane-based in-gel loop-mediated isothermal amplification (mgLAMP) system for absolute quantification of SARS-CoV-2 in environmental water samples within a 1-hr timeframe. The limit of detection (LOD) was 0.96 copy/mL in Milli-

Q water and 93 copies/mL in surface water. The mgLAMP assay and setup development is presented, and its performance was characterized in SARS-CoV-2 spiked Milli-Q water, river water samples, and wastewater samples. We further demonstrated the feasibility of POU applications by developing a portable device that integrates heat incubation, fluorescence illumination, and a cloud-based smartphone image analysis algorithm for quantitative results interpretation. We demonstrate that our integrated portable platform can be reliably used for the POU absolute quantification of SARS-CoV-2 in environmental water samples. Our mgLAMP, as an NAA-based platform, has been adapted for the detection of other microbial pathogens and can be modified easily for use in other sample matrices (e.g., clinical samples).

3.3 Image Analysis Methods

For automated signal counting, a machine-learning model was developed using AutoML Vision module of the Google Cloud Platform (Google, Mountain View, CA). To establish the model, 10 fluorescence microscope images were uploaded to Google Cloud Storage and all signals in those images were labelled manually. Each image with more than 50 signals was split into a 3×3 grid (total of 9 smaller images), and each of the smaller images was uploaded and labelled separately to meet the Google Cloud Vision's limit of 50 signals per image. All images uploaded were categorized randomly as training, testing and validation images with an 8:1:1 ratio. Training of the machine learning model used the high accuracy goal setting and 27 node hours. The trained model was deployed with 1 node for online access. To assess the accuracy of our trained model, 16 new smartphone images were analyzed and compared with manual counts. A portable device was designed to integrate heating, fluorescence illumination, and fluorescence emission filtering. The prototype was assembled with electrical components purchased from Digikey (Thief River Falls, MN) and Programmed Scientific Instruments (Arcadia, California) and plastic structures fabricated by 3D printing (Makerbot METHOD X, Makerbot, Brooklyn, NY) using PLA and ABS filaments (Makerbot, Brooklyn, NY).

3.4 Image Analysis Results: Proof of Portability

To demonstrate the POU applicability of mgLAMP, we developed an image processing algorithm for mgLAMP pictures taken by a smartphone on the portable mgLAMP prototype. Quantitative mgLAMP results were generated by counting amplification dots. As an alternative to fluorescence microscopy, smartphone imaging of the fluorescence amplification dots was shown to be robust enough to deliver comparable image quality for dot counting.[145] Paired with smartphone imaging, our image processing algorithm can be used for point-of-sample-collection quantitative result determination. A machine learning model was trained for 27 node hours using AutoML Vision module of the Google Cloud Platform by feeding 10 fluorescence microscope mgLAMP images with labelled amplicon dots. Models trained with up to 96 mgLAMP images (94 fluorescence microscope images and 2 smartphone images) and 20-54 node hours training time yielded lower recognition accuracy, likely due to overtraining.[155-156] We then tested the trained model with 16 new mgLAMP images and compared the model-recognized signals with visual assessment. An example of this approach is shown in Figure 29a-b. In this image, 20 out of 24 signals were correctly recognized by AutoML vision with no false positive and 4 false negatives. For the 16 tested images, the results from the machine learning algorithm were close to those obtained by manual counting ($y = 0.9926x$, $R^2 = 0.992$) (Figure 29c). The deviations from manual counting were mostly false negatives due to the low fluorescence intensity of the dots or vague boundaries between the adjacent dots with occasional false positives. Furthermore, our portable prototype (Figure 29d) was assembled with 3D-printed parts and commercially-available electrical components. The prototype is able to run 9 mgLAMP reactions simultaneously through 30 min of RT-LAMP heating at 65 °C, fluorescence excitation with high-powered LEDs, and fluorescence emission filtering (Figure 29e). The estimated cost of the prototype is approximately $500. This compact, low cost mgLAMP system can run assays without access to biological laboratories or the need for bulky lab-based equipment.

3.5 Figures

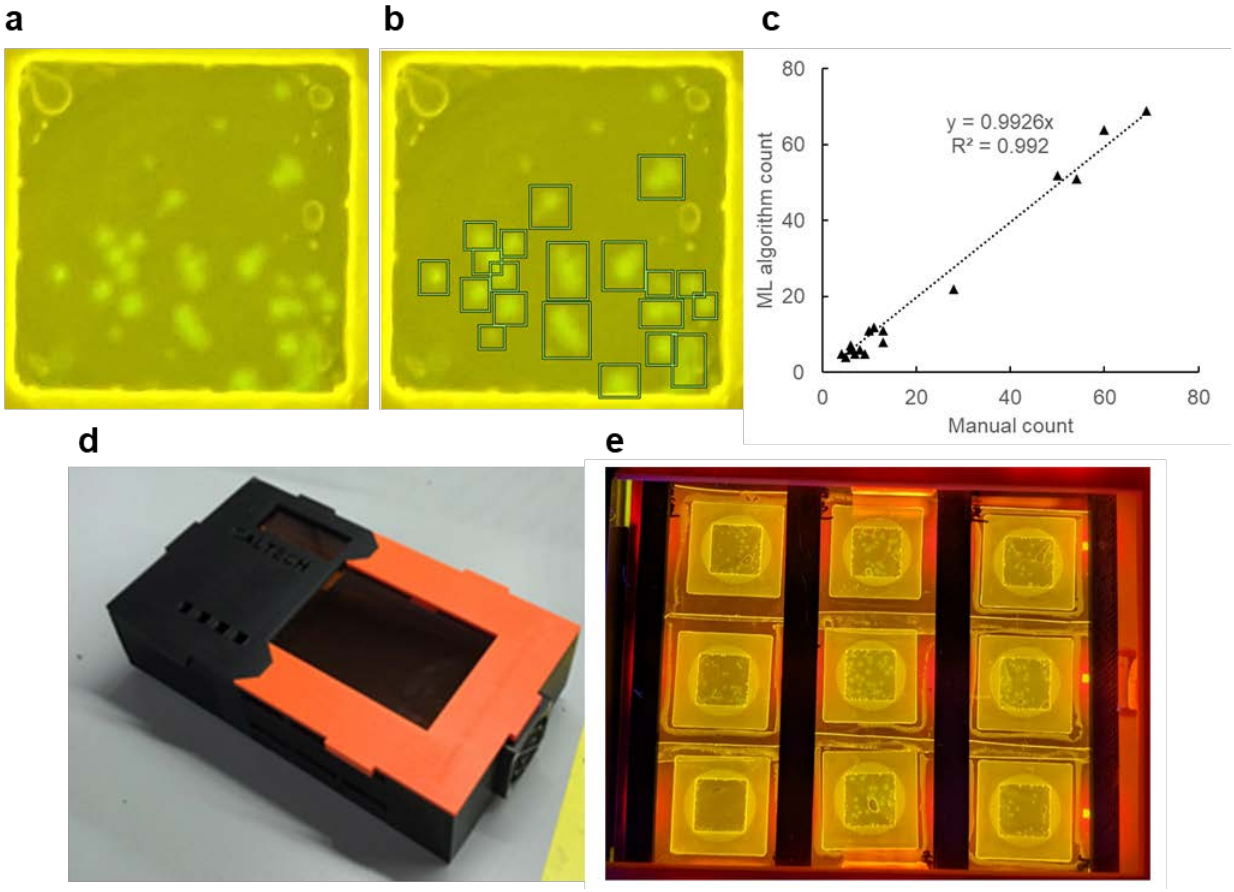

Figure 29. Cloud-based image processing and portable device prototyping. (a) An example mgLAMP image taken by a smartphone. (b) In the same image, the squares highlight the recognized amplicon dots by our trained Google AutoML Vision model. (c) The accuracy of the trained ML model in amplicon dot counting. Sixteen smartphone images were tested, and the results were compared to manual counting of the same images. The dotted line represents the linear fitting of the observed ML counts versus manual counts, with the equation and R-square displayed. (d) Picture of our portable mgLAMP device prototype. The prototype holds 9 mgLAMP reactions, provides 65 °C heating, laser excitation, and fluorescence emission filter. (e) Examples picture of the output from the prototype.

3.6 Acknowledgements

General: The authors thank Caltech Biological Imaging Facility for use of the confocal microscope and Dr. Yuxing Yao for assistance with DLS measurements. **Funding:** The authors acknowledge the financial support provided by the Bill and Melinda Gates Foundation (grant nos. OPP1192379, INV-018569, and INV-030223).

Chapter 5

CO_2-ACTIVATED H_2O_2 OXIDATION

4.1 Abstract

Peroxymonocarbonate (HCO_4^-) is a reactive oxygen species previously used in chemical manufacturing and water detoxification. However, its role in atmospheric chemistry remains largely unexplored despite its high reduction potential for oxygen-atom transfer reactions ($E(HCO_4^-/HCO_3^-)$ = 1.8V vs SHE) as well as the abundance of CO_2 and H_2O_2 in the atmosphere. This work explores the formation and role of HCO_4^- at the interface of an aqueous H_2O_2 jet and an intersection stream of CO_2 gas in an online electrospray ionization mass spectrometry (o-ESI-MS) reacting for ~50 μs. The interfacial kinetics of HCO_4^- formation is measured to be $>10^4$ times faster than the bulk phase kinetics, possibly due to the incomplete hydrogen bonding network at the gas-liquid interface. The oxidation of methanesulfinate by H_2O_2 is 200 times faster in the presence of CO_2 than in its absence. Peroxymonocarbonate may play an important yet previously unexplored role in the oxidation of atmospheric sulfides, (bi)sulfites and alkenes.

4.2 Introduction

Peroxymonocarbonate (HCO_4^-) is an oxidant formed in the presence of H_2O_2 and CO_2 via reaction R6[157-158]

$$H_2O_2 + CO_2 \longrightarrow H^+ + HCO_4^- \qquad [R6]$$

Given its high estimated standard reduction potential ($E(HCO_4^-/HCO_3^-)$ = 1.8V vs SHE)[159] for oxygen atom transfer reaction, CO_2 and HCO_3^- has been used as a green catalyst to activate H_2O_2 in alkene epoxidation[160-161] and sulfide oxidation[159, 162]. In those applications, a rate acceleration of 2 orders of magnitude is observed for most substrates upon introduction

of CO_2 or HCO_3^-. The role of peroxymonocarbonate is recognized as a possible approach for soil remediation in which aqueous H_2O_2 is injected in the sub-surface where it reacts with environmental HCO_3^- to form HCO_4^-. The formed HCO_4^- may have similar importance as hydroxyl radicals ($^{\cdot}OH$) in oxidizing environmental contaminants under certain geological conditions.[163] In the atmosphere, both H_2O_2 and CO_2 also exist: H_2O_2 concentrations are measured within the range of 0.1-1 ppbv in the gas phase, and 1-100 μM in aerosols;[164] CO_2 is measured to be 412 ppm in the gas phase,[165] and calculated to be 14 μM in the aqueous phase using Henry's Law.[166] Hence, peroxymonocarbonate is expected in the atmosphere, though its importance remains unexplored.

Considering the abundance of H_2O_2 in the liquid aerosol phase and CO_2 in the gas phase, gas-liquid interfacial chemistry may be significant in relation to the bulk aqueous or gas phase reactions. Previous studies (including the work presented in Chapter 2) found 3-4 orders of magnitude rate acceleration for interfacial reactions compared to the same reactions in the bulk liquid phase.[35, 167-168]

This work investigates the importance of peroxymonocarbonate in terms of its formation kinetics and oxidation of atmospherically relevant substrates, both at the air-water interface and in the bulk aqueous phase. The model substrate is chosen to be methanesulfinate ($MeSO_2^-$), which can accept an oxygen atom from either H_2O_2 or HCO_4^- to form methanesulfonate ($MeSO_3^-$) as shown in Figure 30. Methanesulfinate is an oxidation intermediate from biogenic dimethyl sulfide (Me_2S) emissions.[32] These emissions account for ~15% of the global atmospheric sulfur budget.[169] An accelerated oxidation kinetics by HCO_4^- compared to H_2O_2 may help explain higher than predicted oxidation products observed in the atmosphere.

4.3 Methods

The experimental apparatus is largely the same as described in Chapter II of the thesis, with different reagents and mass spectrometer voltage parameters. Positively and negatively charged reaction products were analyzed by electrospray ionization mass spectrometry (ESI-

MS). In the gas-liquid experiments, aqueous solutions of H_2O_2 are injected (30 µL min^{-1}) through a stainless-steel Agilent G1946-68703 nozzle) into the spray chamber of the ESI mass spectrometer (Agilent G2445A Ion Trap MSD) (maintained at 1 atm with ultrapure N_2(g), 293 ± 2 K) using a syringe pump (Cole-Parmer 74905-02 and 74905-50). A coaxial, codirectional, fast (~340m s^{-1}) stream of N_2(g) pneumatically nebulizes the outermost layers of the aqueous microjets into sub-micrometer-sized droplets (microdroplets) within 50 µs.[36] Microjets and microdroplets were made to react with an orthogonal stream of O_3(g) directed to the tip of the nozzle for ~ 1 ms, which is the estimated residence time of the microdroplets in the spray chamber, before they are pumped into the low pressure section of the mass spectrometer.[37-38] Microdroplets are naturally charged during nebulization by the segregation of anions from cations and deflected by an applied electric field towards the inlet to the low-pressure section of the mass spectrometer. Microdroplets evaporate within a heated capillary tubing prior to undergoing Coulombic explosions that release the ions contained in the microdroplets to the gas-phase for detection. A schematic of this experimental setup is shown in Figure 31.

Experiments carried out in bulk-phase water were performed by injecting H_2O_2 and $NaHCO_3$ aqueous solutions through separate ports into a manifold mixer (Cole-Parmer Manifold Mixing Valve EW-01356-21, Figure 32) modelled as a tank reactor. The reactions were then allowed to take place for 12 minutes before injection into the ESI mass spectrometer for analysis.

In both interfacial and bulk-phase experimental setups, instrumental drift was eliminated by adding non-complexing Cs^+ and ClO_4^- (50µM $CsClO_4$) ions as internal standards. Positive and negative ions were quantified in the same experiments by alternating positive/negative either in mass scanning or SIM (selected ion monitoring) detecting modes.

The ESI mass spectrometer was operated as follows. Positive ions were detected by polarizing the capillary at -3.434 kV (voltages relative to ground), the end plate offset and the capillary exit at 500 V and 60.7 V, respectively. In the negative mode, the capillary voltage was at 3.434 kV, and the end plate offset and the capillary exit at 500 and -60.7 V,

respectively. The nebulizer N_2 gas source was maintained at 40 psi, and the drying gas (at 325 °C) flow rate was 10 L min^{-1}.

99.99 % CO_2(g) is supplied by Airgas and is introduced into the spray chamber of the ESI-MS at 50 cm^3 min^{-1} via a calibrated rotameter. The pH of aqueous solutions was adjusted before injection by adding $HClO_4$/NaOH solutions and measured (within ± 0.5 pH units) with pH paper (Milipore MCholorpHast). Sodium methanesulfinate ($MeSO_2Na$), sodium methanesulfonate ($MeSO_3Na$), sodium bicarbonate ($NaHCO_3$), cesium perchlorate ($CsClO_4$), perchloric acid ($HClO_4$) and sodium hydroxide (NaOH) of purity 95% or higher were obtained from Sigma Aldrich and used as received. 30% H_2O_2 is obtained from Sigma Aldrich and used as received.

4.4 Results and Discussion

Figure 33 shows the formation kinetics of peroxymonocarbonate at moderately acidic and basic pH, in the bulk aqueous phase as well as at the air-water interface. In the bulk phase, a higher HCO_4^- product concentration is measured at pH = 8.5 compared to pH = 4.5, corroborating previous measurement of H_2CO_4 pKa ~ 4.[159] The higher speciation fraction of HCO_3^- (pK_a = 6.3 for $H_2O{\cdot}CO_2/H_2CO_3$ [159]) at pH = 8.5 may have also enhanced the formation of HCO_4^- from HCO_3^- and H_2O_2.[158] At the air-water interface, however, both pH show similar HCO_4^- formation kinetics. This may be explained by previous observations of the superacidic weakly-hydrated hydronium ions at the air-water interface.[167, 170] Despite having different bulk aqueous phase pH of 4.5 and 8.5, the superacidic hydronium ions at the interface protonates HCO_3^- and/or HCO_4^- to near completion in both scenarios, resulting in similar measured kinetics. In both scenarios, the interfacial reaction kinetics are measured to be 3-4 orders of magnitude faster compared the bulk liquid phase kinetics, similar to previous observations in other reaction systems.[35, 167-168]

The importance of peroxymonocarbonate in the atmosphere is showcased in Figure 34, where methanesulfinate is oxidized by H_2O_2 or peroxymonocarbonate. At pH = 4.5, no difference is measured in the oxidation rate of methanesulfinate upon introduction of gaseous

CO_2 into the reaction system while aqueous H_2O_2 reacts with aqueous methane sulfinate. This choice of reactant phases simulates the atmospheric conditions. At pH = 8.5, the presence of aqueous HCO_3^- accelerates the H_2O_2 oxidation of methanesulfinate by 2 orders of magnitude in the aqueous phase (orange vs purple bar), which agrees with previous findings when oxidizing other sulfides with peroxymonocarbonate.[159, 162] The presence of gaseous CO_2 further accelerates the reaction by 4 orders of magnitude at the interface (purple vs green bar), agreeing with the interfacial rate acceleration observed for peroxymonocarbonate formation at pH = 8.5 in Figure 33. This indicate that peroxymonocarbonate is the reaction intermediate responsible for the observed rate acceleration. The interfacial rate acceleration may be attributed to the incomplete hydration sphere of methane sulfinate, where the unhydrated, exposed sulfur center may accept an oxygen atom transfer with less energy penalty than a hydrated sulfur center.

4.5 Conclusions

Laboratory experiments indicate that gaseous and dissolved CO_2 accelerate H_2O_2 oxidation of methanesulfinate, an atmospherically relevant substrate, by 2 orders of magnitude. The rate acceleration may be attributed to the formation of peroxymonocarbonate as the oxidation reaction intermediate. Formation of the peroxymonocarbonate intermediate and subsequent oxidation of the methanesulfinate substrate are accelerated by 3-4 orders of magnitude at the air-water interface compared to in the bulk aqueous phase. This chemistry may have been playing an important yet previously unrecognized role in atmospheric chemistry. The next step of this work may investigate other atmospherically relevant substrates that may accept an oxygen atom from peroxymonocarbonate such as dimethyl sulfoxide and dimethyl sulfide, as well as substrates whose oxidation may be initiated by accepting an oxygen atom, such as methyl vinyl ketone and methacrolein.

4.6 Figures

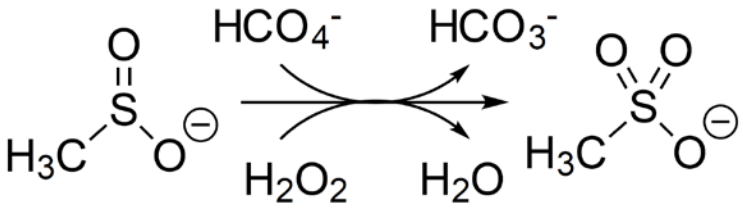

Figure 30. Oxidation of methanesulfinate $MeSO_2^-$ by H_2O_2 or HCO_4^- to methanesulfonate $MeSO_3^-$. The oxidation byproducts are HCO_3^- (from HCO_4^-) and H_2O (from H_2O_2).

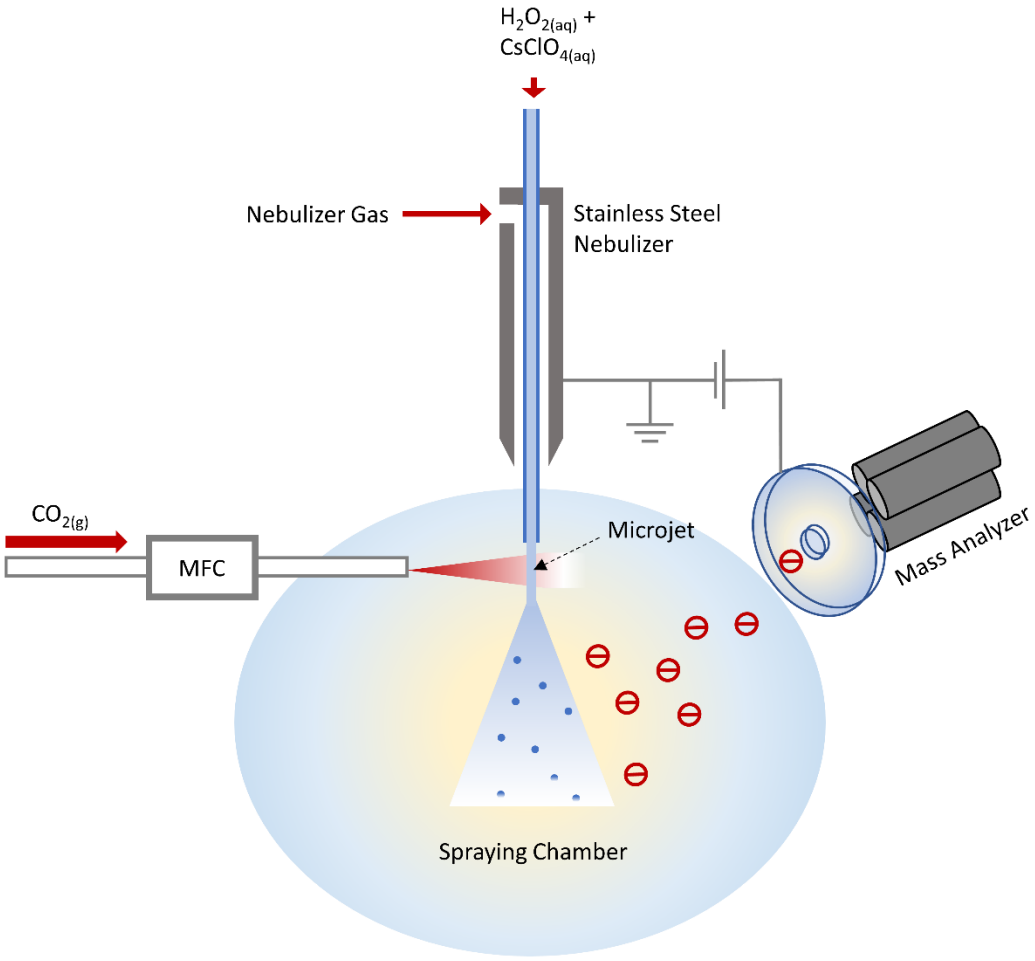

Figure 31. Experimental setup of the online ESI-MS. The aqueous reactants and gaseous reactants contact at the outlet tip of the microjet.

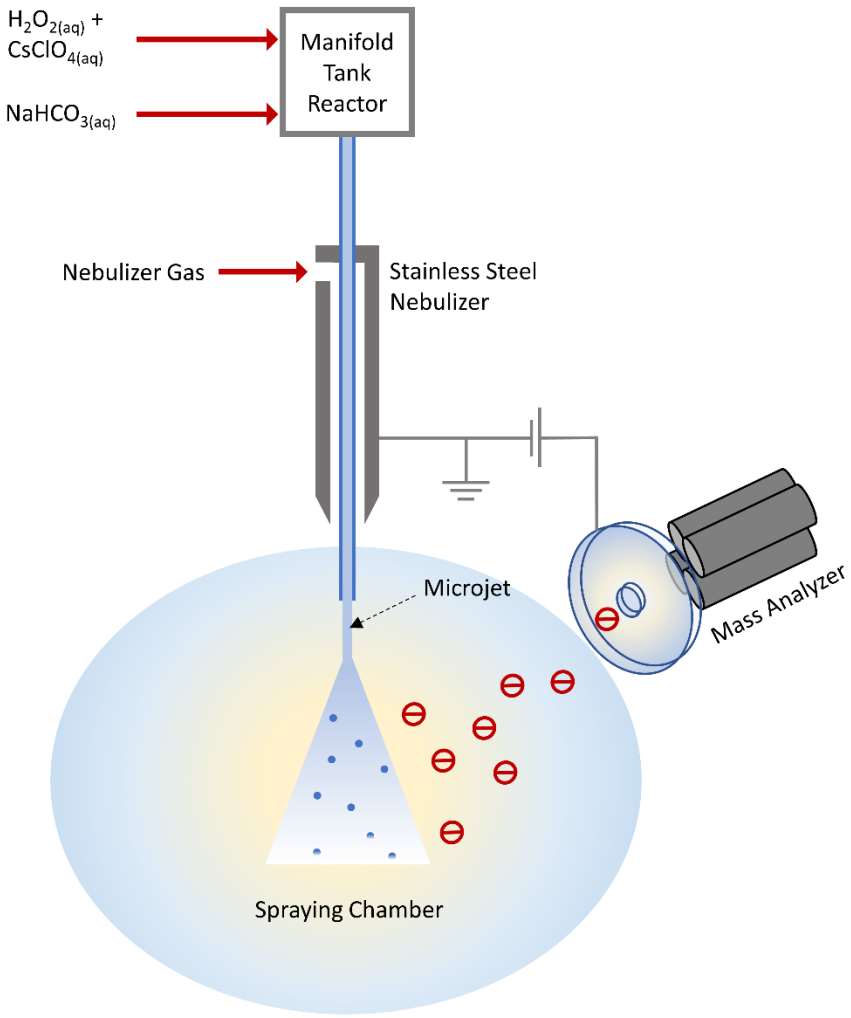

Figure 32. Experimental setup of the offline ESI-MS. The aqueous reactants contact each other in the manifold tank reactor before entering the microjet.

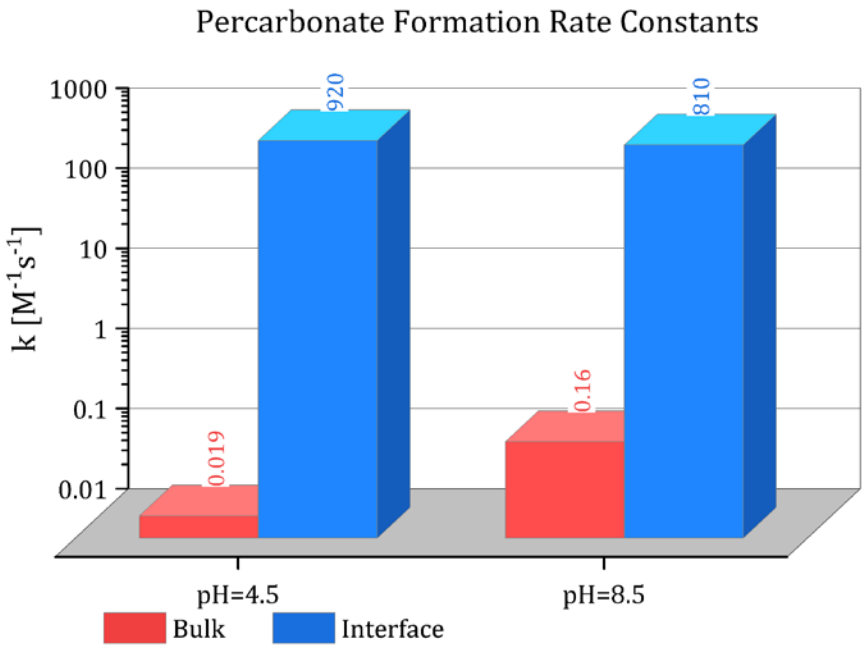

Figure 33. Percarbonate a.k.a. peroxymonocarbonate (HCO_4^-) formation kinetics (y-axis) measured at different pH, in the bulk aqueous phase and at the air-water interface. Rate constant is obtained assuming first order dependence on the concentration of H_2O_2, and CO_2 or HCO_3^-. The 'Bulk' reaction forms peroxymonocarbonate from aqueous H_2O_2 and aqueous HCO_3^-; the 'Interface' reaction forms peroxymonocarbonate from aqueous H_2O_2 and gaseous CO_2.

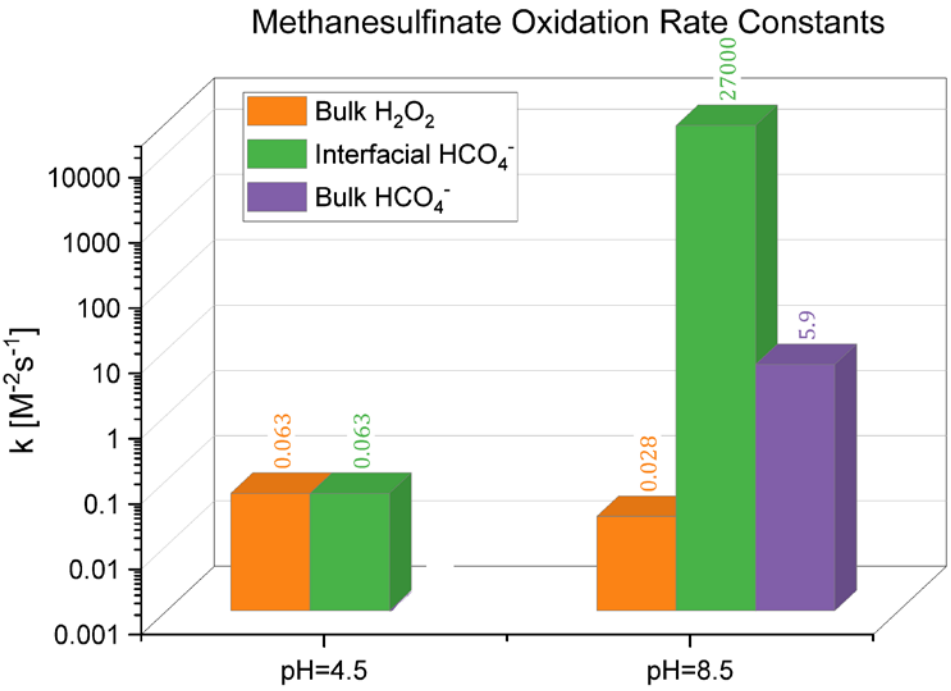

Figure 34. Kinetics of methanesulfinate ($MeSO_2^-$) oxidation by H_2O_2 (orange bars) or HCO_4^- (green and purple bars) at different pH, in the bulk aqueous phase (orange and purple bars) or air-water interface (green bars). The rate constant is plotted on the y-axis. The rate constants are obtained assuming first order dependence on $MeSO_2^-$, H_2O_2, and CO_2 or HCO_3^-. The 'Bulk H_2O_2' reactions involve oxidizing aqueous $MeSO_2^-$ with aqueous H_2O_2 in a nitrogen atmosphere; the 'Interfacial HCO_4^-' reaction involve oxidizing aqueous $MeSO_2^-$ with aqueous H_2O_2 in the presence of gaseous CO_2; the 'Bulk HCO_4^-' reaction involve oxidizing aqueous $MeSO_2^-$ with aqueous H_2O_2 in the presence of aqueous HCO_3^-.

4.7 Acknowledgements

This work is supported by the Resnick Sustainability Institute. Special thanks to Prof. Xuejing Yang for inspiration and helpful discussions.

BIBLIOGRAPHY

1. Hoffmann, P.; Dedik, A. N.; Ensling, J.; Weinbruch, S.; Weber, S.; Sinner, T.; Gütlich, P.; Ortner, H. M., Speciation of iron in atmospheric aerosol samples. *Journal of Aerosol Science* **1996,** *27* (2), 325-337.
2. Deguillaume, L.; Leriche, M.; Desboeufs, K.; Mailhot, G.; George, C.; Chaumerliac, N., Transition Metals in Atmospheric Liquid Phases: Sources, Reactivity, and Sensitive Parameters. *Chemical Reviews* **2005,** *105* (9), 3388-3431.
3. Kuang, X. M.; Gonzalez, D. H.; Scott, J. A.; Vu, K.; Hasson, A.; Charbouillot, T.; Hawkins, L.; Paulson, S. E., Cloud Water Chemistry Associated with Urban Aerosols: Rapid Hydroxyl Radical Formation, Soluble Metals, Fe(II), Fe(III), and Quinones. *ACS Earth Space Chem.* **2019**.
4. Paulson, S. E.; Gallimore, P. J.; Kuang, X. M.; Chen, J. R.; Kalberer, M.; Gonzalez, D. H., A light-driven burst of hydroxyl radicals dominates oxidation chemistry in newly activated cloud droplets. *Science Advances* **2019,** *5* (5), eaav7689.
5. Ding, J.; Guan, Y.; Cong, Y.; Chen, L.; Li, Y.-F.; Zhang, L.; Zhang, L.; Wang, J.; Bai, R.; Zhao, Y.; Chen, C.; Wang, L., Single-Particle Analysis for Structure and Iron Chemistry of Atmospheric Particulate Matter. *Analytical Chemistry* **2020,** *92* (1), 975-982.
6. Zhang, G.; Lin, Q.; Peng, L.; Yang, Y.; Jiang, F.; Liu, F.; Song, W.; Chen, D.; Cai, Z.; Bi, X.; Miller, M.; Tang, M.; Huang, W.; Wang, X.; Peng, P. a.; Sheng, G., Oxalate Formation Enhanced by Fe-Containing Particles and Environmental Implications. *Environmental Science & Technology* **2019,** *53* (3), 1269-1277.
7. Chevallier, E.; Jolibois, R. D.; Meunier, N.; Carlier, P.; Monod, A., "Fenton-like" reactions of methylhydroperoxide and ethylhydroperoxide with Fe2+ in liquid aerosols under tropospheric conditions. *Atmospheric Environment* **2004,** *38* (6), 921-933.
8. Chen, R.; Pignatello, J. J., Role of Quinone Intermediates as Electron Shuttles in Fenton and Photoassisted Fenton Oxidations of Aromatic Compounds. *Environmental Science & Technology* **1997,** *31* (8), 2399-2406.
9. Gonzalez, D. H.; Cala, C. K.; Peng, Q.; Paulson, S. E., HULIS Enhancement of Hydroxyl Radical Formation from Fe(II): Kinetics of Fulvic Acid–Fe(II) Complexes in the Presence of Lung Antioxidants. *Environmental Science & Technology* **2017,** *51* (13), 7676-7685.
10. Mao, J.; Fan, S.; Horowitz, L. W., Soluble Fe in Aerosols Sustained by Gaseous HO2 Uptake. *Environmental Science & Technology Letters* **2017,** *4* (3), 98-104.

11. Daumit, K. E.; Carrasquillo, A. J.; Sugrue, R. A.; Kroll, J. H., Effects of Condensed-Phase Oxidants on Secondary Organic Aerosol Formation. *The Journal of Physical Chemistry A* **2016,** *120* (9), 1386-1394.
12. Al-Abadleh, H. A., Review of the bulk and surface chemistry of iron in atmospherically relevant systems containing humic-like substances. *RSC Advances* **2015,** *5* (57), 45785-45811.
13. Lim, Y. B.; Turpin, B. J., Laboratory evidence of organic peroxide and peroxyhemiacetal formation in the aqueous phase and implications for aqueous OH. *Atmos. Chem. Phys.* **2015,** *15* (22), 12867-12877.
14. Pestovsky, O.; Bakac, A., Identification and Characterization of Aqueous Ferryl(IV) Ion. In *Ferrates*, American Chemical Society: 2008; Vol. 985, pp 167-176.
15. Bakac, A., Oxygen Activation with Transition-Metal Complexes in Aqueous Solution. *Inorganic Chemistry* **2010,** *49* (8), 3584-3593.
16. Bataineh, H.; Pestovsky, O.; Bakac, A., pH-induced mechanistic changeover from hydroxyl radicals to iron(iv) in the Fenton reaction. *Chemical Science* **2012,** *3* (5), 1594-1599.
17. Pestovsky, O.; Bakac, A., Aqueous Ferryl(IV) Ion: Kinetics of Oxygen Atom Transfer To Substrates and Oxo Exchange with Solvent Water. *Inorganic Chemistry* **2006,** *45* (2), 814-820.
18. Barton, D. H. R.; Hu, B.; Taylor, D. K.; Rojas Wahl, R. U., The importance of carboxylate ligands in the differentiation of catalase reactivity from Gif ketonization systems. *Tetrahedron Letters* **1996,** *37* (8), 1133-1136.
19. Barton, D. H. R.; Hu, B.; Taylor, D. K.; Wahl, R. U. R., The selective functionalization of saturated hydrocarbons. Part 32. Distinction between the Fe–Fe and Fe–Fe manifolds in Gif chemistry. The importance of carboxylic acids for alkane activation. Evidence for a dimeric iron species involved in Gif-type chemistry. *Journal of the Chemical Society, Perkin Transactions 2* **1996,** (6), 1031-1041.
20. Stavropoulos, P.; Çelenligil-Çetin, R.; Tapper, A. E., The Gif Paradox. *Accounts of Chemical Research* **2001,** *34* (9), 745-752.
21. Dorfman, L. M.; Adams, G. E., Reactivity of the hydroxyl radical in aqueous solutions. **1973**.
22. Rush, J. D.; Maskos, Z.; Koppenol, W. H., [12] Distinction between hydroxyl radical and ferryl species. In *Methods in Enzymology*, Academic Press: 1990; Vol. 186, pp 148-156.
23. Deguillaume, L.; Leriche, M.; Chaumerliac, N., Impact of radical versus non-radical pathway in the Fenton chemistry on the iron redox cycle in clouds. *Chemosphere* **2005,** *60* (5), 718-724.
24. Cantú Reinhard, F. G.; Faponle, A. S.; de Visser, S. P., Substrate Sulfoxidation by an Iron(IV)-Oxo Complex: Benchmarking Computationally Calculated

Barrier Heights to Experiment. *The Journal of Physical Chemistry A* **2016,** *120* (49), 9805-9814.

25. Zhou, Z.; Dai, G.; Ru, S.; Yu, H.; Wei, Y., Highly selective and efficient olefin epoxidation with pure inorganic-ligand supported iron catalysts. *Dalton Transactions* **2019,** *48* (37), 14201-14205.
26. Kameel, F. R.; Riboni, F.; Hoffmann, M. R.; Enami, S.; Colussi, A. J., Fenton Oxidation of Gaseous Isoprene on Aqueous Surfaces. *Journal of Physical Chemistry C* **2014,** *118* (50), 29151-29158.
27. Huang, X. Y.; Groves, J. T., Beyond ferryl-mediated hydroxylation: 40 years of the rebound mechanism and C-H activation. *Journal of Biological Inorganic Chemistry* **2017,** *22* (2-3), 185-207.
28. Keenan, C. R.; Sedlak, D. L., Factors Affecting the Yield of Oxidants from the Reaction of Nanoparticulate Zero-Valent Iron and Oxygen. *Environmental Science & Technology* **2008,** *42* (4), 1262-1267.
29. Bataineh, H.; Pestovsky, O.; Bakac, A., Iron(II) Catalysis in Oxidation of Hydrocarbons with Ozone in Acetonitrile. *ACS Catalysis* **2015,** *5* (3), 1629-1637.
30. Widger, L. R.; Davies, C. G.; Yang, T.; Siegler, M. A.; Troeppner, O.; Jameson, G. N.; Ivanovic-Burmazovic, I.; Goldberg, D. P., Dramatically accelerated selective oxygen-atom transfer by a nonheme iron(IV)-oxo complex: tuning of the first and second coordination spheres. *J Am Chem Soc* **2014,** *136* (7), 2699-702.
31. Baptista, L.; Clemente da Silva, E.; Arbilla, G., Oxidation mechanism of dimethyl sulfoxide (DMSO) by OH radical in liquid phase. *Physical Chemistry Chemical Physics* **2008,** *10* (45), 6867-6879.
32. Watts, S. F.; Brimblecombe, P.; Watson, A. J., Methanesulphonic acid, dimethyl sulphoxide and dimethyl sulphone in aerosols. *Atmospheric Environment. Part A. General Topics* **1990,** *24* (2), 353-359.
33. Walling, C., Fenton's reagent revisited. *Accounts of Chemical Research* **1975,** *8* (4), 125-131.
34. Loegager, T.; Holcman, J.; Sehested, K.; Pedersen, T., Oxidation of ferrous ions by ozone in acidic solutions. *Inorganic Chemistry* **1992,** *31* (17), 3523-3529.
35. Enami, S.; Sakamoto, Y.; Colussi, A. J., Fenton chemistry at aqueous interfaces. *Proc Natl Acad Sci U S A* **2014,** *111* (2), 623-8.
36. Enami, S.; Colussi, A. J., Long-range specific ion-ion interactions in hydrogen-bonded liquid films. *Journal of Chemical Physics* **2013,** *138* (18).
37. Colussi, A.; Enami, S., Detecting Intermediates and Products of Fast Heterogeneous Reactions on Liquid Surfaces via Online Mass Spectrometry. *Atmosphere* **2019,** *10* (2).

38. Enami, S.; Mishra, H.; Hoffmann, M. R.; Colussi, A. J., Hofmeister effects in micromolar electrolyte solutions. *Journal of Chemical Physics* **2012,** *136* (15).
39. Becke, A. D., Density ‐ functional thermochemistry. III. The role of exact exchange. *The Journal of Chemical Physics* **1993,** *98* (7), 5648-5652.
40. Grimme, S.; Ehrlich, S.; Goerigk, L., Effect of the damping function in dispersion corrected density functional theory. *Journal of Computational Chemistry* **2011,** *32* (7), 1456-1465.
41. Schäfer, A.; Horn, H.; Ahlrichs, R., Fully optimized contracted Gaussian basis sets for atoms Li to Kr. *The Journal of Chemical Physics* **1992,** *97* (4), 2571-2577.
42. Schäfer, A.; Huber, C.; Ahlrichs, R., Fully optimized contracted Gaussian basis sets of triple zeta valence quality for atoms Li to Kr. *The Journal of Chemical Physics* **1994,** *100* (8), 5829-5835.
43. Enami, S.; Sakamoto, Y.; Hara, K.; Osada, K.; Hoffmann, M. R.; Colussi, A. J., "Sizing" Heterogeneous Chemistry in the Conversion of Gaseous Dimethyl Sulfide to Atmospheric Particles. *Environmental Science & Technology* **2016,** *50* (4), 1834-1843.
44. Chou, M.-S.; Chang, K.-L., Oxidation of Aqueous Dimethyl Sulfoxide (DMSO) Using UV, O3, and UV/O3. *Ozone: Science & Engineering* **2007,** *29* (5), 391-397.
45. Cheng, J.; Vecitis, C. D.; Hoffmann, M. R.; Colussi, A. J., Experimental anion affinities for the air/water interface. *J Phys Chem B* **2006,** *110* (51), 25598-602.
46. Bardouki, H.; da Rosa, M. B.; Mihalopoulos, N.; Palm, W. U.; Zetzsch, C., Kinetics and mechanism of the oxidation of dimethylsulfoxide (DMSO) and methanesulfinate (MSI−) by OH radicals in aqueous medium. *Atmospheric Environment* **2002,** *36* (29), 4627-4634.
47. Jacobsen, F.; Holcman, J.; Sehested, K., Activation parameters of ferryl ion reactions in aqueous acid solutions. *International Journal of Chemical Kinetics* **1997,** *29* (1), 17-24.
48. Mukherjee, G.; Lee, C. W. Z.; Nag, S. S.; Alili, A.; Cantu Reinhard, F. G.; Kumar, D.; Sastri, C. V.; de Visser, S. P., Dramatic rate-enhancement of oxygen atom transfer by an iron(iv)-oxo species by equatorial ligand field perturbations. *Dalton Trans* **2018,** *47* (42), 14945-14957.
49. Pye, H. O. T.; Nenes, A.; Alexander, B.; Ault, A. P.; Barth, M. C.; Clegg, S. L.; Collett Jr, J. L.; Fahey, K. M.; Hennigan, C. J.; Herrmann, H.; Kanakidou, M.; Kelly, J. T.; Ku, I. T.; McNeill, V. F.; Riemer, N.; Schaefer, T.; Shi, G.; Tilgner, A.; Walker, J. T.; Wang, T.; Weber, R.; Xing, J.; Zaveri, R. A.; Zuend, A., The acidity of atmospheric particles and clouds. *Atmos. Chem. Phys.* **2020,** *20* (8), 4809-4888.
50. Enami, S.; Ishizuka, S.; Colussi, A. J., Chemical signatures of surface microheterogeneity on liquid mixtures. *The Journal of Chemical Physics* **2019,** *150* (2), 024702.

51. Enami, S.; Mishra, H.; Hoffmann, M. R.; Colussi, A. J., Hofmeister effects in micromolar electrolyte solutions. *J Chem Phys* **2012,** *136* (15), 154707.
52. Enami, S.; Hoffmann, M. R.; Colussi, A. J., How phenol and alpha-tocopherol react with ambient ozone at gas/liquid interfaces. *J Phys Chem A* **2009,** *113* (25), 7002-10.
53. Kebarle, P.; Verkerk, U. H., Electrospray: from ions in solution to ions in the gas phase, what we know now. *Mass Spectrom Rev* **2009,** *28* (6), 898-917.
54. Xiong, H.; Lee, J. K.; Zare, R. N.; Min, W., Strong Electric Field Observed at the Interface of Aqueous Microdroplets. *J Phys Chem Lett* **2020,** *11* (17), 7423-7428.
55. Enami, S.; Hoffmann, M. R.; Colussi, A. J., Proton Availability at the Air/Water Interface. *The Journal of Physical Chemistry Letters* **2010,** *1* (10), 1599-1604.
56. Levanov, A. V.; Isaikina, O. Y.; Lunin, V. V., Thermodynamic and Kinetic Parameters of the Solubility of Ozone in Water. *Russian Journal of Physical Chemistry A* **2019,** *93* (7), 1230-1234.
57. *COVID-19 weekly epidemiological update - 19 Oct 2021*; World Health Organization (WHO): 2021.
58. Qu, G.; Li, X.; Hu, L.; Jiang, G., An Imperative Need for Research on the Role of Environmental Factors in Transmission of Novel Coronavirus (COVID-19). *Environ Sci Technol* **2020,** *54* (7), 3730-3732.
59. Ianevski, A.; Zusinaite, E.; Shtaida, N.; Kallio-Kokko, H.; Valkonen, M.; Kantele, A.; Telling, K.; Lutsar, I.; Letjuka, P.; Metelitsa, N.; Oksenych, V.; Dumpis, U.; Vitkauskiene, A.; Stasaitis, K.; Ohrmalm, C.; Bondeson, K.; Bergqvist, A.; Cox, R. J.; Tenson, T.; Merits, A.; Kainov, D. E., Low Temperature and Low UV Indexes Correlated with Peaks of Influenza Virus Activity in Northern Europe during 2010(-)2018. *Viruses* **2019,** *11* (3).
60. Shaman, J.; Kohn, M., Absolute humidity modulates influenza survival, transmission, and seasonality. *Proc Natl Acad Sci U S A* **2009,** *106* (9), 3243-8.
61. Stadnytskyi, V.; Bax, C. E.; Bax, A.; Anfinrud, P., The airborne lifetime of small speech droplets and their potential importance in SARS-CoV-2 transmission. *Proc Natl Acad Sci U S A* **2020,** *117* (22), 11875-11877.
62. Dabisch, P.; Schuit, M.; Herzog, A.; Beck, K.; Wood, S.; Krause, M.; Miller, D.; Weaver, W.; Freeburger, D.; Hooper, I.; Green, B.; Williams, G.; Holland, B.; Bohannon, J.; Wahl, V.; Yolitz, J.; Hevey, M.; Ratnesar-Shumate, S., The Influence of Temperature, Humidity, and Simulated Sunlight on the Infectivity of SARS-CoV-2 in Aerosols. *Aerosol Science and Technology* **2020**, 1-15.
63. Schuit, M.; Ratnesar-Shumate, S.; Yolitz, J.; Williams, G.; Weaver, W.; Green, B.; Miller, D.; Krause, M.; Beck, K.; Wood, S.; Holland, B.; Bohannon, J.; Freeburger, D.; Hooper, I.; Biryukov, J.; Altamura, L. A.; Wahl, V.; Hevey,

M.; Dabisch, P., Airborne SARS-CoV-2 Is Rapidly Inactivated by Simulated Sunlight. *J Infect Dis* **2020,** *222* (4), 564-571.

64. Rodriguez-Palacios, A.; Cominelli, F.; Basson, A. R.; Pizarro, T. T.; Ilic, S., Textile Masks and Surface Covers-A Spray Simulation Method and a "Universal Droplet Reduction Model" Against Respiratory Pandemics. *Front Med (Lausanne)* **2020,** *7*, 260.
65. Anfinrud, P.; Stadnytskyi, V.; Bax, C. E.; Bax, A., Visualizing Speech-Generated Oral Fluid Droplets with Laser Light Scattering. *N Engl J Med* **2020,** *382* (21), 2061-2063.
66. Bazant, M. Z.; Bush, J. W. M., A guideline to limit indoor airborne transmission of COVID-19. *Proc Natl Acad Sci U S A* **2021,** *118* (17).
67. Prather, K. A.; Marr, L. C.; Schooley, R. T.; McDiarmid, M. A.; Wilson, M. E.; Milton, D. K., Airborne transmission of SARS-CoV-2. *Science* **2020,** *370* (6514), 303-304.
68. Kucharski, A. J.; Russell, T. W.; Diamond, C.; Liu, Y.; Edmunds, J.; Funk, S.; Eggo, R. M.; Sun, F.; Jit, M.; Munday, J. D.; Davies, N.; Gimma, A.; van Zandvoort, K.; Gibbs, H.; Hellewell, J.; Jarvis, C. I.; Clifford, S.; Quilty, B. J.; Bosse, N. I.; Abbott, S.; Klepac, P.; Flasche, S., Early dynamics of transmission and control of COVID-19: a mathematical modelling study. *The Lancet Infectious Diseases* **2020,** *20* (5), 553-558.
69. Pani, S. K.; Lin, N. H.; RavindraBabu, S., Association of COVID-19 pandemic with meteorological parameters over Singapore. *Sci Total Environ* **2020,** *740*, 140112.
70. Lewis, E. R., An examination of Köhler theory resulting in an accurate expression for the equilibrium radius ratio of a hygroscopic aerosol particle valid up to and including relative humidity 100%. *Journal of Geophysical Research* **2008,** *113* (D3).
71. Stokes, G. G., *Mathematical and physical papers*. Johnson reprint corp: 1850; Vol. 3.
72. On the velocity of steady fall of spherical particles through fluid medium. *Proceedings of the Royal Society of London. Series A, Containing Papers of a Mathematical and Physical Character* **1997,** *83* (563), 357-365.
73. Epstein, P. S., On the Resistance Experienced by Spheres in their Motion through Gases. *Physical Review* **1924,** *23* (6), 710-733.
74. Millikan, R. A., The General Law of Fall of a Small Spherical Body through a Gas, and its Bearing upon the Nature of Molecular Reflection from Surfaces. *Physical Review* **1923,** *22* (1), 1-23.
75. Jakobsen, A. B.; Merrison, J.; Iversen, J. J., Laboratory study of aerosol settling velocities using Laser Doppler velocimetry. *Journal of Aerosol Science* **2019,** *135*, 58-71.

76. Lin, K.; Marr, L. C., Humidity-Dependent Decay of Viruses, but Not Bacteria, in Aerosols and Droplets Follows Disinfection Kinetics. *Environ Sci Technol* **2020,** *54* (2), 1024-1032.
77. Prussin, A. J., 2nd; Schwake, D. O.; Lin, K.; Gallagher, D. L.; Buttling, L.; Marr, L. C., Survival of the Enveloped Virus Phi6 in Droplets as a Function of Relative Humidity, Absolute Humidity, and Temperature. *Appl Environ Microbiol* **2018,** *84* (12).
78. Chan, K. H.; Peiris, J. S.; Lam, S. Y.; Poon, L. L.; Yuen, K. Y.; Seto, W. H., The Effects of Temperature and Relative Humidity on the Viability of the SARS Coronavirus. *Adv Virol* **2011,** *2011*, 734690.
79. Shimasaki, N.; Morikawa, H., Prevention of COVID-19 Infection with Personal Protective Equipment. *Journal of Disaster Research* **2021,** *16* (1), 61-69.
80. Yang, W.; Elankumaran, S.; Marr, L. C., Relationship between humidity and influenza A viability in droplets and implications for influenza's seasonality. *PLoS One* **2012,** *7* (10), e46789.
81. Dadar, M.; Fakhri, Y.; Bjorklund, G.; Shahali, Y., The association between the incidence of COVID-19 and the distance from the virus epicenter in Iran. *Arch Virol* **2020,** *165* (11), 2555-2560.
82. Suhaimi, N. F.; Jalaludin, J.; Latif, M. T., Demystifying a Possible Relationship between COVID-19, Air Quality and Meteorological Factors: Evidence from Kuala Lumpur, Malaysia. *Aerosol and Air Quality Research* **2020,** *20* (7), 1520-1529.
83. Venna, S. R.; Tavanaei, A.; Gottumukkala, R. N.; Raghavan, V. V.; Maida, A. S.; Nichols, S., A Novel Data-Driven Model for Real-Time Influenza Forecasting. *IEEE Access* **2019,** *7*, 7691-7701.
84. Tomar, A.; Gupta, N., Prediction for the spread of COVID-19 in India and effectiveness of preventive measures. *Sci Total Environ* **2020,** *728*, 138762.
85. Babin, S., Use of Weather Variables in SARS-CoV-2 Transmission Studies. *Int J Infect Dis* **2020,** *100*, 333-336.
86. Tanaka, K.; Shigemori, K.; Shionoya, M., Cyclic metallopeptides, cyclo[Gly-L-Cys(terpyPt(II))](n)Cl(n). *Chemical Communications* **1999,** (24), 2475-2476.
87. Maruyama, Y.; Hasegawa, K., Evaporation and drying kinetics of water-NaCl droplets via acoustic levitation. *RSC Advances* **2020,** *10* (4), 1870-1877.
88. Gregson, F. K. A.; Robinson, J. F.; Miles, R. E. H.; Royall, C. P.; Reid, J. P., Drying Kinetics of Salt Solution Droplets: Water Evaporation Rates and Crystallization. *J Phys Chem B* **2019,** *123* (1), 266-276.
89. Rezaei, M.; Netz, R. R., Airborne virus transmission via respiratory droplets: Effects of droplet evaporation and sedimentation. *Curr Opin Colloid Interface Sci* **2021,** *55*, 101471.

90. Kallapur, B.; Ramalingam, K.; Bastian; Mujib, A.; Sarkar, A.; Sethuraman, S., Quantitative estimation of sodium, potassium and total protein in saliva of diabetic smokers and nonsmokers: A novel study. *J Nat Sci Biol Med* **2013,** *4* (2), 341-5.
91. Morawska, L.; Johnson, G. R.; Ristovski, Z. D.; Hargreaves, M.; Mengersen, K.; Corbett, S.; Chao, C. Y. H.; Li, Y.; Katoshevski, D., Size distribution and sites of origin of droplets expelled from the human respiratory tract during expiratory activities. *Journal of Aerosol Science* **2009,** *40* (3), 256-269.
92. Millero, F. J., The apparent and partial molal volume of aqueous sodium chloride solutions at various temperatures. *The Journal of Physical Chemistry* **1970,** *74* (2), 356-362.
93. Stull, D. R., Vapor Pressure of Pure Substances. Organic and Inorganic Compounds. *Industrial & Engineering Chemistry* **1947,** *39* (4), 517-540.
94. Vargaftik, N. B.; Volkov, B. N.; Voljak, L. D., International Tables of the Surface Tension of Water. *Journal of Physical and Chemical Reference Data* **1983,** *12* (3), 817-820.
95. Bolz, R. E., *CRC Handbook of Tables for Applied Engineering Science*. CRC press: 1973.
96. Somsen, G. A.; van Rijn, C.; Kooij, S.; Bem, R. A.; Bonn, D., Small droplet aerosols in poorly ventilated spaces and SARS-CoV-2 transmission. *The Lancet Respiratory Medicine* **2020,** *8* (7), 658-659.
97. Zhao, H.; Lu, X.; Deng, Y.; Tang, Y.; Lu, J., COVID-19: asymptomatic carrier transmission is an underestimated problem. *Epidemiol Infect* **2020,** *148*, e116.
98. He, X.; Lau, E. H. Y.; Wu, P.; Deng, X.; Wang, J.; Hao, X.; Lau, Y. C.; Wong, J. Y.; Guan, Y.; Tan, X.; Mo, X.; Chen, Y.; Liao, B.; Chen, W.; Hu, F.; Zhang, Q.; Zhong, M.; Wu, Y.; Zhao, L.; Zhang, F.; Cowling, B. J.; Li, F.; Leung, G. M., Temporal dynamics in viral shedding and transmissibility of COVID-19. *Nat Med* **2020,** *26* (5), 672-675.
99. Allen, M. D.; Raabe, O. G., Re-evaluation of millikan's oil drop data for the motion of small particles in air. *Journal of Aerosol Science* **1982,** *13* (6), 537-547.
100. Netz, R. R.; Eaton, W. A., Physics of virus transmission by speaking droplets. *Proc Natl Acad Sci U S A* **2020,** *117* (41), 25209-25211.
101. Jamshidi, S.; Baniasad, M.; Niyogi, D., Global to USA County Scale Analysis of Weather, Urban Density, Mobility, Homestay, and Mask Use on COVID-19. *Int J Environ Res Public Health* **2020,** *17* (21).
102. Ogaugwu, C.; Mogaji, H.; Ogaugwu, E.; Nebo, U.; Okoh, H.; Agbo, S.; Agbon, A., Effect of Weather on COVID-19 Transmission and Mortality in Lagos, Nigeria. *Scientifica (Cairo)* **2020,** *2020*, 2562641.
103. Malki, Z.; Atlam, E. S.; Hassanien, A. E.; Dagnew, G.; Elhosseini, M. A.; Gad, I., Association between weather data and COVID-19 pandemic predicting

mortality rate: Machine learning approaches. *Chaos Solitons Fractals* **2020,** *138*, 110137.

104. Chanda, A., COVID-19 in India: transmission dynamics, epidemiological characteristics, testing, recovery and effect of weather. *Epidemiol Infect* **2020,** *148*, e182.
105. Hughes, V. C., The Effect of Temperature, Dewpoint, and Population Density on COVID-19 Transmission in the United States: A Comparative Study. *American Journal of Public Health Research* **2020,** *8* (4), 112-117.
106. Joonaki, E.; Hassanpouryouzband, A.; Heldt, C. L.; Areo, O., Surface Chemistry Can Unlock Drivers of Surface Stability of SARS-CoV-2 in a Variety of Environmental Conditions. *Chem* **2020,** *6* (9), 2135-2146.
107. Beckmann, M.; Václavík, T.; Manceur, A. M.; Šprtová, L.; von Wehrden, H.; Welk, E.; Cord, A. F.; Tatem, A., glUV: a global UV-B radiation data set for macroecological studies. *Methods in Ecology and Evolution* **2014,** *5* (4), 372-383.
108. Sajadi, M. M.; Habibzadeh, P.; Vintzileos, A.; Shokouhi, S.; Miralles-Wilhelm, F.; Amoroso, A., Temperature, Humidity and Latitude Analysis to Predict Potential Spread and Seasonality for COVID-19. *SSRN* **2020**, 3550308.
109. Gupta, S.; Raghuwanshi, G. S.; Chanda, A., Effect of weather on COVID-19 spread in the US: A prediction model for India in 2020. *Sci Total Environ* **2020,** *728*, 138860.
110. Zhao, L.; Qi, Y.; Luzzatto-Fegiz, P.; Cui, Y.; Zhu, Y., COVID-19: Effects of Environmental Conditions on the Propagation of Respiratory Droplets. *Nano Lett* **2020,** *20* (10), 7744-7750.
111. Pan, J.; Yao, Y.; Liu, Z.; Meng, X.; Ji, J. S.; Qiu, Y.; Wang, W.; Zhang, L.; Wang, W.; Kan, H., Warmer weather unlikely to reduce the COVID-19 transmission: An ecological study in 202 locations in 8 countries. *Science of The Total Environment* **2021,** *753*.
112. Yao, Y.; Pan, J.; Liu, Z.; Meng, X.; Wang, W.; Kan, H.; Wang, W., No association of COVID-19 transmission with temperature or UV radiation in Chinese cities. *Eur Respir J* **2020,** *55* (5).
113. Smith, S. H.; Somsen, G. A.; van Rijn, C.; Kooij, S.; van der Hoek, L.; Bem, R. A.; Bonn, D., Aerosol persistence in relation to possible transmission of SARS-CoV-2. *Phys Fluids (1994)* **2020,** *32* (10), 107108.
114. Organization, W. H., Coronavirus disease (COVID-19): How is it transmitted? 2021.
115. Evans, M. J., Avoiding COVID-19: Aerosol Guidelines. *medRxiv* **2020**.
116. Pan, J.; Tang, J.; Caniza, M.; Heraud, J.-M.; Koay, E.; Lee, H. K.; Lee, C. K.; Li, Y.; Ruiz, A. N.; Santillan-Salas, C. F.; Marr, L., Correlating Indoor and Outdoor Temperature and Humidity in a Sample of Buildings in Tropical Climates. *engrXiv* **2021**.

117. Nguyen, J. L.; Dockery, D. W., Daily indoor-to-outdoor temperature and humidity relationships: a sample across seasons and diverse climatic regions. *Int J Biometeorol* **2016,** *60* (2), 221-9.
118. Nguyen, J. L.; Schwartz, J.; Dockery, D. W., The relationship between indoor and outdoor temperature, apparent temperature, relative humidity, and absolute humidity. *Indoor Air* **2014,** *24* (1), 103-12.
119. Lee, K.; Lee, D., The Relationship Between Indoor and Outdoor Temperature in Two Types Of Residence. *Energy Procedia* **2015,** *78*, 2851-2856.
120. Habeebullah, T. M.; Abd El-Rahim, I. H. A.; Morsy, E. A., Impact of outdoor and indoor meteorological conditions on the COVID-19 transmission in the western region of Saudi Arabia. *J Environ Manage* **2021,** *288*, 112392.
121. Ahlawat, A.; Wiedensohler, A.; Mishra, S. K., An Overview on the Role of Relative Humidity in Airborne Transmission of SARS-CoV-2 in Indoor Environments. *Aerosol and Air Quality Research* **2020,** *20* (9), 1856-1861.
122. Chong, K. L.; Ng, C. S.; Hori, N.; Yang, R.; Verzicco, R.; Lohse, D., Extended Lifetime of Respiratory Droplets in a Turbulent Vapor Puff and Its Implications on Airborne Disease Transmission. *Phys Rev Lett* **2021,** *126* (3), 034502.
123. Phillips, N., The coronavirus is here to stay — here's what that means. *Nature* Febuary 18, 2021, 2021, p 3.
124. Lavine, J. S.; Bjornstad, O. N.; Antia, R., Immunological characteristics govern the transition of COVID-19 to endemicity. *Science* **2021,** *371* (6530), 741-745.
125. Xiao, F.; Sun, J.; Xu, Y.; Li, F.; Huang, X.; Li, H.; Zhao, J.; Huang, J.; Zhao, J., Infectious SARS-CoV-2 in Feces of Patient with Severe COVID-19. *Emerg Infect Dis* **2020,** *26* (8), 1920-1922.
126. Zhang, N.; Gong, Y.; Meng, F.; Shi, Y.; Wang, J.; Mao, P.; Chuai, X.; Bi, Y.; Yang, P.; Wang, F., Comparative study on virus shedding patterns in nasopharyngeal and fecal specimens of COVID-19 patients. *Sci China Life Sci* **2020**.
127. Wolfel, R.; Corman, V. M.; Guggemos, W.; Seilmaier, M.; Zange, S.; Muller, M. A.; Niemeyer, D.; Jones, T. C.; Vollmar, P.; Rothe, C.; Hoelscher, M.; Bleicker, T.; Brunink, S.; Schneider, J.; Ehmann, R.; Zwirglmaier, K.; Drosten, C.; Wendtner, C., Virological assessment of hospitalized patients with COVID-2019. *Nature* **2020,** *581* (7809), 465-469.
128. Shutler, J. D.; Zaraska, K.; Holding, T.; Machnik, M.; Uppuluri, K.; Ashton, I. G. C.; Migdal, L.; Dahiya, R. S., Rapid Assessment of SARS-CoV-2 Transmission Risk for Fecally Contaminated River Water. *ACS ES T Water* **2021,** *1* (4), 949-957.
129. Rimoldi, S. G.; Stefani, F.; Gigantiello, A.; Polesello, S.; Comandatore, F.; Mileto, D.; Maresca, M.; Longobardi, C.; Mancon, A.; Romeri, F.; Pagani, C.; Cappelli, F.; Roscioli, C.; Moja, L.; Gismondo, M. R.; Salerno, F., Presence

and infectivity of SARS-CoV-2 virus in wastewaters and rivers. *Sci Total Environ* **2020,** *744*, 140911.

130. Haramoto, E.; Malla, B.; Thakali, O.; Kitajima, M., First environmental surveillance for the presence of SARS-CoV-2 RNA in wastewater and river water in Japan. *Sci Total Environ* **2020,** *737*, 140405.
131. Prado, T.; Fumian, T. M.; Mannarino, C. F.; Resende, P. C.; Motta, F. C.; Eppinghaus, A. L. F.; Chagas do Vale, V. H.; Braz, R. M. S.; de Andrade, J.; Maranhao, A. G.; Miagostovich, M. P., Wastewater-based epidemiology as a useful tool to track SARS-CoV-2 and support public health policies at municipal level in Brazil. *Water Res* **2021,** *191*, 116810.
132. Randazzo, W.; Truchado, P.; Cuevas-Ferrando, E.; Simon, P.; Allende, A.; Sanchez, G., SARS-CoV-2 RNA in wastewater anticipated COVID-19 occurrence in a low prevalence area. *Water Res* **2020,** *181*, 115942.
133. de Oliveira, L. C.; Torres-Franco, A. F.; Lopes, B. C.; Santos, B.; Costa, E. A.; Costa, M. S.; Reis, M. T. P.; Melo, M. C.; Polizzi, R. B.; Teixeira, M. M.; Mota, C. R., Viability of SARS-CoV-2 in river water and wastewater at different temperatures and solids content. *Water Res* **2021,** *195*, 117002.
134. Tran, H. N.; Le, G. T.; Nguyen, D. T.; Juang, R. S.; Rinklebe, J.; Bhatnagar, A.; Lima, E. C.; Iqbal, H. M. N.; Sarmah, A. K.; Chao, H. P., SARS-CoV-2 coronavirus in water and wastewater: A critical review about presence and concern. *Environ Res* **2021,** *193*, 110265.
135. Shao, L.; Ge, S.; Jones, T.; Santosh, M.; Silva, L. F. O.; Cao, Y.; Oliveira, M. L. S.; Zhang, M.; BéruBé, K., The role of airborne particles and environmental considerations in the transmission of SARS-CoV-2. *Geoscience Frontiers* **2021,** *12* (5).
136. Carducci, A.; Federigi, I.; Liu, D.; Thompson, J. R.; Verani, M., Making Waves: Coronavirus detection, presence and persistence in the water environment: State of the art and knowledge needs for public health. *Water Res* **2020,** *179*, 115907.
137. Ahmed, W.; Angel, N.; Edson, J.; Bibby, K.; Bivins, A.; O'Brien, J. W.; Choi, P. M.; Kitajima, M.; Simpson, S. L.; Li, J.; Tscharke, B.; Verhagen, R.; Smith, W. J. M.; Zaugg, J.; Dierens, L.; Hugenholtz, P.; Thomas, K. V.; Mueller, J. F., First confirmed detection of SARS-CoV-2 in untreated wastewater in Australia: A proof of concept for the wastewater surveillance of COVID-19 in the community. *Sci Total Environ* **2020,** *728*, 138764.
138. Cervantes-Avilés, P.; Moreno-Andrade, I.; Carrillo-Reyes, J., Approaches applied to detect SARS-CoV-2 in wastewater and perspectives post-COVID-19. *Journal of Water Process Engineering* **2021,** *40*.
139. Pecson, B. M.; Darby, E.; Haas, C. N.; Amha, Y. M.; Bartolo, M.; Danielson, R.; Dearborn, Y.; Di Giovanni, G.; Ferguson, C.; Fevig, S.; Gaddis, E.; Gray, D.; Lukasik, G.; Mull, B.; Olivas, L.; Olivieri, A.; Qu, Y.; Consortium, S. A.-C.-I., Reproducibility and sensitivity of 36 methods to quantify the SARS-

CoV-2 genetic signal in raw wastewater: findings from an interlaboratory methods evaluation in the U.S. *Environmental Science: Water Research & Technology* **2021,** *7* (3), 504-520.

140. Alygizakis, N.; Markou, A. N.; Rousis, N. I.; Galani, A.; Avgeris, M.; Adamopoulos, P. G.; Scorilas, A.; Lianidou, E. S.; Paraskevis, D.; Tsiodras, S.; Tsakris, A.; Dimopoulos, M. A.; Thomaidis, N. S., Analytical methodologies for the detection of SARS-CoV-2 in wastewater: Protocols and future perspectives. *Trends Analyt Chem* **2021,** *134*, 116125.
141. Furuki, T.; Ito, T.; Asakawa, N.; Inoue, Y.; Sakurai, M., Effects of trehalose on the swelling behavior of hydrogel -visualization of the preferential hydration of disaeeharides. *Chemistry Letters* **2009,** *38* (3), 264-265.
142. Kitajima, M.; Ahmed, W.; Bibby, K.; Carducci, A.; Gerba, C. P.; Hamilton, K. A.; Haramoto, E.; Rose, J. B., SARS-CoV-2 in wastewater: State of the knowledge and research needs. *Sci Total Environ* **2020,** *739*, 139076.
143. Chotiwan, N.; Brewster, C. D.; Magalhaes, T.; Weger-Lucarelli, J.; Duggal, N. K.; Ruckert, C.; Nguyen, C.; Garcia Luna, S. M.; Fauver, J. R.; Andre, B.; Gray, M.; Black, W. C. t.; Kading, R. C.; Ebel, G. D.; Kuan, G.; Balmaseda, A.; Jaenisch, T.; Marques, E. T. A.; Brault, A. C.; Harris, E.; Foy, B. D.; Quackenbush, S. L.; Perera, R.; Rovnak, J., Rapid and specific detection of Asian- and African-lineage Zika viruses. *Sci Transl Med* **2017,** *9* (388).
144. Yang, B. Y.; Liu, X. L.; Wei, Y. M.; Wang, J. Q.; He, X. Q.; Jin, Y.; Wang, Z. J., Rapid and sensitive detection of human astrovirus in water samples by loop-mediated isothermal amplification with hydroxynaphthol blue dye. *BMC Microbiol* **2014,** *14*, 38.
145. Huang, X.; Lin, X.; Urmann, K.; Li, L.; Xie, X.; Jiang, S.; Hoffmann, M. R., Smartphone-Based in-Gel Loop-Mediated Isothermal Amplification (gLAMP) System Enables Rapid Coliphage MS2 Quantification in Environmental Waters. *Environ Sci Technol* **2018,** *52* (11), 6399-6407.
146. Li, J.; Zhu, Y.; Wu, X.; Hoffmann, M. R., Rapid Detection Methods for Bacterial Pathogens in Ambient Waters at the Point of Sample Collection: A Brief Review. *Clin Infect Dis* **2020,** *71* (Suppl 2), S84-S90.
147. Fu, J.; Chiang, E. L. C.; Medriano, C. A. D.; Li, L.; Bae, S., Rapid quantification of fecal indicator bacteria in water using the most probable number - loop-mediated isothermal amplification (MPN-LAMP) approach on a polymethyl methacrylate (PMMA) microchip. *Water Research* **2021,** *199*.
148. Ning, B.; Yu, T.; Zhang, S.; Huang, Z.; Tian, D.; Lin, Z.; Niu, A.; Golden, N.; Hensley, K.; Threeton, B.; Lyon, C. J.; Yin, X. M.; Roy, C. J.; Saba, N. S.; Rappaport, J.; Wei, Q.; Hu, T. Y., A smartphone-read ultrasensitive and quantitative saliva test for COVID-19. *Sci Adv* **2021,** *7* (2).
149. Ganguli, A.; Mostafa, A.; Berger, J.; Aydin, M. Y.; Sun, F.; Ramirez, S. A. S.; Valera, E.; Cunningham, B. T.; King, W. P.; Bashir, R., Rapid isothermal

amplification and portable detection system for SARS-CoV-2. *Proc Natl Acad Sci U S A* **2020,** *117* (37), 22727-22735.

150. Prado, T.; Fumian, T. M.; Mannarino, C. F.; Maranhao, A. G.; Siqueira, M. M.; Miagostovich, M. P., Preliminary results of SARS-CoV-2 detection in sewerage system in Niteroi municipality, Rio de Janeiro, Brazil. *Mem Inst Oswaldo Cruz* **2020,** *115*, e200196.
151. Barril, P. A.; Pianciola, L. A.; Mazzeo, M.; Ousset, M. J.; Jaureguiberry, M. V.; Alessandrello, M.; Sanchez, G.; Oteiza, J. M., Evaluation of viral concentration methods for SARS-CoV-2 recovery from wastewaters. *Sci Total Environ* **2021,** *756*, 144105.
152. Xie, X.; Bahnemann, J.; Wang, S.; Yang, Y.; Hoffmann, M. R., "Nanofiltration" Enabled by Super-Absorbent Polymer Beads for Concentrating Microorganisms in Water Samples. *Sci Rep* **2016,** *6*, 20516.
153. Chen, W.; Wang, T.; Dou, Z.; Xie, X., Self-Driven "Microfiltration" Enabled by Porous Superabsorbent Polymer (PSAP) Beads for Biofluid Specimen Processing and Storage. *ACS Mater Lett* **2020,** *2* (11), 1545-1554.
154. Fagnant, C. S.; Sanchez-Gonzalez, L. M.; Zhou, N. A.; Falman, J. C.; Eisenstein, M.; Guelig, D.; Ockerman, B.; Guan, Y.; Kossik, A. L.; Linden, Y. S.; Beck, N. K.; Wilmouth, R.; Komen, E.; Mwangi, B.; Nyangao, J.; Shirai, J. H.; Novosselov, I.; Borus, P.; Boyle, D. S.; Meschke, J. S., Improvement of the Bag-Mediated Filtration System for Sampling Wastewater and Wastewater-Impacted Waters. *Food Environ Virol* **2018,** *10* (1), 72-82.
155. Tetko, I. V.; Livingstone, D. J.; Luik, A. I., Neural network studies. 1. Comparison of overfitting and overtraining. *Journal of Chemical Information and Computer Sciences* **1995,** *35* (5), 826-833.
156. Sjöberg, J.; Ljung, L., Overtraining, Regularization, and Searching for Minimum in Neural Networks. *IFAC Proceedings Volumes* **1992,** *25* (14), 73-78.
157. Flangan, J.; Jones, D. P.; Griffith, W. P.; Skapski, A. C.; West, A. P., On the existence of peroxocarbonates in aqueous solution. *Journal of the Chemical Society, Chemical Communications* **1986,** (1), 20-21.
158. Bakhmutova-Albert, E. V.; Yao, H.; Denevan, D. E.; Richardson, D. E., Kinetics and Mechanism of Peroxymonocarbonate Formation. *Inorganic Chemistry* **2010,** *49* (24), 11287-11296.
159. Richardson, D. E.; Yao, H.; Frank, K. M.; Bennett, D. A., Equilibria, Kinetics, and Mechanism in the Bicarbonate Activation of Hydrogen Peroxide: Oxidation of Sulfides by Peroxymonocarbonate. *Journal of the American Chemical Society* **2000,** *122* (8), 1729-1739.
160. Yao, H.; Richardson, D. E., Epoxidation of Alkenes with Bicarbonate-Activated Hydrogen Peroxide. *Journal of the American Chemical Society* **2000,** *122* (13), 3220-3221.

161. Ho, K.-P.; Chan, T. H.; Wong, K.-Y., An environmentally benign catalytic system for alkene epoxidation with hydrogen peroxide electrogenerated in situ. *Green Chemistry* **2006,** *8* (10), 900-905.
162. Bennett, D. A.; Yao, H.; Richardson, D. E., Mechanism of Sulfide Oxidations by Peroxymonocarbonate. *Inorganic Chemistry* **2001,** *40* (13), 2996-3001.
163. Yang, X.; Duan, Y.; Wang, J.; Wang, H.; Liu, H.; Sedlak, D. L., Impact of Peroxymonocarbonate on the Transformation of Organic Contaminants during Hydrogen Peroxide in Situ Chemical Oxidation. *Environmental Science & Technology Letters* **2019,** *6* (12), 781-786.
164. Vione, D.; Maurino, V.; Minero, C.; Pelizzetti, E., The atmospheric chemistry of hydrogen peroxide: a review. *Ann Chim* **2003,** *93* (4), 477-488.
165. Goosse, H.; Barriat, P.-Y.; Brovkin, V.; Klein, F.; Meissner, K. J.; Menviel, L.; Mouchet, A., Changes in atmospheric CO2 concentration over the past two millennia: contribution of climate variability, land-use and Southern Ocean dynamics. *Climate Dynamics* **2022**.
166. NIST.gov Carbon dioxide. https://webbook.nist.gov/cgi/cbook.cgi?ID=C124389&Mask=10#Solubility.
167. Enami, S.; Mishra, H.; Hoffmann, M. R.; Colussi, A. J., Protonation and Oligomerization of Gaseous Isoprene on Mildly Acidic Surfaces: Implications for Atmospheric Chemistry. *Journal of Physical Chemistry A* **2012,** *116* (24), 6027-6032.
168. Gu, A. Y.; Musgrave, C.; Goddard, W. A.; Hoffmann, M. R.; Colussi, A. J., Role of Ferryl Ion Intermediates in Fast Fenton Chemistry on Aqueous Microdroplets. *Environmental Science & Technology* **2021,** *55* (21), 14370-14377.
169. Zhu, L.; Nicovich, J. M.; Wine, P. H., Temperature-dependent kinetics studies of aqueous phase reactions of hydroxyl radicals with dimethylsulfoxide, dimethylsulfone, and methanesulfonate. *Aquatic Sciences* **2003,** *65* (4), 425-435.
170. Mishra, H.; Enami, S.; Nielsen, R. J.; Stewart, L. A.; Hoffmann, M. R.; Goddard, W. A.; Colussi, A. J., Bronsted basicity of the air-water interface. *Proceedings of the National Academy of Sciences of the United States of America* **2012,** *109* (46), 18679-18683.

Appendix A: Coordinates of DFT-optimized Structures

no ligand

O14	0.7680228217	-1.3052848462	-2.2919432579
H2	0.7584223414	-2.2501763863	-2.0661375355
Fe4	-0.7497366749	-0.0067991904	-2.0394507429
O5	-1.0603443397	0.3322663998	-4.0031504829
H19	-0.4036576990	0.0111010687	-4.6772658472
H20	-1.9243029173	0.7630532931	-4.2591255829
O9	-2.3928455969	0.6745027680	-1.3910942292
H23	-2.7752923342	0.7883218354	-0.5090241509
O10	-3.3577077614	1.4137914804	-3.6805626934
H11	-4.2761494874	1.2317566774	-3.9309555931
H12	-3.1649396027	1.2110512342	-2.6989924854
O25	0.8722547616	0.7285103625	-0.8588231959
H29	1.4614618184	-0.0136329128	-1.1579825200
H30	1.3011820145	1.5741223300	-0.6654673386
O15	1.0136826305	-0.8901396470	-4.8566046002
H16	1.8627748015	-0.8113791205	-5.3154377222

H17	1.0934667770	-1.1445303650	-3.8734238435

dma-Fe(II)

O14	0.7680228217	-1.3052848462	-2.2919432579
H2	0.7584223414	-2.2501763863	-2.0661375355
Fe4	-0.7497366749	-0.0067991904	-2.0394507429
O5	-1.0603443397	0.3322663998	-4.0031504829
H19	-0.4036576990	0.0111010687	-4.6772658472
H20	-1.9243029173	0.7630532931	-4.2591255829
O9	-2.3928455969	0.6745027680	-1.3910942292
H23	-2.7752923342	0.7883218354	-0.5090241509
O10	-3.3577077614	1.4137914804	-3.6805626934
H11	-4.2761494874	1.2317566774	-3.9309555931
H12	-3.1649396027	1.2110512342	-2.6989924854
O25	0.8722547616	0.7285103625	-0.8588231959
H29	1.4614618184	-0.0136329128	-1.1579825200
H30	1.3011820145	1.5741223300	-0.6654673386
O15	1.0136826305	-0.8901396470	-4.8566046002
H16	1.8627748015	-0.8113791205	-5.3154377222

H17	1.0934667770	-1.1445303650	-3.8734238435

tma-Fe(II)

O14	-0.1655340093	-1.7268063039	-2.6095353944
H2	-0.3944219122	-2.4108828075	-3.2632278177
Fe4	-0.7707577602	0.2290541593	-2.7723227762
O5	1.5230329615	0.0171089392	-3.2915139341
H19	2.2534865858	0.4255137552	-2.7999395253
H20	1.2970082143	-0.9133447146	-2.9833107091
O9	-1.0066552088	1.9487382218	-2.0424117983
H23	-0.4984929168	2.6898021231	-1.6832136443
O10	-2.7446668203	-0.2142757076	-1.8892807656
H11	-2.6311698838	-0.9745628100	-1.2442971945
H12	-2.9093194947	0.6370485030	-1.4418975663
C15	-0.3704657242	1.5432800780	-5.3973751225
N16	-1.3494873767	0.5781975649	-4.8293540290
C17	-1.3520134653	-0.6929262087	-5.5942865208
C18	-2.7126537661	1.1736537290	-4.7711098241
H17	-0.3698260792	2.4343964075	-4.7735754166

H18	0.6210145965	1.0993010209	-5.3613931753
H21	-0.6314231817	1.8119699517	-6.4290141523
H22	-3.3882196531	0.4632592938	-4.3008771379
H24	-2.6684113541	2.0624700457	-4.1458264821
H25	-3.0734805126	1.4336554283	-5.7743633641
H26	-2.0433699061	-1.3905771743	-5.1239071940
H27	-1.6590481908	-0.5333790764	-6.6357488419
H28	-0.3506032286	-1.1197469178	-5.5796786368
O25	-1.7216096955	-2.2138716360	-0.6271053384
H29	-0.9584423562	-2.1602443259	-1.3060684009
H30	-1.5271258971	-2.7088429317	0.1810021166

chloride-Fe(II)

O14	0.3976702798	-1.4773996919	-2.7887423748
H2	0.3772259047	-2.3828298976	-2.4402323102
Fe4	-0.7744413237	0.0396878672	-2.3567048422
O5	-0.4405337329	0.9590007201	-4.1347828722
H19	0.2048408237	0.4563172448	-4.7563223266
H20	-0.7042765410	1.8602575824	-4.3663319178

Cl7	-2.0465718251	2.1906876266	-1.5487949815
O10	-2.7698035681	-0.5746316041	-2.2415785220
H11	-3.2845621037	-1.3024474873	-2.6210595601
H12	-3.2955943711	0.1981029804	-1.9355223327
O25	0.0677119898	0.4013039493	-0.4685131437
H29	0.9083819222	0.1111906487	-0.0839362415
H30	-0.3260204012	1.2087914841	-0.0767820033
O15	1.1076792753	-0.7458040964	-5.0658618888
H15	2.0233219486	-0.7675916562	-5.3795276228
H16	0.9471859164	-1.2229291780	-4.1439162864

oxolate-Fe(II)

C1	-1.3518626782	1.1887077594	-4.9834823855
C2	-2.5532196878	1.7486002828	-4.1258181644
O3	-0.5120180158	0.4353111114	-4.2416854379
O4	-2.4781394429	1.3550388065	-2.8363637288
O5	-3.4346454728	2.4545424885	-4.6020014847
O6	-1.2233866228	1.4270608016	-6.1786955916
Fe12	-0.9645174245	0.2308612041	-2.3625262650

O13	0.7756771704	-0.8846087072	-2.4678183860
H14	1.4092866072	-1.4248819202	-1.9739703789
H15	0.9923498594	-0.7718231176	-3.4209800224
O19	-1.9321294166	0.3648460913	-0.5381685054
H20	-1.9192305335	0.1031588534	0.3936904919
H21	-2.6949722511	0.9318662328	-0.7925921136

malonate-Fe(II)

C1	-1.4616918542	1.1304608514	-5.1661571065
C2	-1.2714329443	2.5023583365	-4.5030376946
O3	-1.0968863375	0.0667678130	-4.4235751927
C4	-1.8047285398	2.6919085695	-3.0755316379
H5	-0.1931553953	2.6889511511	-4.4657409888
O6	-1.8804805410	1.0237516653	-6.3236382582
O14	-0.8041295636	-2.0812953667	-3.1379597763
H2	-0.7242041158	-3.0082010414	-2.8728350970
H3	-0.8822713734	-1.9276317995	-4.1088390855
Fe4	-1.0391265617	-0.1163462224	-2.5090022568
O9	-1.2111909422	-0.0657317395	-0.4407086955

H23	-1.1927156691	-0.5752420184	0.3813569757
H11	-1.4663830043	0.8814262787	-0.3420113948
H21	-1.7252450582	3.2534853623	-5.1385035080
O21	-2.4638230784	3.6874660982	-2.7578290328
O23	-1.4646765589	1.7322976415	-2.1928647874

tartrate-Fe(II)

O14	-1.6514421105	-1.8037446986	-3.2016132395
H2	-0.8782166179	-2.3375215406	-3.4554012886
H3	-2.0250784525	-1.2961771971	-3.9689215532
Fe4	-1.1622555927	-0.0680175937	-2.0574845815
O5	-0.4773773402	0.2721723939	-0.0245337343
H19	-0.0197998813	1.1195827942	-0.2373498981
H20	-0.9121196573	0.2754788917	0.8419678617
O9	-3.2069017891	0.3054045129	-1.6946044387
H23	-3.9243495893	0.0649971299	-1.0919904700
H11	-3.4851586737	0.5599383102	-2.6048014572
C1	0.4730157885	1.9902243702	-3.1855779800
C3	-0.0656901050	3.0697801899	-4.1047778962

O4	-0.1840267605	1.7659215797	-2.0719341901
O16	1.4376358294	1.2651186962	-3.5768053027
O6	0.2189023788	4.3719950158	-3.5274286290
H17	0.4206992235	2.9654748343	-5.0755107362
C8	-1.5954990426	2.9227511365	-4.2872196458
C9	-2.0158122284	1.5528200241	-4.8450934683
H21	-2.0597191075	3.0866891425	-3.3184752945
O11	-2.0231421899	3.9878224778	-5.1797119088
O12	-2.1214182042	0.5728996453	-3.9639221601
O13	-2.2477233008	1.4471339514	-6.0673969992
H24	-0.2777162296	5.0334969220	-4.0550501423
H25	-2.1656682464	3.5877255092	-6.0674881565
O25	0.8189499681	-0.9216095344	-2.3833207100
H26	1.2971945788	-0.1608816531	-2.8787536239
H27	1.3287089378	-1.2212996424	-1.6126850432

catechol-Fe(II)

Fe12	-0.5956779278	-0.9401152716	0.2442911944
O19	-0.0641533657	-2.5860914580	-0.8414605665

H20	-0.4857873881	-3.4434153186	-0.9876671207
H21	0.7894117351	-2.3994176083	-1.4220580814
O3	0.9037483723	0.0994699490	-0.5350751272
O4	-1.1626559414	0.8549187687	0.8805537158
O2	-1.9006279704	-1.8627505236	1.5280222944
O9	1.9342327009	-1.6494963794	-1.9434301703
H14	-1.8529718429	-2.7250732998	1.9639493732
H15	-2.4626456572	-1.1440970974	2.0491894695
H16	1.7221785166	-0.7547518909	-1.4606774503
H17	2.2648531891	-1.5603602027	-2.8480258542
C18	1.7853262644	2.3837395314	-0.6464735707
C19	1.6252613215	3.7306074347	-0.2932518041
C20	0.5245932933	4.1333091482	0.4623212547
C21	-0.4308054519	3.1944058586	0.8748758531
C22	-0.2771226398	1.8582754859	0.5273418125
C23	0.8405206769	1.4491445309	-0.2410467840
H24	2.6380529391	2.0553087099	-1.2254254775
H25	2.3624061718	4.4568960240	-0.6084718613

H26	0.4040237131	5.1732759769	0.7345625678
H27	-1.2892951836	3.4918655486	1.4619238817
O24	-2.8870026391	0.1722230671	2.5095915311
H28	-2.2287624942	0.7235761957	1.9222535597
H29	-3.7774477684	0.5429349855	2.5857212916

benzoquinone-Fe(II)

O14	-2.1186606245	-2.0330178699	-3.4766712638
H2	-1.7110437184	-2.8065899684	-3.8902478609
Fe4	-1.5826270926	-0.2725983695	-2.9442561269
O5	0.4667181523	-0.6707772548	-2.4140302042
H19	0.7853925743	-0.0436280888	-1.6736822804
H20	0.7894363751	-1.5789341100	-2.3176158604
O9	-1.7095024198	1.0633733797	-1.5067325193
H23	-2.5292589483	1.2951705630	-1.0419301855
C12	-0.9835245578	4.4261319780	-4.2637500302
C13	-0.7667867987	4.7969576318	-5.6762862064
C14	-0.7056628207	3.7041517454	-6.6690358545
C15	-0.8387391407	2.4191842623	-6.2960011504

C16	-1.0456754895	2.0722092741	-4.8896318749
C17	-1.1152442243	3.1409290226	-3.8902286842
H18	-1.0313787026	5.2453880592	-3.5602276380
O19	-0.6406081947	5.9946269726	-6.0237298167
H21	-0.5506789537	4.0018632805	-7.6963036701
H22	-0.8011329848	1.5959988243	-6.9950094579
O22	-1.1620190215	0.8568588095	-4.5495591471
H24	-1.2848007384	2.8159522541	-2.8701704676
O24	0.6212912162	1.0513770642	-0.5890245469
H25	1.1273764089	1.8511384761	-0.3856808558
H26	-0.3850810218	1.2049625036	-0.7995724634
O25	-3.8686768794	-0.3105215563	-3.3809351666
H27	-3.6100572652	-1.2646582916	-3.5814909317
H28	-4.6231026128	-0.2362409792	-2.7756407246

1,4-naphthaquinone-Fe(II)

O14	-2.3330166693	-1.8529845874	-3.1567442412
H2	-2.1134553449	-2.2013546529	-4.0393784674
Fe4	-2.0369847501	0.1127559584	-2.7346519190

O5	-0.0259184080	-0.2820138265	-2.0054277126
H19	0.1336151055	0.3770723073	-1.3079220350
H20	0.0344234685	-1.2316951577	-1.6763840411
O9	-2.0594151145	1.6108230847	-1.5786382208
H23	-2.6538379048	1.9814170321	-0.9092494033
C12	-0.6673207976	4.4013859133	-4.4760857333
C13	-0.3348266812	4.6574404834	-5.8887552650
C14	-0.4403463468	3.5185485271	-6.8381550628
C15	-0.8513348222	2.2488021337	-6.3809740599
C16	-1.1765864991	2.0606680104	-4.9594305499
C17	-1.0613474043	3.1926932120	-4.0373574282
H18	-0.5728363762	5.2499105422	-3.8127930005
O19	0.0238390437	5.7978235123	-6.2625896270
O22	-1.5530482676	0.9283364746	-4.5281508752
H24	-1.3173729859	2.9720614262	-3.0025330623
O24	-0.6292734788	-2.6999963722	-1.4539537679
H25	-0.4185315064	-3.6185476096	-1.2356206943
H26	-1.4075003449	-2.5671155202	-2.1116253960

O25	-4.2599455684	-0.2228817903	-3.0519551784
H27	-4.0322538327	-1.1904662335	-3.1058509645
H28	-5.0274303788	-0.0117667436	-2.4984258317
C25	-0.1327384985	3.7016268505	-8.1878418825
C26	-0.2306508689	2.6345405221	-9.0778808383
C27	-0.6379922269	1.3753073624	-8.6246998064
C28	-0.9479634240	1.1824469747	-7.2819352209
H17	0.1799122487	4.6816649576	-8.5180291674
H21	0.0091713829	2.7807248456	-10.1218902618
H22	-0.7126979777	0.5497558889	-9.3186721519
H32	-1.2653547612	0.2183032713	-6.9129865198

Edta-Fe(II)

Fe1	-0.0201860345	-0.0527985469	-1.5477579672
C2	0.2309594348	-0.5387212941	1.3284412618
H3	1.3159592907	-0.4577066522	1.3206807399
H4	-0.0443434899	-0.9914672865	2.2802826269
C5	-0.3938993231	0.8493336457	1.2016493685
H6	-1.4768699862	0.7673251401	1.1280123340

H7	-0.1686644532	1.4402745669	2.0897425281
N8	0.0656556284	1.5531936413	-0.0457658184
N9	-0.1465031056	-1.4332481033	0.1815394047
C10	-0.9429043415	2.5550688064	-0.5162176409
H11	-0.4554144080	3.2367788674	-1.2128100505
H12	-1.3490559029	3.1464925086	0.3044915698
C13	-1.5210055282	-1.9736284817	0.2507162620
H14	-2.2347133009	-1.1525255293	0.2993244005
H15	-1.7405366469	-2.4810626367	-0.6890074449
C16	0.9102514866	-2.4570427149	-0.0983692907
H17	1.2861334043	-2.9106441524	0.8142741908
H18	0.4726075719	-3.2463783370	-0.7102906298
C19	1.4523813934	2.1037980291	0.0260191245
H20	2.1315944497	1.3111421669	0.3268475968
H21	1.7424284506	2.4260575356	-0.9683609208
C22	2.0740081352	-1.8402677262	-0.8998822036
O23	3.2157526157	-2.2986553661	-0.8094911302
O24	1.7188718275	-0.8098844195	-1.6745545121

C25	-1.8664813215	-2.9477064727	1.3671694415
O26	-2.9823940627	-3.4263989896	1.5258391652
O27	-0.8044216259	-3.2552904155	2.1845071381
C28	1.5660572782	3.2549419054	1.0034869647
O29	1.4894827336	3.1540821300	2.2273547232
O30	1.7158020658	4.4588388207	0.3676049058
C31	-2.0961154836	1.8544773266	-1.2661276086
O32	-3.2182232445	2.3628134285	-1.3113295574
O33	-1.7463647949	0.6997011022	-1.8401363165
H34	-1.0618301831	-3.9012358449	2.8762685144
H41	1.7789520038	5.2025571125	1.0052252337

No Ligand-Fe(IV)

O14	-0.7676618425	-1.4982343393	-1.9747904571
H2	-1.4603922618	-2.0492513920	-2.3760190591
Fe4	-0.3771310312	0.2612086252	-2.4491642716
O5	-1.2255465979	-0.1137385897	-4.3173038879
H19	-0.9868767899	0.5176026774	-5.0152567168
H20	-2.2282784421	-0.2120524595	-4.1805713315

O9	-1.8757872386	1.1643433113	-1.7776676259
H23	-1.8222603195	2.1370839914	-1.7423046114
O10	-3.5410971322	-0.0349025390	-3.3144509048
H11	-4.3733520407	-0.4848852251	-3.1147829408
H12	-3.1219901715	0.4726787970	-2.5407150427
O25	1.0390217891	-0.2117036898	-1.0544518193
H29	0.8426441574	-1.1446232389	-0.8225357848
H30	1.9464288431	0.1041972450	-0.9403174720
O15	0.4919303872	1.5436287290	-3.0207902164

dma-Fe(IV)

O14	0.2674558505	-1.3794106640	-2.7588283622
H2	0.1159597623	-2.3082724367	-3.0138471775
Fe4	-1.2238841767	-0.1876842959	-2.4887738774
O5	1.4084075656	0.2019226039	-4.5505656020
H19	2.1370135086	0.7888971378	-4.2909003747
H20	1.2014664353	-0.4672458846	-3.8292282519
O9	-0.5383389718	1.4469013938	-2.0067116754
H23	-0.1823221579	1.6285030809	-1.1181767825

O15	-2.5597056719	-1.1505109371	-2.6038165346
O10	-0.9454140708	-0.7710294939	-0.3933960884
H11	-0.1440056731	-1.3249520780	-0.4926067915
H12	-1.7005156098	-1.2835516030	-0.0522736931
H13	-0.3820607680	0.8055453403	-4.5552807397
N16	-1.3718107850	0.5474139685	-4.4011932344
C17	-1.7473922921	-0.4967530355	-5.3897000424
C18	-2.2584289754	1.7393835961	-4.4411789683
H22	-3.2757345509	1.4299441311	-4.2068758849
H24	-1.9116677037	2.4471868986	-3.6941853312
H25	-2.2412562320	2.1978102885	-5.4333070991
H26	-2.7099995782	-0.9171316614	-5.1114728369
H27	-1.7920088278	-0.0719732354	-6.3955460585
H28	-0.9956903584	-1.2807216957	-5.3663394575

tma-Fe(IV)

O14	-0.1219741393	-1.7468986180	-3.2158580786
H2	-0.6096047449	-2.5871383628	-3.2253702642
Fe4	-0.9465209825	-0.1360221249	-2.7506010041

O5	1.1497702089	0.2124356110	-2.8163068011
H19	1.7273383080	0.6408188564	-2.1666872224
H20	1.3492389342	-0.7462703168	-2.9848872383
O9	-1.1592430766	1.4118689302	-1.7373747976
H23	-0.4261571934	1.9885561648	-1.4589095599
O15	-2.4539037517	-0.7254592138	-2.5025316566
O10	-3.8504478122	1.6793595182	-1.5420423367
H11	-4.0805065378	0.7329526296	-1.5881716589
H12	-2.8587845445	1.7255377424	-1.4955221646
C15	-0.1649511077	1.1252158610	-5.3840875548
N16	-1.4081500295	0.6494839274	-4.7180376158
C17	-2.0252329269	-0.4604072149	-5.5002952494
C18	-2.3812211988	1.7714299073	-4.5475343910
H17	0.2955054142	1.8971750752	-4.7744694571
H18	0.5333063299	0.2976498904	-5.4746687769
H21	-0.3922057191	1.5274899372	-6.3768099341
H22	-3.2336070476	1.4330645256	-3.9669507927
H24	-1.9073726560	2.5677048271	-3.9827798142

H25	-2.7028040285	2.1409068078	-5.5267923690
H26	-2.9145295579	-0.8000535808	-4.9786163153
H27	-2.2874137605	-0.1176659393	-6.5065740724
H28	-1.3182667238	-1.2837044734	-5.5605251724

chloride-Fe(IV)

O14	-0.2567421246	-1.6753994051	-2.4544211939
H2	0.4234916029	-2.1870563155	-2.9360707400
Fe4	-0.2585410231	0.1073587212	-2.6339383757
O5	-1.4025090666	1.1067093371	-3.9558461383
H19	-1.0039047482	1.3825874610	-4.7942221047
H20	-2.3926097465	1.3177897201	-3.8353063178
Cl7	-2.0370420418	0.4222682937	-1.0038266588
O10	-3.7930373220	1.5064164494	-3.2401795179
H11	-4.6547677102	1.1984154573	-3.5607950357
H12	-3.6045148703	1.2226194088	-2.3106170341
O25	0.6728210513	1.3911790114	-1.3136725820
H29	1.5774761917	1.7226679869	-1.4245130099
H30	0.2156806574	1.6496971350	-0.4938924121

O15	1.0383441099	0.2068707632	-3.6384647994

oxolate-Fe(IV)

C1	-0.8326044840	3.8464913545	-3.3168126623
C2	-1.5379645714	2.6302145144	-3.9087700508
O3	-1.6246800787	0.1953742130	-0.8615535043
O4	-2.3150763713	1.9695621752	-3.0876873066
O5	-1.2526116725	2.2325784777	-5.0773239562
O6	-1.1058372143	5.0040765779	-3.6018045093
O9	-1.0515866981	-1.9584668322	-2.3840111876
H10	-0.7824834896	-2.2788578886	-1.5055808062
H11	-0.5711698928	-2.3914120598	-3.1098370371
Fe12	-1.4848238163	0.1196158623	-2.4832132691
O13	0.2470919775	0.8173180211	-2.5862786070
H14	0.2594886869	2.5080330233	-2.3143586270
H15	0.7384598900	0.5992527177	-3.4044875255
O16	-1.4117585753	-0.2479259443	-4.5262738027
H17	-2.1532253612	-0.7773840329	-4.8686730954
H18	-1.3589046776	0.6716775381	-4.9974329570

O17	0.1370350613	3.5046483069	-2.4302358273
O18	-3.5400948776	-0.2696288763	-2.7589390177
H19	-4.0433764569	-0.6580468114	-2.0228138324
H20	-3.8384014829	0.6426104946	-2.9789504957

malonate-Fe(IV)

C1	-1.0169153310	1.3080309354	-5.1643155328
C2	-1.3739699689	2.6769038444	-4.5472824056
O3	-1.1950598136	0.2366433093	-4.3711230525
C4	-2.0669554798	2.4361975529	-3.2358384413
H5	-0.4479801240	3.2330343770	-4.4064913840
O6	-0.5884048921	1.2179720765	-6.3186246903
O14	-1.3552295741	-1.9125338633	-3.1069856091
H2	-1.8545909338	-2.5931746663	-2.6296919226
H3	-1.5797833179	-1.8302019128	-4.0564140206
Fe4	-1.0948863774	0.0161832144	-2.4310777849
O5	0.9447216702	-0.1061917349	-2.8237499204
H19	1.6158969561	-0.2443484949	-2.1378884597
H20	1.2763759724	-0.1279179505	-3.7362423652

O9	-3.2696705630	-0.0069822216	-2.1251063657
H23	-3.4485606306	-0.1430629959	-1.1775795201
H11	-3.6324066402	0.8741827051	-2.4178876229
O15	-0.8661509385	-0.3880427825	-0.8551450215
H21	-2.0140813211	3.2147358942	-5.2398838509
O21	-3.3076421273	2.5377957425	-3.0990319894
O23	-1.2846358028	1.9169988091	-2.2742739389

tartrate-Fe(IV)

O14	-1.8801956895	-1.7716265730	-2.8299685378
H2	-1.6315618328	-2.6364459058	-2.4678596123
H3	-1.8315928359	-1.7052421369	-3.8068413722
Fe4	-1.1220764282	0.0374152509	-2.1625962285
O5	0.7973379774	-0.7906793194	-2.6177268308
H19	1.3377312942	-0.0396253888	-3.0248419096
H20	1.2431597112	-1.1520996266	-1.8319777290
O9	-3.0737704682	0.7169229333	-1.8290321371
H23	-3.4017891893	0.7931860220	-0.9182440068
H11	-3.7719962682	0.7000856463	-2.5028347961

O15	-0.9959497283	-0.4214955489	-0.5944910721
C1	0.4705178640	2.1322604441	-3.1307995517
C3	-0.1703559743	3.1981177818	-3.9976274555
O4	-0.2382817293	1.7433499405	-2.0783573587
O16	1.5201339039	1.5510432504	-3.5017462528
O6	-0.1492938366	4.4762590210	-3.3194029374
H17	0.3773252730	3.2456446349	-4.9393791956
C8	-1.6385096893	2.7863906783	-4.2706634896
C9	-1.7650436030	1.3776720906	-4.8684928553
H21	-2.1606536056	2.8257563865	-3.3172677229
O11	-2.2210632654	3.7749793297	-5.1519207094
O12	-1.5140426455	0.3534024263	-4.0607964966
O13	-2.1067380684	1.2436720694	-6.0555170603
H24	-0.6681356974	5.1103850272	-3.8583643017
H25	-2.3413207967	3.3707520791	-6.0402548917

catechol-Fe(IV)

Fe12	-0.8043398489	-0.7618731585	0.1663471937
O19	0.0945217808	-2.5595601633	-0.1652404955

H20	1.0451791380	-2.4446699329	-0.3454811913
H21	-0.3397245506	-3.2500927179	-0.6890240956
O14	-2.3542943879	-1.3319345919	0.0538900022
O3	1.0412266998	-0.1896954464	0.2247675633
O4	-1.2219017022	1.0715491300	0.3032417816
O2	-0.6671904426	-1.1013158427	2.2635509843
O9	-0.6909098452	-0.5498117682	-2.0460772650
H14	0.0638823690	-0.6694127106	2.7361109979
H15	-1.4989368126	-1.1237311354	2.7650912929
H16	-0.0561709325	0.1412880660	-2.3084304602
H17	-1.5924174104	-0.3469216281	-2.3567102223
C18	2.3398816848	1.8924428083	0.3375312608
C19	2.3003314316	3.2896680716	0.4187708728
C20	1.0773503832	3.9661067881	0.4637561504
C21	-0.1278488538	3.2560991196	0.4275607196
C22	-0.0919328082	1.8678954588	0.3472582401
C23	1.1437141201	1.1831560071	0.3024621724
H24	3.2763445030	1.3537643474	0.3035402664

H25	3.2262473013	3.8476346739	0.4471280626
H26	1.0593191539	5.0452967100	0.5269896708
H27	-1.0848267656	3.7566102302	0.4622408556

benzoquinone-Fe(IV)

O14	-1.8416465905	-1.2460000322	-3.2146303901
H2	-1.9810727362	-2.0560253637	-2.6887940822
Fe4	-0.9229699265	0.1729729273	-2.3219502282
O5	0.9613788407	-0.7842530493	-2.8997914785
H19	1.3258565201	-1.3966132912	-2.2383433909
H20	0.8188109617	-1.2110197606	-3.7640459624
O9	-0.3660295322	1.8366937941	-1.7924975025
H23	-0.1464179029	1.9442715948	-0.8483748523
O15	-0.9578065529	-0.5086826880	-0.8242292217
C12	-1.8557968838	4.2035373878	-4.8983578826
C13	-1.7758582767	4.2651361516	-6.3701837301
C14	-1.2583132412	3.0730409030	-7.0841417507
C15	-0.8867841582	1.9755942623	-6.4108838101
C16	-0.9994344702	1.9222100466	-4.9426879916

C17	-1.4949388524	3.1035955349	-4.2190984117
H18	-2.2161213662	5.0945969042	-4.4057486248
O19	-2.1256395932	5.2847373652	-7.0034353276
H21	-1.2054740936	3.1479248719	-8.1606300652
H22	-0.5109850485	1.0851947104	-6.8931909917
O22	-0.6661102150	0.8622802563	-4.3498032786
H24	-1.5057872557	3.0148387771	-3.1443610814
O24	-3.0820280317	0.9174271800	-2.8399918594
H25	-3.1585001576	-0.0195911765	-3.1749001183
H26	-3.7120461012	1.1219291170	-2.1297580792

1,4-naphthaquinone-Fe(IV)

O14	-1.6517175365	-1.3371660716	-3.2755191901
H2	-1.8598839606	-2.1025035525	-2.7051419368
Fe4	-0.9259663879	0.1781495427	-2.3361606991
O5	1.0049186327	-0.7798943905	-2.7955378076
H19	1.5138317566	-1.1475090487	-2.0534811069
H20	0.7215970585	-1.4655070393	-3.4316000790
O9	-0.4091663901	1.8443729204	-1.7683932977

H23	-0.3065956686	1.9551863096	-0.8044918061
O15	-1.1063799845	-0.4704895011	-0.8330219104
C12	-1.7561574411	4.2342106581	-4.9116753170
C13	-1.1953394137	3.1132756264	-8.5161699940
C14	-0.7897853233	1.9721995463	-9.2059928681
C15	-0.4487153311	0.8111273285	-8.5070879218
C16	-0.5084407571	0.7900109833	-7.1162844406
C17	-1.4252628860	3.1231272014	-4.2358846965
H18	-2.0758657459	5.1361103532	-4.4094766631
H17	-1.4675930302	4.0180463851	-9.0394092276
H21	-0.7425710890	1.9852406748	-10.2855435608
H22	-0.1407756992	-0.0730414349	-9.0465060458
O22	-0.6564111708	0.8721688031	-4.3185007719
H24	-1.4233839563	3.0446791991	-3.1589525881
O24	-3.0747216454	0.7796704919	-2.9512099589
H25	-3.0937048431	-0.1353383671	-3.3393985239
H26	-3.7485853563	0.9116276608	-2.2640455682
C25	-1.7019481536	4.3121292033	-6.3835626149

C26	-1.2581773985	3.1012789525	-7.1229018384
C27	-0.9077245369	1.9331094879	-6.4184464229
C28	-0.9784763185	1.9165609592	-4.9448195833
O19	-2.0206600320	5.3661449714	-6.9765392283
H30	-0.2580952964	-0.0979142411	-6.5552741201

edta-Fe(IV)

Fe1	-0.1603003512	-0.1022444073	-1.3974872379
C2	0.4466970058	-0.4559928965	1.4506417070
H3	1.4800091851	-0.1825581253	1.2558330994
H4	0.4025673588	-0.9295879976	2.4303778493
C5	-0.4283897782	0.7940037394	1.4346118295
H6	-1.4803835430	0.5305103584	1.4991049860
H7	-0.1974096335	1.4138130166	2.2942967777
N8	-0.2573856866	1.5671524965	0.1502770960
N9	0.0365044162	-1.4045586258	0.3725860405
C10	-1.4434040114	2.3827221038	-0.2387364167
H11	-2.2943007975	1.7050620670	-0.3094218074
H12	-1.2766535251	2.7523600504	-1.2449683142

C13	-1.2681303540	-2.0761317153	0.5873053527
H14	-2.0580306549	-1.3342159357	0.6494466263
H15	-1.5071850389	-2.6389700215	-0.3143490334
C16	1.0851496829	-2.3673177686	-0.0764890173
H17	2.0530581426	-1.8831258971	0.0191076008
H18	1.0937263964	-3.2745326999	0.5202130397
C19	1.0204509900	2.3519064989	0.0619310401
H20	1.8367166106	1.6415963744	-0.0325268122
H21	0.9909936577	2.9126895659	-0.8644892977
C22	0.8791892170	-2.7168118181	-1.5613762928
O23	1.3863765871	-3.7367931511	-2.0451615212
O24	0.1505319306	-1.8323229770	-2.2415436738
C25	-1.4156316478	-3.0070005110	1.7749270916
O26	-2.4759777929	-3.5369092388	2.0884745070
O27	-0.2572762715	-3.2162165207	2.4890097403
C28	1.2905829470	3.2790720496	1.2223116671
O29	1.6739108447	2.9352514084	2.3387956134
O30	1.0906318743	4.5983214088	0.8892396302

C31	-1.8414745162	3.5633776268	0.6192772333
O32	-2.4135527693	4.5605897196	0.1957896035
O33	-1.5588226995	3.3916397658	1.9554541418
H34	-0.4085316466	-3.8442180320	3.2269303750
O35	-0.1573087997	1.2691854094	-3.0059876856
H36	-0.8532358650	1.2267850911	-3.6840370991
H37	0.7475586686	1.3649587759	-3.3560842194
O38	-1.8196253529	-0.1454599430	-1.4163787988
H41	1.3057011566	5.1921796455	1.6400648647
H40	-1.8655126093	4.1581211449	2.4840582014
O41	1.7105668011	0.2230088512	-1.4632438641
H42	2.2790909087	-0.4051840608	-1.9457193572